https://doi.org/10.15388/vu.thesis.1014
https://orcid.org/0009-0004-4028-5263

VILNIUS UNIVERSITY
CENTER FOR PHYSICAL SCIENCES AND TECHNOLOGY

Darija Astrauskytė

Formation of Thin Dielectric Layers on Structured Elements using Atomic Layer Deposition

DOCTORAL DISSERTATION

Technological Sciences,
Materials Engineering (T 008)

VILNIUS 2026

The dissertation was prepared between 2022 and 2026 at Optical coatings laboratory of the Center for Physical Sciences and Technology.

Academic Supervisor –
Dr. Lina Grinevičiūtė (Center for Physical Sciences and Technology, Technological Sciences, Materials Engineering, T 008).

This doctoral dissertation will be defended in a public meeting of the Dissertation Defence Panel:

Chairman – Dr. Gediminas Račiukaitis (Center for Physical Sciences and Technology, Technological Sciences, Materials Engineering, T 008).
Members:
Dr. Paulius Gečys (Center for Physical Sciences and Technology, Technological Sciences, Materials Engineering, T 008),
Dr. Marco Jupé (Laser Zentrum Hannover e.V., Germany, Natural Sciences, Physics, N 002),
Dr. Arūnas Kadys (Vilnius University, Technological Sciences, Materials Engineering, T 008),
Prof. Dr. Giedrius Laukaitis (Kaunas University of Technology, Natural Sciences, Physics, N 002).

The dissertation shall be defended at a public meeting of the Dissertation Defence Panel at 10:00 on 1st December 2026 in meeting room A140 of the Physics Institute (Center for Physical Sciences and Technology).

Address: Savanorių Ave. 231, 02300 Vilnius, Lithuania
Tel. +37064515557; e-mail: info@ftmc.lt

https://doi.org/10.15388/vu.thesis.1014
https://orcid.org/0009-0004-4028-5263

VILNIAUS UNIVERSITETAS
FIZINIŲ IR TECHNOLOGIJOS MOKSLŲ CENTRAS

Darija Astrauskytė

Plonų dielektrinių sluoksnių formavimas ant struktūrizuotų elementų naudojant atominių sluoksnių nusodinimo technologiją

DAKTARO DISERTACIJA

Technologijos mokslai,
Medžiagų inžinerija (T 008)

VILNIUS 2026

Disertacija rengta 2022–2026 metais Optinių dangų laboratorijoje, Fizinių ir technologijos mokslų centre.

Mokslinė vadovė – dr. Lina Grinevičiūtė (Fizinių ir technologijos mokslų centras, technologijos mokslai, medžiagų inžinerija, T 008).

Gynimo taryba:

Pirmininkas – dr. Gediminas Račiukaitis (Fizinių ir technologijos mokslų centras, technologijos mokslai, medžiagų inžinerija, T 008).
Nariai:
dr. Paulius Gečys (Fizinių ir technologijos mokslų centras, technologijos mokslai, medžiagų inžinerija, T 008),
dr. Marco Jupé (Hanoverio lazerių centras, Vokietija, gamtos mokslai, fizika, N 002),
dr. Arūnas Kadys (Vilniaus universitetas, technologijos mokslai, medžiagų inžinerija, T 008),
prof. dr. Giedrius Laukaitis (Kauno technologijos universitetas, gamtos mokslai, fizika, N 002).

Disertacija ginama viešame Gynimo tarybos posėdyje 2026 m. gruodžio mėn. 1 d. 10 val. Fizinių ir technologijos mokslų centro Fizikos instituto A140 posėdžių salėje.

Adresas: Savanorių pr. 231, 02300 Vilnius, Lietuva,
Tel. +37064515557; el. paštas: info@ftmc.lt

CONTENTS

List of abbreviations 7
INTRODUCTION 8
1 THE LITERATURE OVERVIEW 16
1.1 Structured optical components 16
1.2 Formation of optical coatings 19
1.2.1 Thermal evaporation 20
1.2.2 Glancing angle deposition 21
1.2.3 Atomic layer deposition 23
1.2.4 Comparison of deposition techniques 30
1.3 Quality of optical components 34
1.3.1 Surface roughness 34
1.3.2 Reflection losses 37
1.3.3 Environmental stability 40
2 EXPERIMENTAL METHODS 44
2.1 Deposition of thin films 44
2.1.1 Atomic layer deposition 44
2.1.2 Glancing angle deposition 44
2.2 Fabrication of micro-optical components 46
2.2.1 Hybrid-polymer micro-optics 46
2.2.2 Inorganic micro-optics 47
2.3 Characterization techniques 47
2.3.1 In-situ quartz crystal monitoring 47
2.3.2 In-situ optical emission spectroscopy 48
2.3.3 Evaluation of optical properties 49
2.3.4 Birefringence imaging 51
2.3.5 Laser-induced damage 51
2.3.6 Evaluation of residual stress 51
2.3.7 Structural and surface morphology analysis 52

2.3.8 Characterization of the micro-optics 53
RESULTS 56
3 IMPROVING QUALITY OF MICRO-OPTICS 56
3.1 Surface smoothing of micro-optical components 57
3.2 Reduction of reflection losses in micro-optical components 63
3.2.1 Optical properties of hybrid-polymer SZ2080™ 63
3.2.2 Optimization of TiO_2 thin film deposition 65
3.2.3 Al_2O_3 film growth on SZ2080™ 69
3.2.4 Single-layer coatings on micro-optics 70
3.2.5 Antireflective coatings on micro-optics 75
3.3 Main results and conclusions 79
4 IMPROVING ENVIRONMENTAL STABILITY OF NANOSTRUCTURED COATINGS 80
4.1 Nanostructured anisotropic LaF_3 coatings 81
4.1.1 Single-layer anisotropic LaF_3 coatings 81
4.1.2 Multilayer anisotropic LaF_3 coatings 84
4.1.3 Waveplates based on nanostructured coatings 86
4.2 Encapsulation of nanostructured anisotropic SiO_2 coatings 90
4.2.1 Analysis of Al_2O_3 films 90
4.2.2 Encapsulation of nanostructured SiO_2 coatings 93
4.2.3 Encapsulation of nanostructured SiO_2 waveplates 99
4.3 Main results and conclusions 106
CONCLUSIONS 108
SANTRAUKA 109
BIBLIOGRAPHY 123
PADĖKA 138
CURRICULUM VITAE 139

List of abbreviations

Abbreviation	Phrase
3D	Three-dimensional
AFM	Atomic force microscopy
ALD	Atomic layer deposition
AR	Antireflective
CVD	Chemical vapor deposition
EBE	Electron beam evaporation
GLAD	Glancing angle deposition
GPC	Growth per cycle
LID	Laser-induced deflection
LIDT	Laser-induced damage threshold
OES	Optical emission spectroscopy
PE-ALD	Plasma-enhanced atomic layer deposition
Ppm	Parts per million
PVD	Physical vapor deposition
QCM	Quartz crystal microbalance
RMS	Root mean square
Sccm	Standard cubic centimeters per minute
SEM	Scanning electron microscopy
TDMAT	Tetrakis(dimethylamino)titanium
TMA	Trimethylaluminum
UV	Ultraviolet

INTRODUCTION

Modern optical and laser systems rely on a wide range of optical components, including lenses, prisms, nonlinear crystals, and optical coatings. These components are employed to control the direction, shape, transmission, reflection, and polarization of a light beam. In addition, advanced photonic systems increasingly require non-standard optics, such as structured optical elements with complex engineered surface topographies, three-dimensional (3D) geometries, or internal microstructures. Examples of structured components include micro-optics, textured surfaces, and nanostructured optical coatings. Such structures can provide additional optical functionalities and enable the development of miniaturized optical systems and micro-lasers [1–3].

Like conventional optical elements, structured components have strict quality requirements because their quality directly impacts the efficiency, reliability, and durability of the overall optical system. Depending on the operation conditions, high-quality optical components mostly should exhibit low optical losses, high resistance to laser radiation, mechanical robustness, and stable optical and physical properties. Achieving these properties requires optimization of both fabrication and post-fabrication processes, including material selection, polishing, etching, and deposition of thin films [4].

One of the primary challenges in the fabrication of high-quality optical components is minimizing optical losses caused by absorption, scattering, and unwanted reflections, which can significantly degrade system performance. In dielectric materials, absorption is primarily determined by the fundamental absorption edge and vibrational modes, but additional absorption can be also introduced by impurities, structural defects, and subsurface damage. Increased absorption is particularly detrimental in high-power laser systems because it can reduce the laser-induced damage threshold (LIDT) [5]. Reflections at optical interfaces decrease transmission efficiency and can also produce ghost images. Such losses are typically minimized employing antireflective (AR) coatings or surface nanostructuring. Scattering losses are primarily caused by surface irregularities and can reduce the transmittance or degrade imaging quality [6,7]. Consequently, optical surfaces are commonly polished or etched to reduce surface roughness.

In addition to optical losses, environmental stability is a critical parameter for optical components. Various optical materials, including porous nanostructured coatings and moisture-sensitive crystals, can exhibit high sensitivity to environmental conditions. Exposure to humidity or organic contamination can alter both optical and physical characteristics, degrading

performance and limiting the applications of these components [8,9]. Dense protective coatings or hydrophobic layers can therefore be required to improve environmental stability.

Physical vapor deposition (PVD) methods are the most developed technologies for producing high-quality optical coatings. However, these processes have limitations when applied to non-planar surfaces. Advances in optics fabrication techniques, including additive manufacturing and lithography, have resulted in increasingly complex component geometries, such as free-form elements and multi-lens systems [7,10,11]. Ensuring the coating conformality on such advanced optical components using conventional PVD methods is becoming increasingly challenging due to directional vapor flux and shadowing effects.

Atomic layer deposition (ALD) has emerged as a promising technique for the formation of dense and conformal thin films on complex 3D substrates. The ALD process is based on sequential, self-limiting surface reactions between gaseous precursors and the substrate [12]. Precise control of film thickness and conformality has enabled ALD applications to highly curved and aspherical lenses, micro-lenses, and micro-objectives [7,13–15]. ALD has been also demonstrated for the formation of films on structured surfaces with intricate geometries, photonic crystals, and complex microstructures [16,17].

This thesis focuses on improving the quality of structured optical elements. First, the reduction of surface roughness and reflection losses of micro-optical components using conformal ALD coatings formation is investigated. Second, the environmental stability of porous nanostructured coatings is improved either by producing porous coatings from material with lower humidity sensitivity or by employing ALD encapsulation.

The objective of the thesis

The objective of this thesis was to enhance the quality of structured elements using atomic layer deposition, through the formation of conformal thin films for optical loss reduction of micro-optics and the environmental stabilization of porous nanostructured coatings

The scientific tasks of the thesis

1. To evaluate the effectiveness of atomic layer deposition conformal coatings to reduce the surface roughness of micro-optical components while maintaining component geometry.

2. To investigate the formation of conformal antireflective coatings on complex hybrid-polymer micro-optical components using atomic layer deposition.
3. To develop nanostructured LaF_3-based waveplates and evaluate their environmental stability.
4. To improve the environmental stability of nanostructured anisotropic SiO_2 coatings using atomic layer deposition encapsulation.

Scientific novelty and relevance of the work

- Surface smoothing of micro-optical components by deposition of conformal films using atomic layer deposition was demonstrated. Compared with previously reported studies, surface roughness reduction was investigated for substrates exhibiting significantly higher initial roughness (> 100 nm compared with < 10 nm reported in the literature). Furthermore, surface smoothing of non-planar substrates was investigated, showing that atomic layer deposition can be applied to reduce surface roughness of complex components without distorting their initial geometry.
- The impact of coatings produced by atomic layer deposition on the geometry of hybrid-polymer micro-optical components was evaluated. It was observed that, in addition to coating stress, other effects may contribute to induced changes in component geometry, including possible penetration of precursors into the near surface region of the porous hybrid-polymer substrate. It was demonstrated that low stress conformal antireflective coatings produced by atomic layer deposition can be applied to reduce reflection losses of hybrid-polymer micro-optical components without distorting their geometry.
- The formation of nanostructured anisotropic lanthanum fluoride coatings was investigated, and improved short-term environmental stability of nanostructured LaF_3-based waveplates was demonstrated.
- Encapsulation of nanostructured SiO_2 coatings using atomic layer deposition was investigated. Environmental stabilization of nanostructured SiO_2 waveplates was achieved using plasma-enhanced atomic layer deposition of Al_2O_3 without damaging the underlying porous structure. Furthermore, local laser annealing with gradual fluence ramping has been applied to improve the laser resistance of encapsulated waveplates.

Statements to defend

1. Al_2O_3 films produced by atomic layer deposition can reduce the surface roughness of micro-optics without measurable changes in their geometry, provided that the film thickness is optimized according to the initial surface topography.
2. Conformal low stress bilayer TiO_2/Al_2O_3 antireflective coatings produced by atomic layer deposition minimize reflection losses in hybrid-polymer micro-optical components with multiple surfaces, while causing no distortion of the geometry.
3. Porous nanostructured LaF_3 coatings exhibit improved short-term stability of retardance under varying humidity conditions compared to porous nanostructured SiO_2 coatings.
4. Plasma-enhanced atomic layer deposition of Al_2O_3 enables encapsulation of porous nanostructured SiO_2 coatings, reducing the sensitivity of their retardance to varying humidity conditions without inducing cracking of the porous structure.

Approbation

Scientific articles directly related to the thesis (peer-reviewed and referenced in Clarivate Analytics Web of Science):

1. **D. Astrauskyte**, M. Slipkauskas, S. Tumenas, A. Selskiene, L. Ramalis, L. Grineviciute "Performance and Stability Evaluation of LaF_3 Thin-Film Waveplates for High-Power 266 nm Laser Applications", *Nanoscale* **18**, 4127–4134 (2026).
2. **D. Astrauskytė**, K. Galvanauskas, D. Gailevičius, M. Drazdys, M. Malinauskas, L. Grineviciute "Anti-Reflective Coatings Produced via Atomic Layer Deposition for Hybrid Polymer 3D Micro-Optics", *Nanomaterials* **13**, 2281 (2023).
3. **D. Astrauskyte**, L. Ramalis, L. Grinevičiūtė "Environmental stabilization of anisotropic nanostructured SiO_2 waveplates via plasma-enhanced atomic layer deposition" (Submitted).
4. **D. Astrauskytė**, D. Ladika, K. Galvanauskas, I. A. Petsi, M. Česnulis, D. Dapšys, G. Balčas, D. Gailevičius, L. Grineviciute, G. Zyla, M. Malinauskas "High-Transparency 3D Micro-Optics of Hybrid-Polymer SZ2080™ via Multiphoton Lithography and Atomic Layer Deposition" Opt. Open 104228 (Submitted).

Publications in the conference proceedings directly related to the thesis:

1. **D. Astrauskyte**, L. Ramalis, L. Grinevičiūtė, “Encapsulation of Porous Nanostructured Waveplates Using Atomic Layer Deposition”. In Proceedings of the Advances in Optical Thin Films IX; Lumeau, J., Wienke, A., Tilsch, M.K., Eds.; SPIE: Strasbourg, France, May 28 2026; p. 52
2. **D. Astrauskyte**, M. Slipkauskas, L. Grineviciute, “Functionalization of Structured Optical Components via Atomic Layer Deposition”. In Proceedings of the Oxide-based Materials and Devices XVI; Teherani, F.H., Rogers, D.J., Eds.; SPIE: San Francisco, United States, March 19 2025; p. 22.
3. **D. Astrauskyte**, K. Galvanauskas, D. Gailevicius, M. Drazdys, M. Malinauskas, L. Grineviciute, “Deposition of Thin Films on Hybrid-Polymer 3D Micro-Optics Using Atomic Layer Deposition”. In Proceedings of the Advances in Optical Thin Films VIII; Lequime, M., Ristau, D., Eds.; SPIE: Strasbourg, France, June 24 2024; p. 6.
4. **D. Astrauskyte**, K. Galvanauskas, D. Gailevicius, M. Drazdys, M. Malinauskas, L. Grineviciute, “Deposition of Antireflective Coatings on 3D Micro-Optics Using Atomic Layer Deposition”. In Proceedings of the Functional Material Applications: From Energy to Sensing; Kean, A.H., Bhalla, N., Eds.; SPIE: Glasgow, United Kingdom, November 30 2023; p. 19.

Scientific articles not directly related to the thesis (peer-reviewed and referenced in Clarivate Analytics Web of Science):

1. H. Mu, D. Smith, T. Katkus, N. H. A. Le, D. Stonyte, D. Gailevičius, D. Kapsaskis, A. D. Frate, T. S. Bedi, D. Narbutis, V. Anand, **D. Astrauskyte**, L. Grineviciute, S. H. Ng, K. Glazebrook, J. Lawrence, S. Juodkazis, “3D Free-Form Optical Lens — Miniaturised Fibre Couplers for Astrophotonics”. *Optics & Laser Technology* **190**, 112960 (2025).
2. L. Grineviciute, S. Melnikas, J. Nikitina, M. Drazdys, A. Selskis, **D. Astrauskytė**, “Optical Coating Deposition on Submicron-Patterned Surfaces”. *Coatings* **15**, 372 (2025).
3. M. Drazdys, E. Bužavaitė-Vertelienė, **D. Astrauskytė**, Z. Balevičius, “Atomic Layer Deposition for Tailoring Tamm Plasmon-Polariton with Ultra-High Accuracy”. *Coatings* **14**, 33 (2023).

Conference presentations directly related to the thesis:

1. **D. Astrauskyte**, L. Ramalis, L. Grineviciute “Encapsulation of porous nanostructured waveplates using atomic layer deposition”, SPIE Optical Systems Design 2026, 2026 April 12–16, Strasbourg, France (oral presentation).
2. **D. Astrauskyte**, L. Ramalis, L. Grineviciute “Humidity-insensitive porous nanostructured waveplates via glancing angle deposition and atomic layer deposition”, Symposium on Optical Coatings for Laser Applications OCLA 2026, 2026 March 26, Buchs, Switzerland (oral presentation).
3. **D. Astrauskyte**, L. Grineviciute “Nanostruktūrizuotų dangų stabilizavimas naudojant atominių sluoksnių nusodinimo technologiją”, FizTech 2025, 2025 October 21–22, Vilnius, Lithuania (oral presentation).
4. **D. Astrauskyte**, L. Ramalis, L. Grineviciute “Stabilization of all-silica waveplates via atomic layer deposition”, Advanced Solid State Lasers Conference (ASSL) 2025, 2025 October 19–23, Prague, Czech Republic (poster presentation).
5. **D. Astrauskytė**, K. Galvanauskas, D. Gailevičius, M. Drazdys, M. Malinauskas, L. Grinevičiūtė “Antireflective coatings for multi-level micro-optics produced by atomic layer deposition”, Symposium on Optical Coatings for Laser Applications OCLA 2025, 2025 May 8, Vilnius, Lithuania (poster presentation).
6. **D. Astrauskyte**, M. Slipkauskas, L. Grineviciute “Functionalization of structured optical components via atomic layer deposition”, SPIE Photonics West 2025, 2025 January 25–31, San Francisco, United States (oral presentation).
7. **D. Astrauskytė**, K. Galvanauskas, D. Gailevičius, M. Drazdys, M. Malinauskas, L. Grinevičiūtė “Skaidrinančių dangų formavimas ant 3D mikrooptinų komponentų naudojant atominių sluoksnių nusodinimo technologiją”, FizTech 2024, 2024 October 15–17, Vilnius, Lithuania (oral presentation).
8. **D. Astrauskytė**, K. Galvanauskas, D. Gailevičius, M. Drazdys, M. Malinauskas, L. Grinevičiūtė “Reducing reflection losses in multi-level micro-optics made by femtosecond laser direct writing”, Summer School on Ultra-short Pulse Lasers Applications in Material Processing UPLAMP 2024, 2024 July 1–6, Vilnius, Lithuania (oral presentation).

9. **D. Astrauskytė**, K. Galvanauskas, D. Gailevičius, M. Drazdys, M. Malinauskas, L. Grinevičiūtė "Reducing reflection losses in multi-level micro-optics made by femtosecond laser direct writing", UPLAMP 2024 Summer School on Ultra-short Pulse Lasers Applications in Material Processing, 2024 July 1–6, Vilnius, Lithuania (poster presentation).
10. **D. Astrauskytė**, K. Galvanauskas, D. Gailevičius, M. Drazdys, M. Malinauskas, L. Grinevičiūtė "Deposition of thin films on hybrid-polymer 3D micro-optics using atomic layer deposition", SPIE Optical Systems Design 2024, 2024 April 7–11, Strasbourg, France (oral presentation).
11. **D. Astrauskytė**, K. Galvanauskas, D. Gailevičius, M. Drazdys, M. Malinauskas, L. Grinevičiūtė "Deposition of antireflective coatings on 3D micro-optics using atomic layer deposition", SPIE Photonex 2023, 2023 October 24–26, Glasgow, Scotland (oral presentation).
12. **D. Astrauskyte**, K. Galvanauskas, D. Gailevicius, M. Drazdys, R. Drazdys, M. Malinauskas, L. Grineviciute "Plonų sluoksnių formavimas ant 3D mikrostruktūrų paviršių naudojant atominių sluoksnių nusodinimo technologiją", FizTech 2022, 2022 October 19–20, Vilnius, Lithuania (poster presentation).
13. **D. Astrauskyte**, K. Galvanauskas, D. Gailevicius, M. Drazdys, R. Drazdys, M. Malinauskas, L. Grineviciute "Deposition of optical coatings on micro-optics using atomic layer deposition", Functional Inorganic Materials 2022, 2022 October 6–8, Vilnius, Lithuania (poster presentation).

Contribution of the author and co-authors

The author performed all thin film depositions using atomic layer deposition, as well as the deposition of nanostructured SiO_2 coatings. The author conducted the majority of the spectrophotometric measurements, coating designs, and optical characterization. The author also performed all optical emission spectroscopy, atomic force microscopy, interferometry, focal length, optical profilometry, and environmental stability measurements. The author participated in the analysis of the results.

Dr. L. Grinevičiūtė supervised the work, advised on arising issues with experiments and the analysis of the results.

Dr. L. Ramalis and Dr. R. Buzelis performed laser-induced damage threshold and absorption measurements of the coatings.

M. Slipkauskas performed the deposition of nanostructured LaF_3 coatings and carried out the majority of their characterization.

Dr. A. Selskienė performed scanning electron microscopy measurements of the nanostructured coatings.

Dr. S. Tumėnas provided ellipsometry measurements.

Dr. D. Gailevičius prepared the spin-coated and drop-casted hybrid-polymer SZ2080™ samples.

Prof. Dr. M. Malinauskas, Dr. D. Ladika, Dr. G. Zyla, Dr. D. Gailevičius, and K. Galvanauskas contributed at different stages to the fabrication of hybrid-polymer micro-optical components using multiphoton lithography done by direct laser writing. They also provided scanning electron microscopy and transmittance measurements of the fabricated micro-optical components.

Dr. D. Smith and Prof. Dr. S. Juodkazis research group contributed to the fabrication of inorganic micro-lenses using laser back-side ablation and scanning electron microscopy measurements.

1 THE LITERATURE OVERVIEW

1.1 Structured optical components

The increasing complexity of photonic systems, together with the growing demand for compact and highly integrated optical devices, has led to the development of non-standard optical components with micro- or nanoscale engineering. An important group of these components comprises structured optical elements, which are characterized by complex surface structures, surface topographies, or internal morphologies. In contrast to conventional components, the optical functionality of structured elements is primarily determined by their surface topography or internal morphology. By tailoring their dimensions, geometry, and morphology, it is possible to manipulate the propagation, amplitude, phase, and polarization of light. Optical elements that can be classified as structured components include micro-optics, metasurfaces, structured surfaces, and nanostructured coatings. This overview focuses on micro-optical components and nanostructured coatings.

Micro-optics are optical components with dimensions ranging from several micrometers to the sub-millimeter scale. The development of micro-optical elements has been enhanced by the continuing miniaturization of photonic devices, which requires optical components capable of maintaining high optical performance despite decreasing sizes. According to the dominant mechanism determining light propagation, micro-optical components are commonly classified as refractive, reflective, or diffractive. Refractive elements include single micro-lenses [18,19], micro-lens arrays [20], micro-prisms, whereas reflective micro-optics comprise micro-mirrors [10]. Common examples of diffractive micro-optical components include diffraction gratings and diffractive lenses [21,22].

Rapid developments in micro-fabrication technologies have expanded the optical design flexibility. Advanced manufacturing techniques, such as laser ablation, laser 3D printing, or nanoimprint lithography, facilitate the fabrication of complex 3D microstructures. These methods can be employed to manufacture free-form optics [11] (Figure 1a), photonic crystals [17,23] (Figure 1b), and stacked optical elements [2,7,22] (Figure 1c).

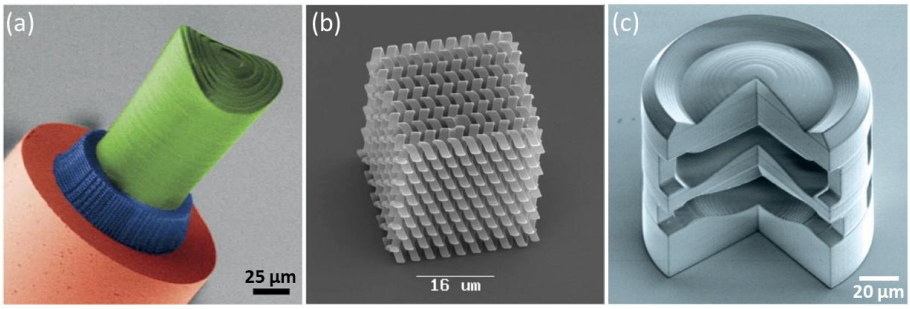


Figure 1. Scanning electron microscopy (SEM) images of complex microstructures: (a) colorized SEM image of a free-form optical component [11], (b) photonic crystal [23], and (c) micro-objective [2].

Owing to their small size and optical performance, micro-optical components have enabled the miniaturization and integration of optical systems. Consequently, they have become essential in numerous applications, including optical communications, imaging systems, astrophotonics, and biomedical instruments. For example, micro-lens arrays are widely used in wavefront sensors and high-resolution cameras [24,25], while single micro-lenses are frequently employed for light coupling in optical fibers [15,19]. Moreover, micro-objectives are essential components for high-resolution imaging systems, such as medical endoscopes and drone cameras [2,3].

Another class of structured optical elements is nanostructured coatings, whose optical performance can be tailored by engineering their internal structure or surface topography. For example, structural modifications can include the introduction of porosity [26] (Figure 2a), periodic refractive index modulations [27] (Figure 2b), or surface patterns [28,29] (Figure 2c). Nanostructured coatings can be produced using advanced thin film deposition techniques or combinations of thin film deposition and surface structuring processes. Glancing angle deposition (GLAD) and sol-gel methods are widely employed to tailor coating porosity and internal microstructure [26,30]. More complex designs are typically achieved through multistep fabrication approaches, such as depositing coatings onto patterned substrates or texturing the coating surface. The surface structure of the coating is commonly modified using techniques such as electron beam lithography, laser processing, and ion etching [28,29].

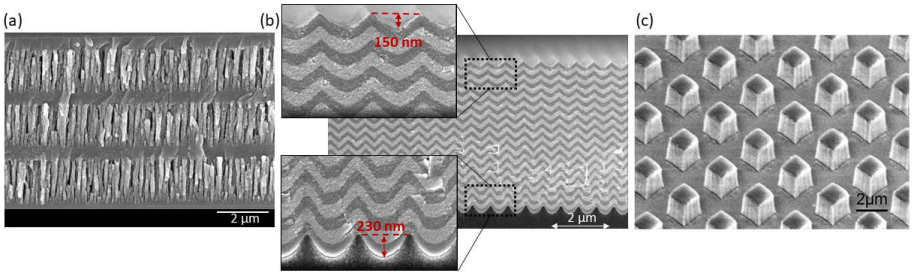


Figure 2. SEM images of nanostructured coatings: (a) porous nanostructured coating [31], (b) periodically modulated coating [27], and (c) patterned coating [28].

Structural control provides additional degrees of freedom for manipulating the interaction of light with the nanostructured coating, thereby extending its optical functionalities compared with conventional homogeneous coatings. Consequently, such coatings are used to produce both conventional optical coatings, such as antireflective and highly reflective coatings [32,33], and advanced optical elements, including polarizers [34], spatial filters [27], photonic crystals [35], and thin film waveplates [31].

Waveplates are among the most widely used optical components for polarization state control, which relies on birefringent materials. When a light beam propagates through a birefringent medium, the two orthogonal polarization components experience different refractive indices. As a result, a phase difference, referred to as the phase retardance, is introduced between the orthogonal polarization components. The resulting retardance determines the polarization transformation introduced by the waveplate and can be expressed as:

$$\phi = \frac{2\pi d}{\lambda}|n_o - n_e|$$

where ϕ is the retardance, d is the thickness of the anisotropic material, λ is the wavelength of light, and n_o and n_e are the refractive indices experienced by the ordinary and extraordinary components, respectively.

Depending on the introduced retardance, waveplates are commonly classified as half-wave (λ/2) plates and quarter-wave (λ/4) plates (Figure 3a). Half-wave plates are used for polarization rotation, whereas quarter-wave plates are used for converting the polarization state of light, for example, linear polarization can be converted into circular polarization (Figure 3b). Moreover, waveplates can be categorized into zero-order and multiple-order components, depending on the thickness of the birefringent material. Zero-order waveplates provide the required phase retardance, whereas multiple-order waveplates

introduce the required retardance with one or more additional integer multiples of 2π [5].

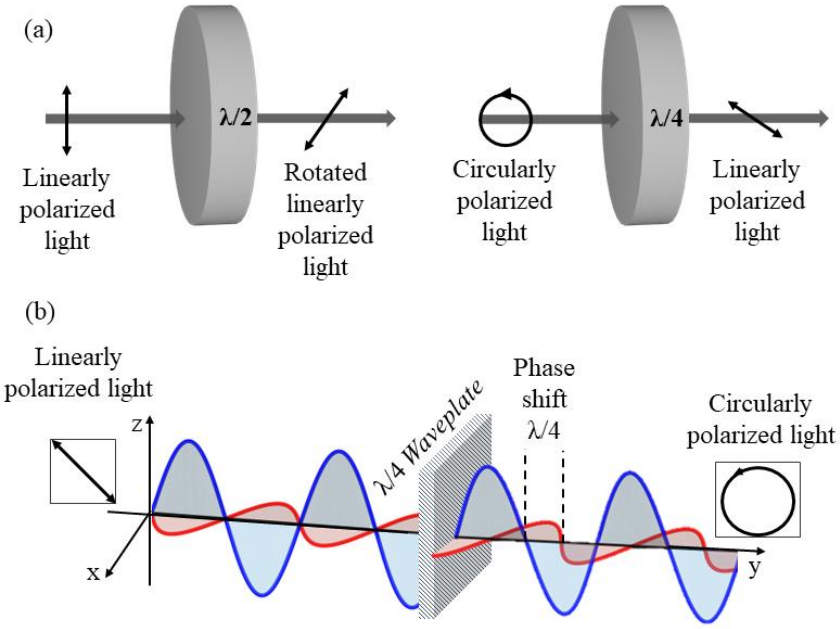


Figure 3. (a) Illustration of light behavior in half-wave and quarter-wave waveplates and (b) illustration of light propagation through a quarter-wave waveplate resulting in circularly polarized light.

1.2 Formation of optical coatings

Optical coatings are single-layer or multilayer thin film structures deposited on optical components, such as flat glass substrates, non-linear crystals, and lenses, to control transmittance, reflectance, and polarization. Most optical coatings consist of alternating high and low refractive index layers, designed to achieve the desired optical performance for specific wavelength ranges and applications. The operation of optical coatings is based on thin film interference, where light waves reflected from different interfaces interfere constructively or destructively to achieve the required optical properties. Common types of optical coatings include AR coatings, highly reflective coatings, polarizers, filters, beam splitters, and etc.

PVD is one of the primary techniques used for producing optical coatings. In PVD processes, a solid source material is vaporized, transferred through a vacuum, and condensed onto a substrate to form a solid thin film. According to the method used to generate vapor, PVD techniques can be broadly classified into evaporation and sputtering processes. Evaporation techniques include thermal evaporation and electron beam evaporation (EBE), while

sputtering techniques include magnetron sputtering and ion beam sputtering. ALD is an alternative technology for producing optical coatings due to its precise thickness control and conformal deposition on complex 3D optical elements.

1.2.1 Thermal evaporation

Thermal evaporation is based on resistive heating of the source material to induce evaporation (Figure 4a). The source material is typically placed in a metal evaporation boat through which a high electric current, ranging from several tens to several hundreds of amperes, is passed to generate heat. The resulting vapor flux travels through the vacuum chamber and condenses on the substrate, forming a thin film. Thermal evaporation is performed under high vacuum conditions to minimize collisions between the evaporated atoms and residual gas molecules in the vacuum chamber. Evaporation boats are fabricated from metals, such as molybdenum, tungsten, or tantalum, whose melting temperatures significantly exceed those of the evaporated materials. Nevertheless, thermal evaporation is generally limited to materials with relatively low melting points. Furthermore, chemical reactions between the source material and the evaporation boat can occur, introducing impurities into the deposited film and degrading its optical properties [36].

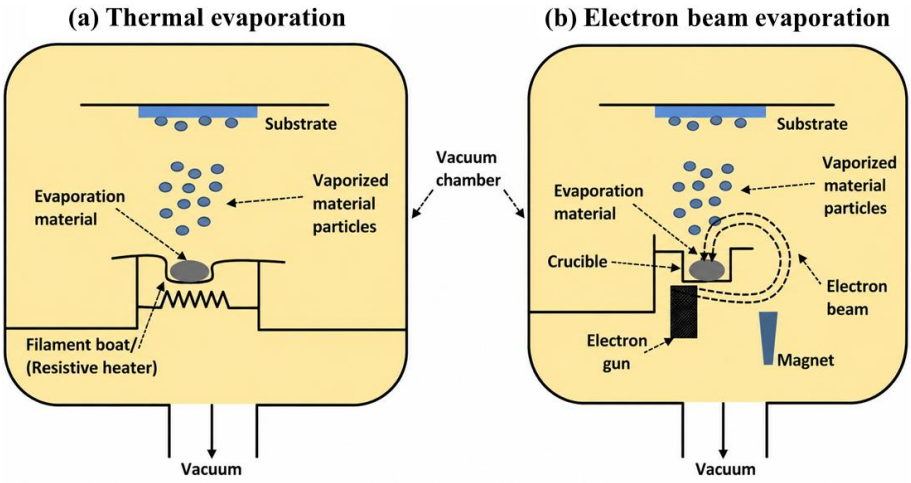


Figure 4. Schematic representation of (a) thermal evaporation and (b) electron beam evaporation [36].

In contrast, EBE employs a focused beam of high-energy electrons to locally heat and evaporate the source material (Figure 4b). The source material is conventionally placed in a water-cooled crucible, while electrons emitted

from a heated filament are accelerated by an electric field and focused onto the source material using an electromagnetic field. During bombardment with electron beam, the kinetic energy of the incident electrons is converted into thermal energy, resulting in localized heating and evaporation of the source material. The generated vapor is then transported through the vacuum chamber and deposited onto the substrate to form a thin film. EBE is particularly suitable for evaporating high melting point materials that are difficult to evaporate using resistive heating. In addition, localized heating of the source material minimizes interactions with the crucible, thereby reducing the risk of contamination compared with resistive heating evaporation [36,37].

1.2.2 Glancing angle deposition

More complex coating morphologies can be achieved by controlling the direction of the incident vapor flux with respect to the normal axis of the substrate. GLAD is a PVD technique in which an oblique incidence of vapor flux toward the substrate is employed (Figure 5a). Unlike conventional PVD processes, where the vapor flux is directed along the substrate normal and relatively dense films are produced, the oblique incidence used in GLAD leads to the growth of highly porous nanostructured coatings. During the GLAD process, the substrate is tilted at an oblique angle, resulting in a ballistic shadowing effect and the formation of a nanocolumnar film microstructure. During the initial stages of film growth, incoming vapor atoms condense on the substrate, forming nuclei (Figure 5b). As deposition proceeds, these nucleation sites receive a higher fraction of the incoming vapor flux, while the regions behind the nuclei become shadowed and receive considerably less deposited material (Figure 5c). This shadowing process promotes preferential growth of the nucleation sites, resulting in the formation of separated columns (Figure 5d) [26].

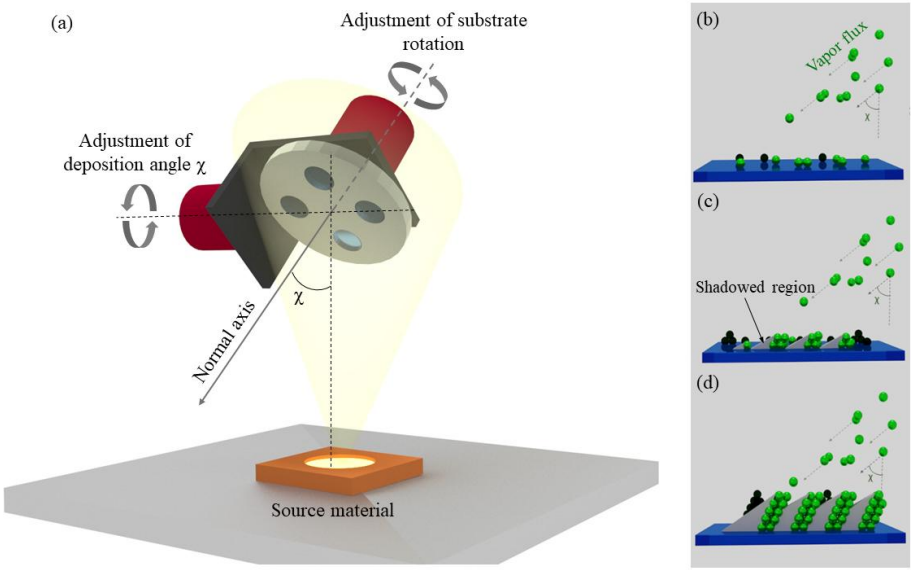


Figure 5. Schematic illustration of (a) glancing angle deposition and stages of nanocolumnar film growth: (b) initial nucleation, (c) continued growth of the initial nuclei and development of shadowed regions, and (d) preferential growth of the nuclei, leading to the formation of a nanocolumnar film microstructure [38].

The growth of the porous nanostructured films is strongly influenced by adatom surface diffusion. Therefore, GLAD is performed at relatively low substrate temperatures to suppress adatom mobility. Limited surface diffusion prevents the migration of atoms into shadowed regions, thereby enhancing the shadowing effect and promoting the growth of a porous columnar microstructure. GLAD can be implemented using various PVD techniques, including thermal evaporation, EBE, sputtering, and pulsed laser deposition [39–41]. Among these, evaporation-based techniques are most frequently employed because during such processes higher collimation of the vapor flux is obtained which enhances the self-shadowing effect [26].

The morphology of nanostructured GLAD coatings can be tailored at the nanoscale by varying the deposition angle and the substrate rotation around its normal axis. By adjusting these parameters, various microstructures can be deposited, ranging from nanocolumnar and helical to zigzag geometries. For example, oblique angle deposition without substrate rotation produces inclined nanocolumns oriented toward the incident vapor flux [39] (Figure 6a). Continuous slow rotation of the substrate leads to the formation of a helical film morphology [42] (Figure 6b), whereas periodic changes in the deposition angle produce zigzag structures [26] (Figure 6c).

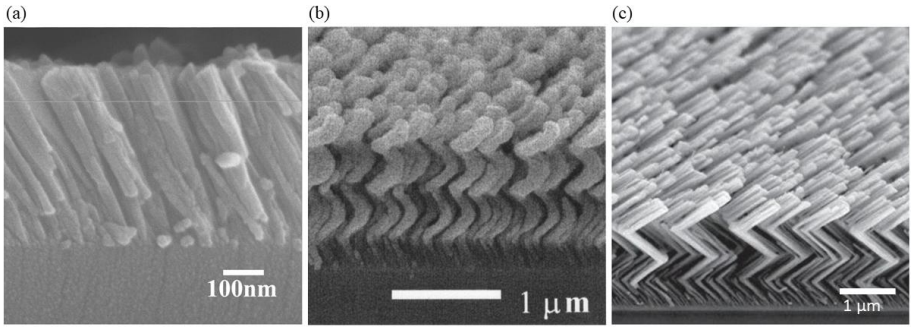


Figure 6. Cross-sectional SEM images of nanostructured coatings exhibiting different internal morphologies: (a) inclined nanocolumnar [39], (b) helical [42], and (c) zigzag [26] microstructures.

Furthermore, the GLAD technique enables the formation of birefringent coatings with direction-dependent optical properties originating from the film microstructure. Consequently, anisotropic GLAD coatings have been widely investigated for potential applications such as thin film waveplates [31,43,44]. For instance, tilted nanocolumnar films typically consist of columns with an elliptical cross-section, resulting in different effective refractive indices along two orthogonal optical axes [39]. Optical anisotropy has been also reported for helical and zigzag morphologies [42,45]. Moreover, anisotropy can be further enhanced through more complex substrate motions during deposition. One approach is serial bideposition, in which the substrate is periodically rotated by 180° about its normal axis while maintaining a constant deposition angle [46]. Rapid half-turn substrate rotations result in a small subdeposited thickness of a few nanometers, typically using rotation intervals of several seconds. Serial bideposition produces elliptical columnar structures aligned perpendicular to the substrate plane, thereby inducing birefringence [26].

1.2.3 Atomic layer deposition

Over the past few decades, ALD has emerged as a promising alternative to PVD methods for producing optical coatings. ALD was originally developed and patented in the 1970s as atomic layer epitaxy by T. Suntola and J. Antson for the deposition of crystalline thin films, such as ZnS, SnO_2, and GaP [47]. The term “ALD” became widely used as the technique was extended to the deposition of amorphous thin films. Initially, ALD was applied in the semiconductor and microelectronics industries [48,49]. Although optical applications were not the primary focus of early ALD research, its precise film thickness control and capability to produce conformal coatings on surfaces

with intricate topographies led to its application for optical coatings in the late 1990s [50,51].

ALD is a modified chemical vapor deposition (CVD) technique used for thin film deposition through surface reactions. In conventional CVD, gaseous precursors are introduced simultaneously, and the thin film is formed through continuous gas-phase and surface reactions. In contrast, ALD employs a sequential and alternating precursor dosing approach to enable self-limiting surface reactions while preventing gas-phase reactions between the precursors. These self-limiting chemical reactions enable conformal coating deposition on complex substrates. ALD proceeds in cycles, with each cycle producing approximately one atomic layer [12]. A conventional ALD cycle consists of four steps, as illustrated in Figure 7:

1. Precursor introduction: a precursor is introduced into the reaction chamber for a specific pulse duration. ALD precursors are typically metal-organic or halide-based compounds that undergo chemisorption onto available surface functional groups (commonly hydroxyl groups). The chemisorption of the precursors continues until all surface groups are occupied and saturation is achieved.

2. Purge step: reaction by-products and unreacted precursor molecules are removed from the reactor using an inert gas flow (e.g., N_2 or Ar).

3. Co-reactant introduction: a reactive gas or plasma species (e.g., H_2O, O_2 plasma, O_3) are introduced into the reactor to react with the adsorbed precursor, forming the desired material layer (e.g., metal oxide). During this surface reaction, precursor ligands are released, and the surface is re-saturated with hydroxyl groups.

4. Purge step: residual oxidizers and reaction byproducts are purged from the reactor, preparing the surface for the next deposition cycle.

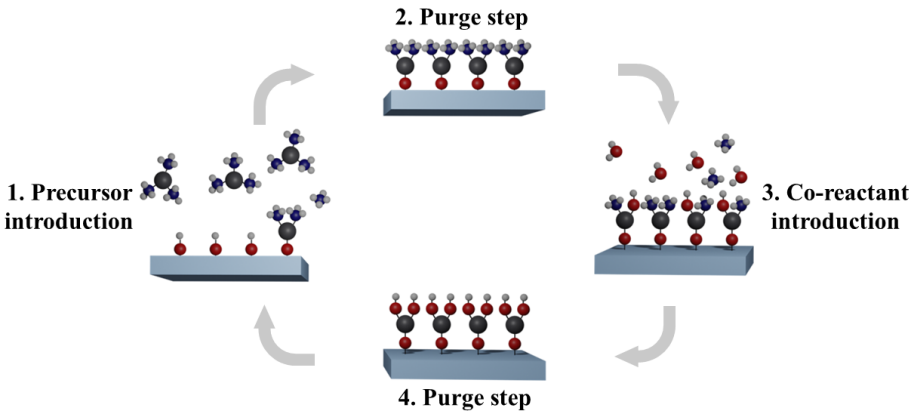


Figure 7. Schematic representation of a conventional ALD cycle.

Throughout the conventional ALD process, a continuous flow of an inert carrier gas is maintained to transport precursors to the substrate and remove reaction by-products from the reactor efficiently.

ALD film growth strongly relies on the adsorption of precursor molecules onto the substrate surface. Adsorption can be classified as physisorption or chemisorption depending on the strength of the interaction between the adsorbed molecules and the substrate surface. Physisorption is characterized by relatively weak interactions, with interaction energies ranging from approximately 0.01 eV to 0.1 eV [52,53]. It is primarily caused by van der Waals forces, which arise from interactions between transient, induced, or permanent electric dipoles. Generally, physisorption is reversible, meaning that adsorbed species can desorb from the surface depending on temperature and pressure. In contrast, chemisorption involves the formation of chemical bonds between the precursor and the surface. Chemisorption is characterized by significantly stronger interactions and is generally irreversible. During ALD, both chemisorption and physisorption may occur. Although for a controlled, self-limiting ALD process, chemisorption is a crucial, while minimizing physisorption is desirable [53].

The ALD growth rate is commonly expressed as growth per cycle (GPC), which refers to the thickness of the material deposited per ALD cycle [54]. The effective deposition rate (film thickness per unit time) can be used to compare ALD with other deposition methods. Typically, the effective deposition rates for ALD range from 20 nm/h to 180 nm/h, but these values can vary significantly depending on GPC, ALD cycle duration, and reactor design [12,55]. GPC is primarily determined by the precursor chemistry and deposition temperature, while cycle duration is largely influenced by reactor design. Additionally, the chemical reaction rates, precursor pulse duration, and purge durations significantly impact film growth kinetics. Precursor pulse durations must be optimized to achieve reaction saturation, ensuring self-limiting growth and complete surface coverage [56]. Saturation can be determined by evaluating the GPC dependence on pulse duration (Figure 8a). Additionally, precursor decomposition should be avoided, as it leads to CVD-like film growth, compromising the uniformity of the deposited coating. Purge durations highly depend on the deposition temperatures and molecular properties of the precursors. Excessively long purge durations can be required at low deposition temperatures to prevent condensation and ensure complete removal of byproducts and residual precursor from the reactor.

During an ideal ALD process, one monomolecular layer is deposited in each cycle [57]. However, in practice, sub-monolayer growth per cycle is typically observed due to limited availability of reaction sites and steric

hindrance. Precursor ligands are often relatively large, partially blocking the chemisorption sites, creating steric hindrances. As a result, the formation of a complete monolayer is rarely achieved, with GPC values ranging from 15% to 50% of a full monolayer per cycle [55].

Another essential characteristic of the ALD process is the ALD window (Figure 8b), which defines the optimal temperature range for ideal ALD growth. At low temperatures, precursors may condense or exhibit incomplete surface reactions due to insufficient thermal energy. Conversely, at high temperatures, precursor decomposition may occur, leading to uncontrolled film growth or film contamination. Furthermore, high deposition temperatures can increase desorption of surface species, reducing the number of available reaction sites [49].

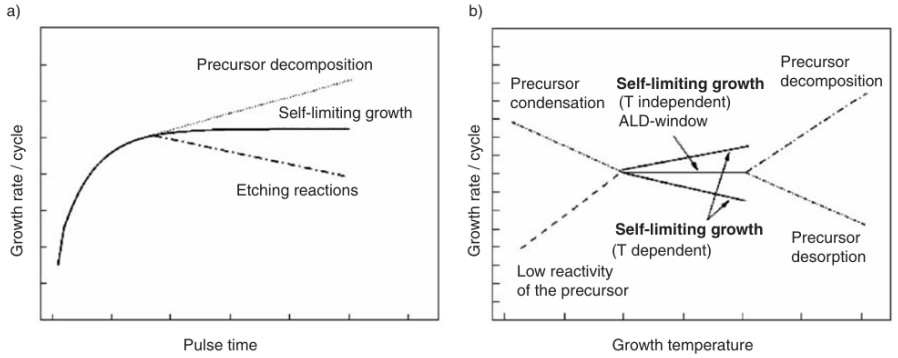


Figure 8. Comparison of ALD and non-ALD film growth behaviors: (a) schematic representation of GPC as a function of precursor pulse duration and (b) schematic representation of GPC as a function of deposition temperature [12].

In general, key ALD process parameters, such as precursor pulse and purge durations, are influenced by numerous factors including precursor chemistry, reactor design, carrier gas, deposition temperature, etc. These parameters may critically affect film uniformity, conformality, and composition, since deviations from optimal conditions can lead to CVD-like growth, incomplete reactions, or precursor decomposition. Also, excessively long pulse and purge durations result in inefficient precursor usage and extended deposition times. Therefore, optimizing deposition parameters is inherently complex and time consuming, necessitating the use of in-situ film monitoring techniques. For instance, a quartz crystal microbalance (QCM) is widely employed to measure film thickness and GPC as well as to evaluate reaction saturation [58], though it is highly sensitive to variations in temperature, pressure and gas flow [59].

Materials

The surface chemistry of ALD is based on chemical reactions between precursors and surface functional groups. To ensure a cost-effective, well-controlled, and non-CVD-like process, ALD precursors must satisfy several criteria. Although precursors may be in solid, liquid, or gaseous form, they must exhibit sufficient volatility and high vapor pressure. Thermal stability is also essential to prevent precursor decomposition, which can lead to undesired CVD-like film growth or contamination. Moreover, precursors should be highly reactive with the substrate surface to ensure efficient material utilization [60]. Common precursor families include halides, alkoxides, alkyls, and alkylamides, each of which can exhibit structural variations that influence the deposition process, chemical reaction mechanisms, film growth kinetics, and film properties [49,61]. For example, when depositing SiO_2 using different aminosilane precursors, the GPC can vary from 0.7 Å/cycle to 1.25 Å/cycle [61].

In addition, the reaction by-products must be volatile to allow efficient purging from the reactor without re-adsorption, and ideally, they should be inert to avoid any unwanted side reactions with the precursors. Furthermore, these by-products should be non-corrosive to prevent potential etching during the deposition process [60].

Oxidizing agents

The ALD processes are often categorized based on the energy source driving the chemical reactions, including thermal ALD and plasma-enhanced ALD (PE-ALD). Each method offers distinct advantages depending on precursor reactivity, deposition temperatures, and desired film properties.

Thermal ALD is based on thermally activated surface reactions, such as ligand exchange, oxidation, and reduction. Various oxidizing agents including water (H_2O), ozone (O_3), hydrogen peroxide (H_2O_2), alcohols, and alkoxides, can be used to induce surface reactions. Among these, water is the most commonly used oxidizer due to its availability, stability and low cost, as it does not require additional equipment and complex reactor designs. However, water-based ALD processes frequently require higher deposition temperatures (typically 150 °C – 350 °C) to achieve sufficient reactivity. Typically, thermal ALD provides high uniformity and conformality of the coatings, although these properties can depend on the specific ALD process [62].

Ozone serves as an alternative highly reactive oxidizer, particularly when water exhibits insufficient reactivity with certain precursors. Compared to water-based ALD, ozone-based ALD reduces purge durations due to the high

volatility of ozone molecules, making them easier to remove from the reactor, especially at low deposition temperatures. Since purge duration is a critical factor in determining ALD cycle duration, ozone-based ALD can significantly enhance process efficiency by reducing overall deposition time. Additionally, ozone-based ALD results in lower hydrogen and hydroxyl incorporation in the final film [63]. However, at lower deposition temperatures, ozone-based ALD may lead to the formation of porous films with lower refractive indices compared to water-based coatings [63,64]. Conversely, at high deposition temperatures, ozone thermally decomposes more rapidly, limiting its effectiveness as an oxidizing agent [65]. Despite enabling lower deposition temperatures and expanding the range of accessible precursors, ozone-based ALD requires an ozone generator, adding additional equipment costs.

PE-ALD utilizes plasma-generated highly reactive plasma species, often referred to as plasma radicals, to enhance film growth. Plasma consists of a mixture of species, including neutral radicals (e.g., O), ions (e.g., O_2^+, O^+), electrons, and photons. Plasma is typically generated using an electric field, which accelerates electrons. These high energy electrons collide with the gas-phase molecules and atoms, inducing ionization, excitation and dissociation. This process creates highly reactive radicals and ions that strongly influence surface chemistry and film growth. Furthermore, excited molecules and atoms returning to their ground state emit photons, which can have enough energy to break chemical bonds, further affecting surface reactions [66]. Plasma emission can also be utilized in optical emission spectroscopy (OES) to analyze ALD reaction chemistry in real time [67]. In PE-ALD, ion bombardment transfers additional energy to the surface, enhancing reaction rates, surface diffusion, chemical bond breaking, crystallization, atomic migration, and sputtering [68]. The impact of ion bombardment on the film growth can be both beneficial and destructive, depending on ion energy and the desired film properties. During ALD processes, ion energy typically ranges from 15 eV to 300 eV, depending on plasma source configurations and substrate voltage biasing.

Generally, low (10 – 30 eV) and intermediate (≈ 100 eV) ion energies have been observed to positively influence film growth and material properties [69]. Ion bombardment can lead to higher film density by promoting structural reordering in amorphous films and increased GPC due to enhanced surface reaction rates. This effect is particularly pronounced at low deposition temperatures, where GPC and density in PE-ALD exceed those in thermal ALD [68]. However, at high ion energies, plasma exposure may cause stoichiometric changes and crystallization [70]. A key advantage of PE-ALD is its ability to activate precursors with inherently low thermal reactivity,

thereby expanding the range of materials that can be deposited. Additionally, PE-ALD enables deposition at lower temperatures, as plasma radicals enhance precursor reactivity. However, the application of PE-ALD for coatings on highly intricate, stacked 3D structures, or high aspect ratio features is limited due to surface recombination of reactive plasma radicals. These radicals, having incomplete valence shells, tend to rapidly recombine upon collisions with 3D structure sidewalls, which significantly limits film conformality [66]. Despite its advantages, PE-ALD requires additional equipment, including a plasma source and power supplies, which increase system complexity and cost.

Precursors

Aluminum oxide (Al_2O_3) is a wide bandgap material (7 eV) frequently used in optical coatings [71]. Due to its intermediate refractive index, Al_2O_3 can function as either a low or high refractive index material, depending on the coating design. When paired with lower refractive index materials such as SiO_2, AlF_3 or MgF_2, alumina serves as a high refractive index layer. Conversely, when combined with higher refractive index materials such as HfO_2, Ta_2O_5 or TiO_2, it acts as a low refractive index material. The most common ALD precursor for Al_2O_3 is trimethylaluminum (TMA).

The deposition of Al_2O_3 via ALD using TMA and water is one of the most extensively studied ALD processes. During the first half-cycle, TMA molecules react with surface hydroxyl groups through ligand exchange reactions:

$$Al - OH^* + Al(CH_3)_3 \rightarrow Al - O - Al(CH_3)_2{}^* + CH_4$$

In the second half-cycle, water molecules react with the adsorbed precursor via hydrolysis reactions:

$$Al - O - Al(CH_3)_2{}^* + 2H_2O \rightarrow Al - O - Al(OH)_2{}^* + 2CH_4$$

In PE-ALD of Al_2O_3, the first half-cycle reaction remains the same as in the thermal ALD. However, during the second half-cycle, oxygen radicals react with the adsorbed precursor through combustion-like reactions:

$$Al - O - Al(CH_3)_2{}^* + 8O \rightarrow Al - O - Al(OH)_2{}^* + 2CO_2 + 2H_2O$$

where the asterisks denote the surface species.

During the reaction between TMA and water, methane is produced as a by-product. Since methane is an inert and volatile gas, it can be easily removed from the reactor during the purge step. Due to the high reactivity of TMA, the deposition process can be carried out even at room temperature, making ALD Al_2O_3 suitable for thermally sensitive substrates such as polymers or hybrid organic-inorganic materials. Furthermore, the small size of TMA molecules ensures efficient transport within the reactor, resulting in high uniformity of

aluminum oxide films across the large area substrates. Additionally, ALD-grown Al_2O_3 thin films remain amorphous even when deposited at temperatures as high as 600 °C [72].

Titanium oxide (TiO_2) is a high refractive index material that is transparent from the visible to the near infrared region and is widely used in optical coatings. The most common ALD precursors for TiO_2 thin films deposition are alkylamides, with tetrakis(dimethylamino)titanium (TDMAT) being among the most frequently utilized. TDMAT is highly reactive, allowing the deposition at relatively low temperatures. However, at higher deposition temperatures (> 180 °C), TDMAT can decompose, affecting film quality [73]. During the first half-cycle, TDMAT molecules react with surface hydroxyl groups through reactions:

$$TiO_2 - OH^* + Ti(N(CH_3)_2)_4 \rightarrow TiO_2 - O - Ti(N(CH_3)_2)_3{}^* + NH(CH_3)_2$$

In the second half-cycle, water molecules react with the adsorbed precursor via reactions:

$$TiO_2 - O - Ti(N(CH_3)_2)_3{}^* + 2H_2O \rightarrow TiO_2 - TiO_2 - OH^* + 3(NH(CH_3)_2)$$

where the asterisks denote the surface species.

During the reaction between TDMAT and water, dimethylamine is produced as a by-product [74].

1.2.4 Comparison of deposition techniques

Optical coatings are conventionally produced using PVD techniques, including thermal evaporation, EBE, ion-assisted deposition, magnetron sputtering, and ion beam sputtering. ALD can be employed as an alternative method for the fabrication of optical coatings, providing accurate film thickness control and conformal deposition on complex elements. However, the deposition rate of ALD (0.3 – 3 nm/min) is significantly lower than the growth rates achieved using PVD methods (0.5 – 10 nm/s). The long ALD process duration limits its efficiency for applications requiring relatively thick optical coatings, such as highly reflective coatings, filters, and coatings for the infrared spectral range. Therefore, ALD is mostly applied for AR coatings, particularly in the visible and near infrared spectral range, where the total coating thickness is typically on the order of several hundred nanometers [55]. Nevertheless, advanced ALD systems, such as spatial ALD reactors, enable a substantial reduction in deposition duration and expand the range of ALD applications in optical coatings [75,76].

The suitability of a deposition technology for a specific optical application depends not only on the deposition rate but also on the required optical properties. These requirements may vary depending on the application and

operating conditions. Key requirements include precise control of layer thickness and refractive index, low absorption, high surface quality, high LIDT, high uniformity, high density, and low stress [77,78]. A comparison of the coating properties typically achieved using different deposition technologies is provided in Table 1.

Table 1. Comparison of optical coatings deposition techniques.

Deposition technique	Density	Accuracy	Deposition rate	Stress	Uniformity	Ability to coat complex substrates
Thermal evaporation	Low	Low	1 – 10 nm/s	Tensile	Low	Limited
Electron beam evaporation	Low	Low-moderate	1 – 10 nm/s	Tensile	Moderate-high	Limited
Magnetron sputtering	Moderate-high	Moderate-high	0.5 – 1 nm/s	Compressive	Moderate-high	Limited
Ion beam sputtering	High	High	0.1 – 1 nm/s	Compressive	High	Moderate
Atomic layer deposition	High	High	0.3 – 3 nm/min	Tensile/ compressive	High	Good

The optical performance of multilayer optical coatings is highly sensitive to variations in layer thickness and refractive index. Deviations from the designed values can shift the spectrum and increase reflectance or reduce transmittance at the target wavelength. Film density is also an important property because it can influence the environmental stability of optical coatings. Porous thin films can adsorb moisture from the surrounding environment, leading to changes in their properties [8]. Coating density strongly depends on the deposition technique and process conditions. Conventional thermal evaporation and EBE produce relatively porous layers, whereas ion-assisted deposition can be employed to increase film density. Magnetron sputtering and ion beam sputtering can deposit highly dense coatings due to energetic particle bombardment [79], while ALD can also produce dense films. However, the density of ALD-grown coatings depends on the deposition parameters. For instance, increasing the deposition temperature or using PE-ALD can improve coating density [80].

The uniformity of optical coatings is a crucial parameter, particularly for large-aperture and complex shape components. Conventional PVD techniques are directional, making it challenging to form uniform and conformal coatings on large-scale, strongly curved, and free-form optics. For example, ion beam sputtering has been employed to deposit thin films on modulated substrates

while replicating the original surface topography [27,38] (Figure 9a). However, achieving uniform film thickness on highly curved lenses remains difficult due to thickness variations across the lens surface. As illustrated in Figure 9b, a thicker layer is grown on surface areas oriented perpendicular to the vapor flux compared to surface regions near the edges of the curved component, introducing thickness gradients [14]. Although complex deposition systems containing planetary substrate rotation and shadowing masks can be applied to improve coating uniformity, such modifications increase system complexity and require careful optimization procedures [81].

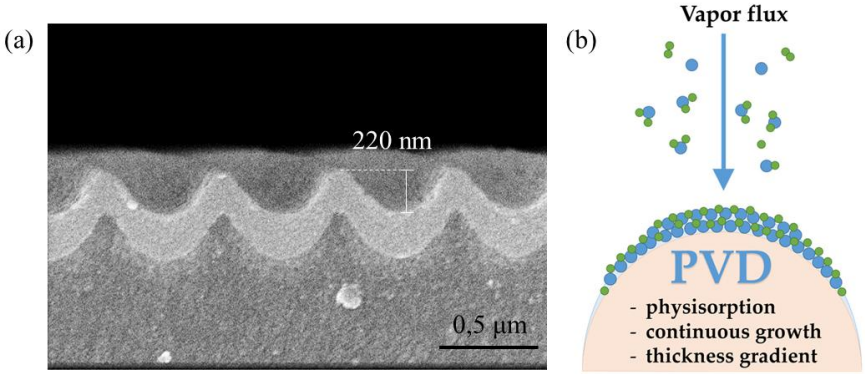


Figure 9. (a) Cross-sectional SEM image of a thin film deposited on a modulated surface using ion beam sputtering [38] and (b) schematical representation of thickness gradient during physical vapor deposition on a highly curved component [14].

The limitations of PVD become especially significant for stacked micro-optical components, in which multiple elements are connected by supporting structures for precise alignment. In such elements, all surfaces must be coated simultaneously. However, during PVD processes the top surfaces receive a greater amount of material, while underlying or shadowed areas remain uncoated (Figure 10). Consequently, PVD is generally best suited for coating planar, weakly curved, or some structured surfaces. In contrast, ALD can provide uniform and conformal coverage over complex geometries, including multi-level micro-optical components (Figure 10).

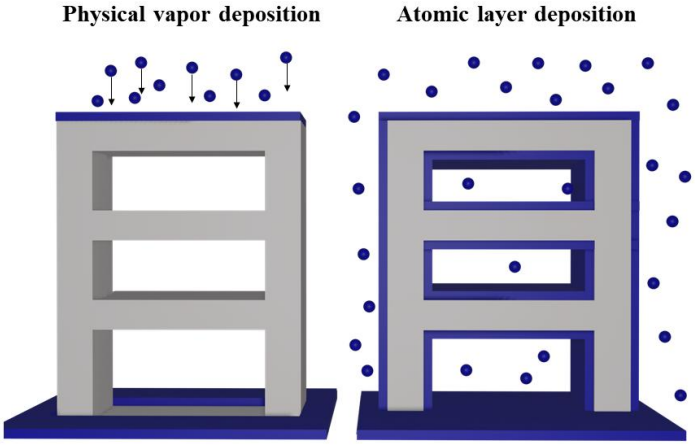


Figure 10. Schematic representation of the difference between directional physical vapor deposition and conformal atomic layer deposition on a multi-level structure.

Residual stress in thin films is another crucial property of optical coatings. Stress consists of thermal and intrinsic components. Thermal stress primarily arises from the mismatch between the coefficients of thermal expansion of the coating and substrate materials. In contrast, intrinsic stress is associated with the deposition process and film growth mechanisms and is strongly influenced by factors such as structural and chemical defects, film microstructure, and packing density. In addition, intrinsic stress depends on deposition parameters, including deposition temperature, growth rate, and ion-assisted deposition conditions, when applicable [79,82]. Furthermore, for porous films, environmental effects should also be considered, since adsorption of moisture within pores may influence film stress [78].

Residual stress in thin films can be either tensile or compressive. Coatings under tensile stress tend to contract, whereas compressive stress is associated with expansion of the film parallel to the substrate surface. Because the substrate constrains these deformations, residual stress results in bending of the substrate, leading to either concave or convex curvature. As a result, film stress can alter the flatness of the optical component, causing wavefront deformations and defocusing of the laser beam [77]. Additionally, sufficiently high stress can lead to coating failure. Tensile stress can lead to the crack initiation, whereas compressive stress can cause blistering or delamination of the coating [83,84].

During the ion beam sputtering process, the kinetic energy of sputtered atoms can be on the order of several tens of eV, resulting in high compressive stress in the thin films. Coatings produced by magnetron sputtering also

typically exhibit compressive residual stress, whereas evaporated coatings tend to exhibit tensile stress [79,82]. The stress in ALD-grown films strongly depends on deposition parameters. Typically, coatings deposited by thermal ALD exhibit high tensile stress, while PE-ALD can produce compressive stress [85,86]. Additionally, it has been reported that substrate biasing can be applied to modify the stress type and magnitude in PE-ALD coatings [87].

1.3 Quality of optical components

The quality of optical elements directly impacts the efficiency, reliability, and durability of optical systems, making their fabrication, optimization, and post-processing critical for a wide range of applications. Numerous quality parameters are used to characterize optical components, including low optical losses, high surface quality, mechanical robustness, high resistance to laser radiation, and stable optical and mechanical properties under harsh or changing operating conditions. In general, the importance of these properties depends on the final application of the component.

Structured optical components are no exception. Although these elements provide additional optical functionalities, they also exhibit imperfections that degrade their efficiency and therefore must be mitigated. In this thesis, structured optical elements operating in transmission are investigated. Consequently, low reflection losses and high transmittance are among the most important parameters. In addition, high surface quality and low surface roughness are essential for micro-optics. For porous nanostructured coatings, additional quality requirements are introduced, such as reduced moisture sensitivity, while high-power laser applications also demand low absorption and high LIDT.

1.3.1 Surface roughness

The optical performance of optical components is strongly influenced by surface quality, since high surface roughness and surface defects can increase light scattering and reduce efficiency and imaging quality. Light scattering in optical materials can be categorized into surface scattering and bulk scattering. For high-quality optical elements, surface scattering is usually the dominant source of scattering losses. Surface scattering originates from macroscopic defects, surface contamination, and microirregularities. While particulates and macroscopic defects, such as scratches and digs, primarily contribute to scattering at longer wavelengths, surface asperities with dimensions on the order of or smaller than the wavelength of light are the main source of

scattering in the ultraviolet (UV), visible, and near-infrared spectral ranges [6,78]. The height of surface irregularities is commonly described using the root mean square (RMS) roughness. In general, the required surface roughness of high-quality optical components depends on the wavelength of the light. To minimize surface scattering losses, the RMS roughness should be significantly smaller than the wavelength. Typically an acceptable roughness values range from $\lambda/5$ to $\lambda/20$ [6].

Numerous techniques have been developed to reduce surface roughness, including chemical etching, chemical mechanical polishing, and high temperature annealing. These methods can be efficient, but can also introduce subsurface damage or change the geometry and surface curvature of the component. In optical applications, maintaining precise geometry, curvature, and high surface quality is crucial, as any deformation or surface damage can significantly degrade optical performance. For example, 3D-printed polymer and hybrid-polymer microstructures often exhibit high surface roughness values ranging from several tens of nanometers to more than 100 nm [10]. Such roughness can result in considerable scattering losses. However, conventional polishing and wet etching methods can damage polymer surfaces or affect the geometry of micro-optical elements. Consequently, alternative optical finishing approaches are required for the complex micro-optical components.

Laser surface polishing can be applied as a non-contact method for reducing the surface roughness of 3D optics. It can be classified into cold laser polishing and thermal laser polishing. Cold laser polishing employs short-wavelength, ultrashort laser pulses to minimize thermal effects. This process relies on high-energy photon absorption to break molecular bonds with minimal heat accumulation. In contrast, thermal laser polishing is based on local remelting or evaporation of the substrate material caused by heat accumulation. However, laser polishing can introduce surface damage, therefore, precise sample scanning is required to prevent the formation of defects and cracks [88]. Magnetorheological polishing is another high-precision technique. This method utilizes a magnetorheological fluid composed of magnetic particles, abrasives, and a carrier liquid. With the assistance of a magnetic field, the fluid can be precisely controlled to remove surface material at the nanoscale level. Magnetorheological polishing has been applied to the surface finishing of various optical glasses and polymers. Although this technique is advancing rapidly, its relatively long processing duration limits its effectiveness for large-scale applications [89].

As an alternative, conformal coating deposition can be used to reduce the surface roughness of optical elements without modifying the geometry or

causing surface damage. Unlike the majority of surface finishing techniques that remove material, conformal film deposition is based on the layer-by-layer growth of the film, progressively filling surface grooves until the surface is smoothed [90] (Figure 11).

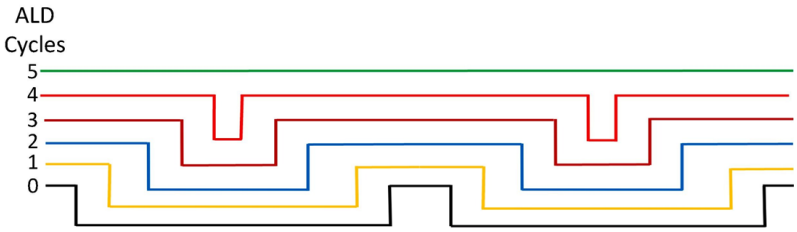


Figure 11. Schematic illustration of the progressive smoothing of a rough surface during conformal coating deposition [90].

Film conformality describes the ability of a deposited film to maintain an approximately uniform thickness over the entire surface, independent of the surface geometry. Therefore, the deposited coating follows the underlying substrate topography. However, considering a small groove on the surface, although the conformal film thickness remains constant at all points on the surface, the reduction in surface asperity height or depth is greater than the deposited film thickness (Figure 12a).

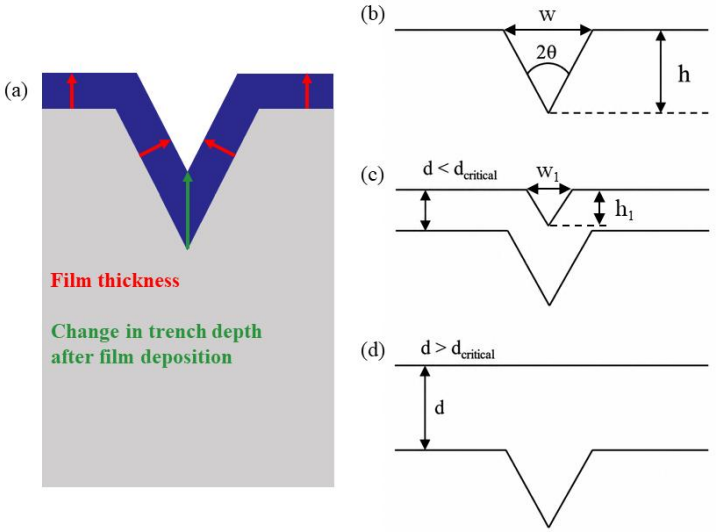


Figure 12. (a) Schematic illustration of conformal coating on a surface trench, showing a uniform coating thickness across the entire surface. The reduction in trench depth is greater than the deposited coating thickness. (b) Geometry of the initial triangular trench [91], (c) trench geometry after conformal coating deposition with a coating thickness $d < d_{critical}$ [91], and (d) trench geometry after conformal coating deposition with a coating thickness $d > d_{critical}$ [91].

According to Lau et al. [91], surface irregularities can be approximated as nanoscale triangular trenches (Figure 12b). After deposition of a conformal film with a thickness d, the surface geometry is preserved but reduced in scale (Figure 12c). The depth and width of the irregularity after conformal film deposition are given by:

$$h_1 = h - d(\csc\theta - 1)$$
$$w_1 = 2h_1 \tan\theta$$

where h_1 is the groove depth after film deposition, h is the groove depth before deposition, θ is the half-angle of the triangular groove, and w_1 is the width of the groove after deposition.

A critical film thickness can be defined as the minimum thickness required to completely fill a surface irregularity. Once the film thickness exceeds the critical thickness, a flat and smooth surface is achieved (Figure 12d). At the critical thickness w_1 = 0 and h_1 = 0, and it is expressed by:

$$d_{critical} = \frac{h}{\csc\theta - 1}$$

where $d_{critical}$ is the critical film thickness required to smooth the surface.

One of the main techniques for producing conformal coatings is ALD. Nevertheless, amorphous ALD coatings are preferred for surface smoothing because their surface roughness remains nearly constant regardless of thickness, whereas polycrystalline thin films exhibit increasing roughness as thickness grows [92]. Several studies have reported reductions in surface roughness following the deposition of amorphous films by ALD [90,93,94]. Previous works have focused on applications in microelectronics and the smoothing of polycrystalline substrates exhibiting RMS roughness values of several nanometers. Additionally, ALD Al_2O_3 has been applied for surface smoothing, thereby enhancing the reflectance of metal mirrors [90].

1.3.2 Reflection losses

When light crosses the boundary between two transparent media (e.g., air and glass), it is partially transmitted into the second medium and partially reflected at the interface (Figure 13a). The Fresnel coefficients for transmittance and reflectance at an ideal, smooth interface between homogeneous materials are described using the Fresnel equations [78]:

$$r_p = \frac{n_2 \cos\varphi - n_1 \cos\psi}{n_2 \cos\varphi + n_1 \cos\psi}$$
$$t_p = \frac{2n_1 \cos\varphi}{n_2 \cos\varphi + n_1 \cos\psi}$$

$$r_s = \frac{n_1 \cos\varphi - n_2 \cos\psi}{n_1 \cos\varphi + n_2 \cos\psi}$$

$$t_s = \frac{2n_1 \cos\varphi}{n_1 \cos\varphi + n_2 \cos\psi}$$

where φ and ψ are the angles of incidence and refraction, respectively, n_1 and n_2 are refractive indices of two media, t and r are the Fresnel coefficients, representing the ratios of transmitted and reflected electric field amplitudes, respectively. The subscripts s and p denote s- and p-polarized light. In s-polarization, the electric field oscillates perpendicular to the plane of incidence, whereas in p-polarization it oscillates parallel to the plane of incidence. At normal incidence, the reflection from the interface is given by:

$$R = \left(\frac{n_1 - n_2}{n_1 + n_2}\right)^2$$

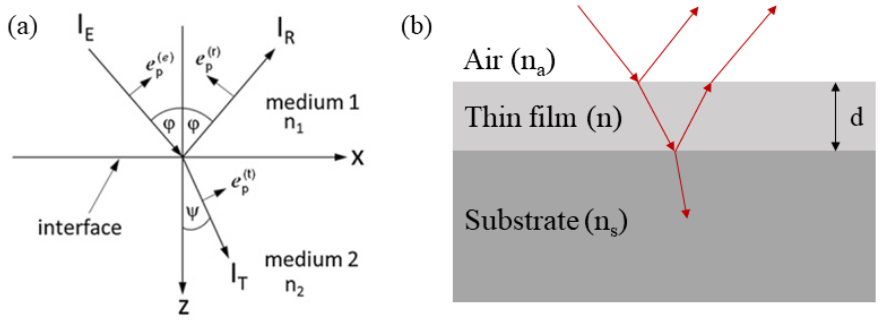


Figure 13. (a) Schematic illustration of light transmission and reflection at the interface between two media with refractive indices n_1 and n_2. The angle of incidence is denoted as φ [78]. (b) Schematic illustration of light reflection in a thin film deposited on a substrate with the refractive indices n and n_s, respectively.

Optical systems typically consist of multiple optical components, such as lenses, beam splitters, beam shapers, prisms, etc. In transmissive optical systems, accumulated reflections at multiple interfaces can significantly reduce total transmittance of the light and cause parasitic reflections or ghost images. To minimize these reflections, AR coatings are widely applied. AR coatings are dielectric thin films designed to minimize reflections through destructive interference between light waves reflected from different interfaces.

The simplest AR coating design is a single-layer coating, consisting of a quarter-wave optical thickness layer. When light is incident on a thin film, partial reflection occurs at both the air-film and film-substrate interfaces (Figure 13b). These reflected waves acquire an optical path difference given

by: $\Delta = 2ndcos\alpha$, where n is the refractive index of the film, d is the film thickness and α is the angle of refraction. The resulting phase difference between reflected waves is: $\phi = \frac{2\pi}{\lambda}\Delta$, where λ is the wavelength of light. Depending on the phase difference, constructive or destructive interference occurs. Constructive interference occurs when these two waves are in phase, while destructive interference occurs when waves are out of phase.

The optimal refractive index (n) of a single-layer AR coating at normal incidence should satisfy the relationship: $n = \sqrt{n_a n_s}$, where n_a and n_s are the refractive indices of air and the substrate, respectively [78]. MgF_2 is one of the lowest refractive index materials used for AR coatings. However, its refractive index (n = 1.38) remains too high for optimal AR performance on most optical glasses with refractive indices around 1.5, which ideally require coatings with refractive indices near 1.22 [5]. The effective refractive index of coatings can be reduced by introducing porosity. Nanoporous AR coatings are commonly produced using the sol-gel method and GLAD [30,32].

Thin films deposited by ALD are typically dense and exhibit refractive indices close to bulk materials. Although lower deposition temperature can slightly decrease film density and refractive index, the resulting reduction is insufficient to achieve the ultra-low refractive indices required for single-layer AR coatings. Recently, several approaches have been developed to produce highly porous ALD coatings, including grass-like alumina obtained through hot water-induced morphological changes of Al_2O_3 films [15,16,95] and nanoporous silica produced by selective etching of nanocomposite coatings [13,96,97]. Grass-like Al_2O_3 exhibits a gradient refractive index profile with an effective refractive index of approximately 1.2. Additionally, this gradient-index structure enables broadband and omnidirectional AR coating performance [95]. Nanoporous SiO_2 films are particularly attractive because their porosity and effective refractive index can be tailored by adjusting the composition of the initial composite coating, such as SiO_2–Al_2O_3 nanocomposite. For instance, varying the SiO_2–Al_2O_3 ratio enables tuning of the refractive index of the resulting porous SiO_2 film from approximately 1.4 to 1.13 after the selective etching procedure [97].

For high performance, broadband, and wide-angle optical applications, single-layer AR coatings can be insufficient to achieve the required optical characteristics. Instead, multilayer AR coatings consisting of alternating high and low refractive index materials are commonly employed. The simplest multilayer design is a two-layer AR coating, also referred to as a V-coating, comprising one high and one low refractive index layer. V-coatings are typically applied to minimize reflection at a single wavelength [78]. To

suppress reflections over broader spectral or angular ranges, more complex designs composed of a larger number of layers, inhomogeneous layers, or sub-wavelength surface structures are required [5]. Among these, step-down index designs, in which the refractive index decreases from the substrate toward air (Figure 14a), are widely used for broadband AR coatings [98].

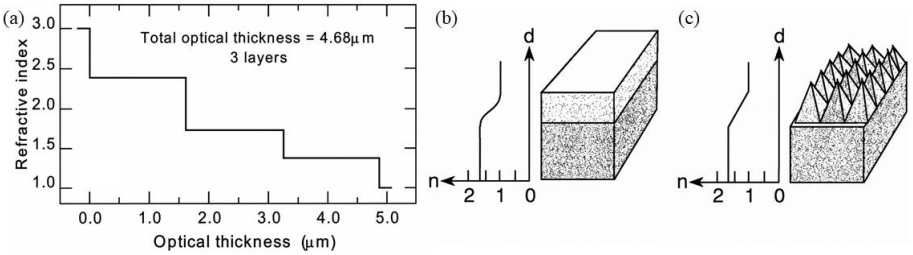


Figure 14. (a) Refractive index profile of a conventional three-layer AR coating [98], (b) effective refractive index profile and coating structure of an inhomogeneous single-layer AR coating [5], and (c) effective refractive index profile and coating structure of a structured AR coating [5].

Similar performance can be also achieved using inhomogeneous layers with continuously varying refractive indices (Figure 14b) or by structuring the surface (Figure 14c). Multilayer AR coatings are also particularly useful for multi-wavelength optical systems requiring high transmittance at several discrete wavelengths. However, achieving the desired optical performance in multilayer coatings requires precise control of both the refractive index and the thickness of each layer, as even small deviations in either parameter can considerably degrade coating performance [5,78].

1.3.3 Environmental stability

Optical components are often required to operate under demanding environmental conditions, including high temperatures, high vacuum, UV irradiation, particle radiation, and varying humidity levels. Exposure to such conditions can significantly affect the optical and physical properties of sensitive elements, thereby reducing their performance, reliability, and durability. Components particularly sensitive to environmental degradation include polymeric optics, humidity-sensitive nonlinear crystals (e.g., potassium dideuterium phosphate and beta barium borate), metallic mirrors, and porous thin films.

Highly porous thin films have received considerable interest over the past few decades because their low effective refractive index enables designs of optical coatings that are difficult to achieve using dense materials.

Particularly, porous layers can be used to produce single-layer, gradient index, broadband, wide-angle, and omnidirectional AR coatings [13,95]. In addition, nanostructured GLAD coatings can provide additional functionalities, such as optical anisotropy or the capability to produce multilayer optical interference coatings from a single material [31,33]. Moreover, relatively porous optical coatings are usually produced using conventional evaporation-based PVD techniques, such as thermal evaporation and EBE. During these processes, the kinetic energy of evaporated atoms is typically on the order of tenths of an eV. The low energy of atoms limits surface diffusion and can result in a lower density, porous microstructure [78]. Despite the inherent porosity, evaporated optical coatings are widely applied due to high deposition rates, cost-effectiveness, scalability to large substrates, and the ability to produce coatings with relatively high LIDTs [99]. In general, high-density thin films are environmentally stable. Such coatings can be deposited using ion beam sputtering, magnetron sputtering or ALD. Nevertheless, replacing lower density evaporated coatings with dense films is not always feasible or practical because of longer deposition durations, higher deposition costs, or higher residual stress. Consequently, minimizing the environmental sensitivity of porous thin films remains an important challenge.

The environmental sensitivity of porous coatings primarily originates from the adsorption of water within the porous structure. Water diffusion into the porous layer increases the effective refractive index because air within the pores can be partially or completely replaced by water, which has a significantly higher refractive index. This change in refractive index can shift the spectrum of optical coatings and consequently degrade their optical performance [100–102]. In porous anisotropic coatings, ambient humidity can additionally affect birefringence and phase retardance [44,103,104]. Moisture permeation has also been reported to influence residual stress and LIDT [8,100,105]. In addition, the adsorption of organic contaminants can also modify the optical properties of porous films [9].

The adsorption of water and other contaminants in porous coatings can result in both long-term and short-term instability. Long-term degradation, commonly referred to as aging, describes gradual changes in the optical and physical properties over periods ranging from days to months or even years after exposure to ambient conditions. In contrast, short-term instability is associated with relatively rapid and usually reversible adsorption and desorption of water caused by variations in ambient humidity or temperature [9,106,107]. In general, the rate of water diffusion within the porous structure strongly depends on pore size, coating material and its stoichiometry, and the intercolumnar spaces in nanocolumnar films. Smaller

pores typically slow water diffusion and therefore prolong the environmental stabilization process. Conversely, larger pores facilitate faster moisture permeation, resulting in more rapid stabilization but also higher sensitivity to short-term changes in ambient conditions [107].

Water adsorption in porous coatings can result in reversible and irreversible changes. Reversible changes are typically associated with physisorption, in which water molecules are weakly bound to the surfaces and can be removed through desorption. Such behavior has been reported for various oxides, including SiO_2, Nb_2O_5, TiO_2, etc. [106–108]. In contrast, irreversible changes are commonly attributed to trapped water molecules within micropores or to water chemisorption. These processes can permanently modify the optical and physical properties of porous films [106,107,109].

Furthermore, different materials can exhibit different moisture sensitivity. Since environmental stabilization of porous SiO_2 coatings is a primary focus of this work, the mechanisms of water adsorption in SiO_2 are considered in greater detail. In relaxed silica, the Si-O-Si bond angle is approximately 144°, whereas smaller bond angles correspond to strained bonds that exhibit increased chemical reactivity with water [110]. Water chemisorption occurs through the hydrolysis of strained Si-O-Si bonds according to:

$$Si - O - Si + H_2O \rightarrow 2(Si - OH)$$

This reaction results in the relaxation of the strained silica matrix and the formation of silanol (Si-OH) groups. The presence of strained SiO_2 structure has been reported in evaporated porous films [111], and their gradual relaxation has been associated with long-term changes in film stress and optical properties [109].

Ion-assisted deposition is commonly used to increase the packing density of evaporated coatings. During ion-assisted deposition, high-energy ions transfer kinetic energy to evaporated atoms, enhancing surface diffusion and reducing film porosity. As a result, short-term moisture sensitivity can be significantly reduced compared to conventionally evaporated coatings [78]. Nevertheless, degradation in optical performance, particularly in the long term, can still occur depending on the material and film microstructure [107]. Moreover, predicting humidity-induced changes in optical coatings is highly challenging because these effects depend on multiple factors such as material composition, porosity, and layer thickness [105,112]. Therefore, minimizing environmental sensitivity is highly desirable. Different approaches have been investigated to improve the environmental stability of porous optical coatings, including hydrophobic surface functionalization, deposition of protective

layers, and utilization of coating materials exhibiting lower humidity sensitivity [43,103,104,112,113].

The main characteristics of protective layers to suppress water permeation include high density, uniformity, conformality, and a low density of defects and pinholes. Furthermore, both the top surface and sidewalls of porous coatings must be encapsulated, as water can penetrate through both pathways [112]. However, PVD techniques cannot be universally applied for protecting thick coatings and non-planar optics due to the shadowing effect, which limits the uniform coverage [112,114]. ALD is a suitable technique for producing dense, conformal protective coatings on 3D substrates. ALD films are widely utilized as diffusion barriers for polymers, organic solar cells, and organic light emitting devices [115–117]. Additionally, ALD has been also utilized to produce protective layers on porous optical coatings [102,105,118]. Among the various ALD-produced encapsulation layers, Al_2O_3 is the most extensively studied due to its high density, conformality, and low density of pinhole defects. ALD-grown Al_2O_3 has demonstrated environmental protection in multiple applications. For instance, Al_2O_3 films have been employed to stabilize the refractive index and stress of porous evaporated coatings [102,105].

SiO_x thin films have been also reported for protection against moisture [119,120]. However, it has also been reported that SiO_2 films deposited using ALD often exhibit porosity, regardless of deposition temperature, resulting in spectral shifts [118]. This suggests that water can permeate through such silica coatings, making them unsuitable for encapsulation. The density of SiO_2 films can be increased using optimized PE-ALD, thereby significantly reducing spectral shifts. Additionally, bilayer structures can be employed to improve environmental stability. For example, deposition of an ALD Al_2O_3 layer on porous silica successfully encapsulated the underlying SiO_2 pores and stabilized the optical properties [118].

2 EXPERIMENTAL METHODS

2.1 Deposition of thin films

2.1.1 Atomic layer deposition

In this work, Al_2O_3 and TiO_2 thin films were deposited by ALD. Thin films were deposited using a commercial ALD system (Veeco Savannah S200). For PE-ALD, the same system was equipped with a capacitively coupled radio frequency plasma generator operating at 13.56 MHz. TMA was used as an Al-containing precursor and TDMAT was used as a Ti precursor. The TDMAT cylinder was heated to 75 °C to achieve an adequate vapor pressure, while TMA was kept at room temperature. Water or oxygen plasma were used as oxidizers, depending on the deposition process. All deposition processes were carried out under a continuous carrier gas flow. Nitrogen was used during thermal ALD, with flow rates of 20 sccm (standard cubic centimeters per minute) for Al_2O_3 and 60 sccm for TiO_2. For PE-ALD, argon was used as the carrier gas at a flow rate of 40 sccm for both materials. For plasma generation, oxygen was introduced at a flow rate of 100 sccm.

Thin films were deposited on both reference fused silica substrates and structured optical elements, such as 3D micro-optical components or porous nanostructured coatings. Because the deposition conditions were optimized for different investigations throughout this work, the specific deposition temperatures, precursor pulse durations, and purge durations are presented with the corresponding results.

2.1.2 Glancing angle deposition

Nanostructured coatings were deposited using a vacuum evaporation system (Sidrabe) equipped with step motors for GLAD method (Figure 15). In this thesis, anisotropic nanostructured SiO_2 and LaF_3 coatings were deposited and investigated. High-purity (99.9%) SiO_2 and LaF_3 granules were used as the source materials. For EBE, the source materials were placed in a copper crucible, whereas thermal evaporation employed a molybdenum boat. The evaporation boats were covered with protective covers with apertures to reduce defects. LaF_3 coatings were deposited using both thermal evaporation and EBE, while SiO_2 films were produced by EBE. The base pressure during depositions was maintained at 10^{-5} mbar. Film thickness was monitored using a QCM, and the deposition rate was maintained at 3 Å/s.

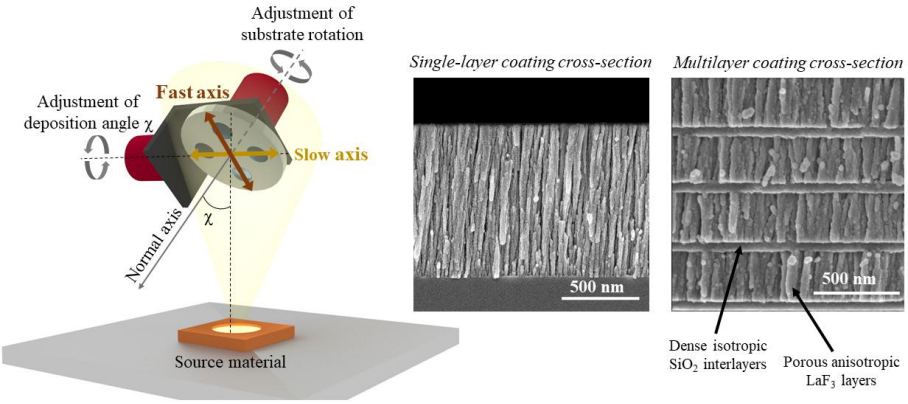


Figure 15. Schematic representation of the GLAD process and representative cross-sectional SEM images of the resulting nanostructured anisotropic single-layer LaF_3 and multilayer LaF_3+SiO_2 coatings.

Both single-layer and multilayer anisotropic coatings were investigated (Figure 15). The multilayer nanostructured coatings consisted of alternating porous anisotropic layers and dense isotropic layers. The anisotropic layers were produced using the serial bideposition technique, which involves periodic 180° rotation of the substrate around its normal. In this work, substrate rotation was performed every 6 seconds of film growth. Dense isotropic layers were deposited at a 30° deposition angle under continuous substrate rotation, as these conditions have been shown to provide higher birefringence in subsequent anisotropic layers compared to deposition at 0° angle [121].

Nanostructured coatings were deposited on 1-inch diameter, 1 mm thick fused silica substrates, which were used as reference substrates for optical characterization and retardance measurements. During LIDT measurements under UV laser irradiation, subsurface damage in fused silica can be a dominant factor in damage initiation. As a result, the LIDT of transmissive coated optics can be limited by the substrate rather than by the coating itself [122]. Therefore, for LIDT measurements, nanostructured coatings were deposited on high-quality, chemically etched 1-inch diameter, 6.35 mm thick fused silica substrates. Chemical etching removes or reduces subsurface defects and damage, resulting in substantially higher LIDT [122]. Under the same measurement conditions, chemically etched substrates used in this work exhibited LIDT of approximately 35 – 40 J cm^{-2} at 355 nm with nanosecond pulses, compared with approximately 16 – 20 J cm^{-2} for the reference fused silica substrates.

2.2 Fabrication of micro-optical components

2.2.1 Hybrid-polymer micro-optics

All hybrid-polymer micro-optical components investigated in this thesis were fabricated at the Laser Research Center, Vilnius University (Lithuania). Microstructures were fabricated from hybrid organic-inorganic polymer SZ2080™, which consists of 3-(trimethoxysilyl)propyl methacrylate and zirconium propoxide, diluted in isopropanol. 3D micro-optics were fabricated by ultrafast nanolithography done by direct laser writing (Figure 16a). Microstructures were polymerized using a laser oscillator with 517 nm wavelength, 100 fs pulse duration, and 76 MHz repetition rate. Scanning was done with a Femtika NanoFactory system, utilizing Aerotech IFOV technology known as continuous 3D writing. Fabrication power was set to ≈ 3 mW, resulting in ≈ 0.5 TW/cm^2 intensity, and scanning speed was 1 mm/s. Following the fabrication, methyl-isobutyl-ketone was used as a solvent for removal of unpolymerized resist. In this work, pure SZ2080™ photoresist was used without the photoinitiator addition, as the femtosecond laser pulses can induce photopolymerization reactions directly via multiple excitation mechanisms [123]. Two micro-lens geometries with approximate diameters of 50 μm and 100 μm were fabricated, exhibiting focal lengths in the range of 140 – 190 μm (Figure 16 b and c). In addition, flat surface microstructures with square and circular geometries and dimensions of 50 μm × 50 μm × 5 μm were fabricated (Figure 16c).

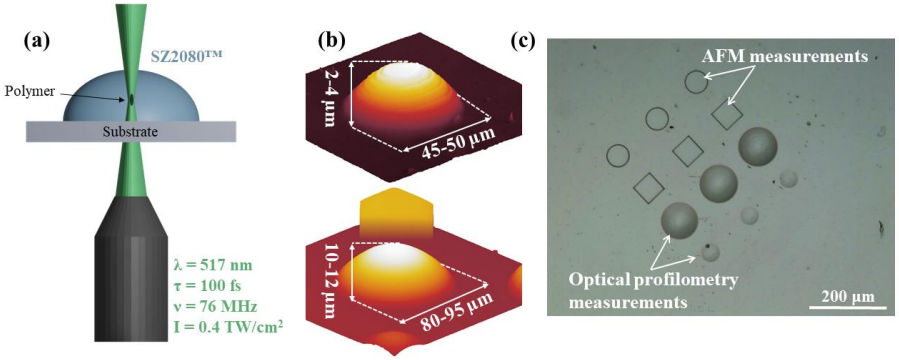


Figure 16. (a) Illustration of laser direct writing, (b) 3D profiles of the fabricated micro-lenses with diameters of ≈ 50 μm and ≈ 100 μm, (c) optical micrograph of the 3D microstructures and micro-lenses fabricated using laser direct writing.

2.2.2 Inorganic micro-optics

All inorganic micro-optical components studied in this work were fabricated at Swinburne University of Technology (Australia). 3D micro-lenses were produced by ultrashort pulsed laser back-side ablation of glasses and crystals. In this technique, the laser beam is transmitted through the transparent substrate and focused onto its back-side surface, where material removal occurs (Figure 17a). In contrast to commonly used front-side laser ablation, the removed material during back-side machining is ejected in the direction of laser beam propagation, reducing the redeposition of ablation products on the processed surface. Fabrication was performed using a femtosecond laser operating at a wavelength of 1030 nm, with a pulse duration of approximately 200 fs and a repetition rate of 200.3 kHz. Micro-optical elements were produced from fused silica, calcium fluoride, barium fluoride and sapphire. The micro-lenses had diameters of approximately 250 µm and heights of approximately 55 µm, and their typical geometry is presented in Figure 17b.

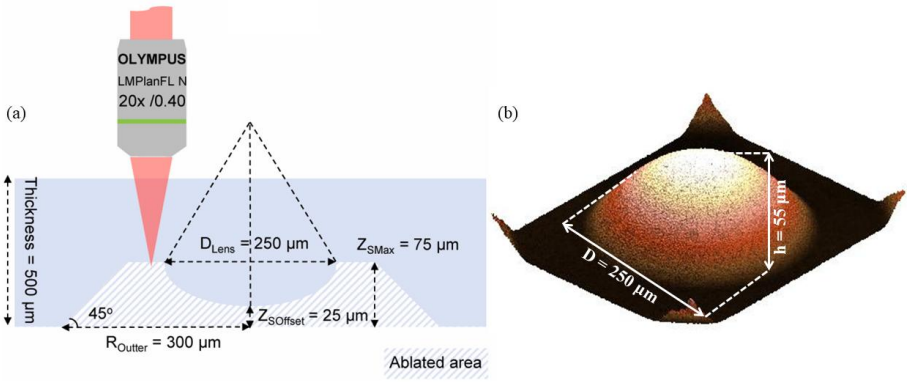


Figure 17. (a) Schematic representation of micro-lens fabrication by laser-induced back-side ablation [19] and (b) representative 3D surface profile of a fabricated fused silica micro-lens.

2.3 Characterization techniques

2.3.1 In-situ quartz crystal monitoring

The growth behavior of ALD thin films was monitored using an in-situ QCM. QCM enables real-time observation of the stepwise thickness development of the growing thin film during the ALD process by monitoring mass changes occurring on the quartz crystal surface [124]. During film

deposition, the mass deposited on the quartz crystal changes its resonant frequency according to the equation:

$$\Delta f = -\frac{2f_0^2 \Delta m}{A\sqrt{\mu\rho}}$$

where Δf is the change in resonant frequency, f_0 is the resonant frequency of the quartz crystal, Δm is the change in deposited mass, A is the active surface area of the crystal, μ is the shear modulus of quartz, and ρ is the density of quartz [125].

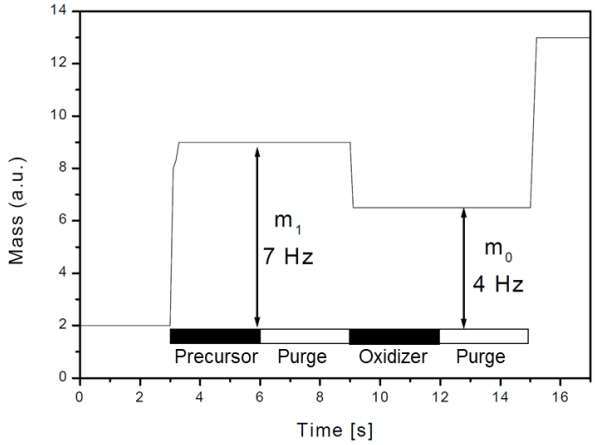


Figure 18. Schematic illustration of mass changes measured by QCM during a single ALD cycle of metal oxide film growth [125].

The GPC was determined from the measured mass increase after a certain number of ALD cycles (Figure 18). In this work, the QCM sensor was positioned at the center of the ALD reactor.

2.3.2 In-situ optical emission spectroscopy

OES is based on the detection of light emitted by plasma. Atoms, molecules, and ions introduced into the plasma are excited to higher energy states and subsequently decay to lower energy states through spontaneous emission. The emitted radiation has characteristic wavelengths determined by the energy difference between the excited and lower energy levels according to:

$$\lambda_0 = \frac{hc}{E_p - E_k}$$

where λ_0 is the central wavelength of the emitted radiation, h is the Planck constant, c is the speed of light, and $E_p - E_k$ is the energy difference between the two energy levels [126].

OES is commonly used in PE-ALD to investigate gas composition and reaction mechanisms during the plasma exposure step. Moreover, time-resolved OES can be applied to determine saturation of surface reactions and required purge durations [67]. Conventionally, light emitted by the plasma is collected using an optical fiber and coupled into a spectrometer. However, this conventional configuration provides information primarily about the plasma step and does not directly reveal precursor reactions occurring on the surface. In this thesis, a configuration with an additional plasma reactor was employed in which all gases, precursors, oxidizers, and reaction byproducts passed through the plasma region prior to spectral analysis (Figure 19). This modified OES configuration enabled monitoring of all steps of the ALD cycle.

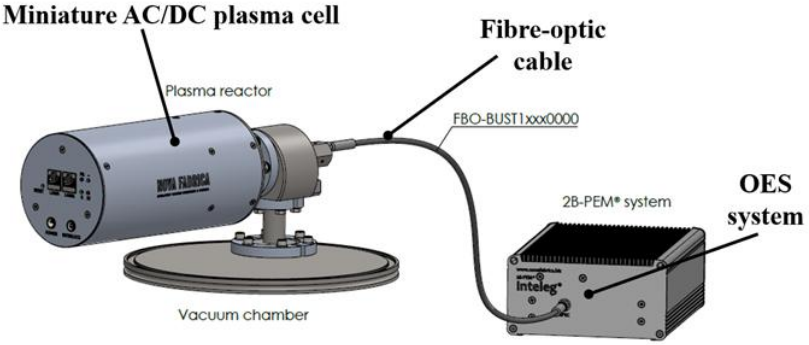


Figure 19. Self-plasma OES system (Inteleg® S IM). Image courtesy of Nova Fabrica Ltd.

2.3.3 Evaluation of optical properties

The optical properties of the thin films deposited on fused silica substrates were characterized using UV–visible spectrophotometry (Photon RT, Essent Optics spectrophotometer) in the spectral range from 185 nm to 2000 nm. For anisotropic coatings, measurements were performed along two orthogonal optical axes of the sample, referred to as the fast and slow axes. The effective refractive index along the fast axis, n_{fast} (parallel to the shadowing plane), was lower than that along the slow axis, n_{slow} (perpendicular to the shadowing plane). Birefringence was defined as the difference between effective refractive indices: $\Delta n = n_{slow} - n_{fast}$.

Film thickness, refractive index dispersion, and optical losses were determined by fitting the measured transmittance and reflectance spectra using commercial optical modeling software OptiChar (OptiLayer, Gmbh). Since the investigated materials are transparent and exhibit negligible absorption in the visible spectral range, spectral fitting was performed using a Cauchy

dispersion model combined with an exponential loss model. The refractive index was described using the Cauchy equation:

$$n(\lambda) = A_0 + \frac{A_1}{\lambda^2} + \frac{A_2}{\lambda^4}$$

where n is the refractive index, λ is the wavelength, and A_0, A_1, and A_2 are fitting coefficients.

Optical losses were determined using transmittance and reflectance spectra. It should be noted that losses evaluated by this approach include contributions from both absorption and scattering. The spectral dependence of optical losses in the UV–visible range was described using an exponential extinction model:

$$k(\lambda) = B_0 \cdot exp\left(-\frac{B_1}{\lambda} - B_2 \cdot \lambda\right)$$

where k is the extinction coefficient representing effective optical losses in the film, λ is the wavelength, and B_0, B_1, and B_2 are fitting coefficients.

During spectral fitting, these coefficients were adjusted until good agreement between calculated and measured spectra was achieved (Figure *20*), thereby determining dispersions of the refractive index and optical losses.

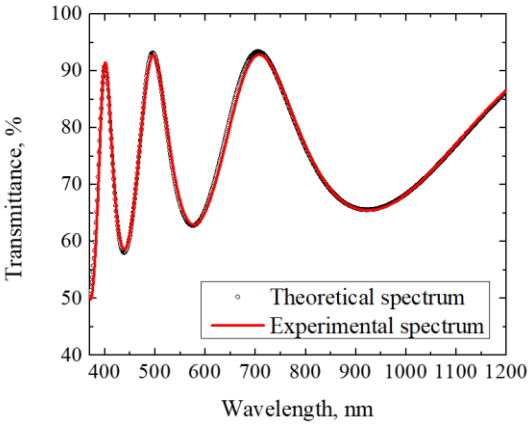


Figure 20. Comparison between the theoretical and experimental transmittance spectra of titanium oxide.

Absolute absorption of thin films was evaluated using a laser-induced deflection (LID) system developed by the Leibniz Institute of Photonic Technology [127]. The LID technique is based on a pump-probe configuration, where irradiation by the pump laser generates a thermal gradient in the surrounding medium, resulting in a refractive index gradient that deflects the probe beam proportionally to the absorbed laser power. In this work, measurements were performed at a wavelength of 355 nm using a

nanosecond pulsed laser with a beam diameter of approximately 1 mm. Absorption values are reported in parts per million (ppm).

2.3.4 Birefringence imaging

Retardance maps of the anisotropic coatings were acquired using a birefringence imaging system (Thorlabs LCC7201) operating at a wavelength of 488 nm. Retardance analysis was performed using the software supplied with the instrument. The system provides a field of view of 20 mm, a spatial resolution of 9.77 µm, and an image resolution of 2448 × 2048 pixels. Environmental stability of the anisotropic nanostructured coatings was evaluated under controlled relative humidity conditions using birefringence imaging. During these measurements, the relative humidity was reduced by introducing nitrogen gas into the sealed measurement box.

2.3.5 Laser-induced damage

Laser damage resistance of the thin films deposited on chemically etched fused silica substrates was characterized by LIDT, expressed in J cm^{-2}. LIDT measurements were performed using the 1-on-1 test procedure, in which each test site was exposed to a single laser pulse, with increasing fluence levels for each site (ISO21254:2011 [128]). In this work, the measurements were carried out using a nanosecond pulsed laser system (Ekspla NL 120). LIDT measurements were performed at two wavelengths depending on the intended application of the optical components. At 266 nm, measurements were performed using a pulse duration of 1.7 ns, and a beam diameter of 98.1 µm. At 355 nm, the laser pulse duration was 2.08 ns, the repetition rate was 15 Hz, and the beam diameter was 61 µm. For anisotropic coatings, LIDT measurements were performed along both the fast and slow optical axes by rotating the sample by 90° around the substrate normal. The incident laser light was linearly polarized, corresponding to an electric field oscillating perpendicular to the table surface. In addition, laser conditioning tests were performed using the same laser system. During these experiments, the samples were locally irradiated while gradually increasing the laser energy fluence until laser damage was detected.

2.3.6 Evaluation of residual stress

Residual stress in thin films was evaluated from substrate curvature measurements by comparing the curvature radius of fused silica substrates before and after deposition. Substrate deformation was measured using

interferometry (Zygo Verifire interferometer), and stress values were calculated using the Stoney equation [129]:

$$\sigma = \frac{1}{6}\left(\frac{1}{R_2} - \frac{1}{R_1}\right) \cdot \frac{E}{(1-\nu)} \cdot \frac{t_s^2}{t_f}$$

where σ is the thin film stress, R_1 is the curvature radius of substrate before deposition, R_2 is the curvature radius of substrate after film deposition, E is the Young's modulus of the substrate, ν is the Poisson's ratio of the substrate, t_s is the thickness of the substrate, and t_f is the film thickness.

2.3.7 Structural and surface morphology analysis

Structural properties of the structured components and thin films were characterized using SEM and atomic force microscopy (AFM). The surface morphology and internal microstructure of the nanostructured coatings were investigated using SEM (Helios NanoLab 650), acquiring both top-view and cross-sectional images. Surface quality of the investigated samples was analyzed using an AFM (Bruker Dimension Edge). AFM measurements were performed in tapping mode using diamond-like-carbon coated probes with a tip radius below 15 nm. Depending on the sample, scan areas of 10 µm × 10 µm or 20 µm × 20 µm were used. The 10 µm × 10 µm scans were acquired with 512 × 512 data points, while the 20 µm × 20 µm scans were acquired with 1024 × 1024 data points, corresponding to a spatial resolution approximately of 19.5 nm in both cases. The AFM data were analyzed using NanoScope Analysis software. Artifacts arising from sample tilt or bow were removed using first or second order polynomial flattening. The same measurement area and flattening procedure were applied to samples that were directly compared. The present work focused on the influence of ALD coatings on the surface quality of structured optical elements. The ALD films have a more pronounced effect on nanoscale roughness than on micrometer scale roughness [90]. Therefore, RMS surface roughness was used as the primary parameter for evaluating the surface quality. The RMS roughness was calculated using the following formula:

$$\sigma = \sqrt{\frac{1}{N}\sum (z_i - z)^2}$$

where z_i is the measured surface height at the i-th measurement point, z is the mean surface height, and N is the total number of measured points.

2.3.8 Characterization of the micro-optics

Inorganic micro-optics

Inorganic micro-optical elements in this thesis were characterized in terms of surface morphology and micro-lens geometry. AFM was used to characterize the surface topography and RMS roughness of the micro-lenses. AFM measurements were performed on the top of the micro-lenses, and the approximate area used for AFM measurements is indicated in Figure 21a. At least three AFM images at different positions were acquired for each element, with a scan area of 20 µm × 20 µm.

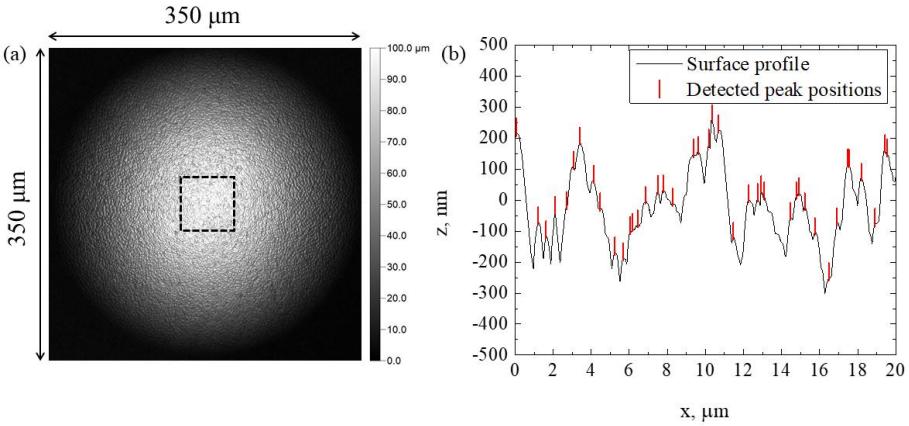


Figure 21. (a) Representative 3D profile of the inorganic micro-lens, indicating the area used for AFM measurements and (b) representative surface profile with detected peaks.

AFM data were also used to characterize the lateral dimensions of surface features. Ten profiles along the *x* direction were extracted from each AFM image. Peak analysis was subsequently performed for each profile using Origin software to identify local surface maxima. A representative surface profile with the detected peaks is shown in Figure 21b. The same peak detection and filtering parameters were applied to all measurements. Peaks with heights below 10% of the maximum height of the profile were excluded from the analysis. Peak threshold was selected to minimize the detection of false peaks. The lateral spacing between peaks was calculated as:

$$d_i = x_{i+1} - x_i$$

where x_i is the position of the *i*-th peak.

The mean lateral spacing was then calculated from all detected distances between surface peaks. Additionally, optical profilometry was used to analyze the micro-lens geometry before and after deposition of thin films by ALD. 3D profiles of micro-lenses were measured using optical profilometer (Sensofar

S Neox). The collected data were analyzed using the Gwyddion software. SEM was employed to evaluate the conformality and thickness of the deposited coating on the micro-lens surface.

Hybrid-polymer micro-optics

Hybrid-polymer micro-optical elements were analyzed in terms of geometry, surface roughness, focal length, imaging quality, and transmittance. SEM and optical profilometry were used to evaluate the geometry of the micro-optical components. AFM was used to determine the RMS roughness of the flat surface microstructures. At least three different areas were scanned for each structure, with a scan area of 10 μm × 10 μm. The focal lengths and imaging quality of the micro-lenses were evaluated using optical microscopy by imaging a square aperture and a USAF 1951 resolution target. The imaging object was placed on the microscope condenser diaphragm, providing a virtual object at a distance significantly larger than the focal length of the micro-lens. The image plane was then adjusted until a focused image was obtained. Under these conditions, the object can be considered to be located at infinity, and the image is formed in the focal plane of the micro-lens.

The relative transmittance of the micro-lenses was evaluated before and after AR coating deposition using a square aperture as the imaging object (Figure 22). An image of the aperture was captured using an optical filter with a transmission band closely matching the spectrum of AR coating. The CCD sensor operated in a grayscale mode, and a fixed region of the square image was integrated to obtain a numerical average of the grayscale intensity. No gamma correction or additional image processing was applied, assuming that the obtained image brightness is linearly proportional to the amount of light transmitted. This method provides only relative transmittance values and is suitable for comparing elements with identical shape, since the measured intensity depends not only on the transmittance but also on the geometry of the element. For comparison, transmittance measurements were also performed on flat surface microstructures.

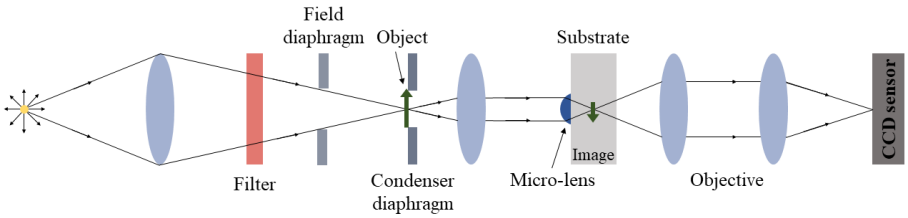


Figure 22. Schematic representation of the optical setup used for micro-lens imaging.

The transmittance of the stacked microstructures containing multiple interfaces was characterized using the tunable wavelength optical setup shown in Figure 23. A femtosecond pulsed laser (Pharos, Light Conversion) was used as the light source, with a wavelength of 1030 nm, a pulse duration of approximately 300 fs, and a repetition rate of 250 kHz. The laser beam was directed into an optical parametric amplifier (OPA; Light Conversion Orpheus) followed by a second harmonic generation (SHG) module (Light Conversion Lyra). The laser power was adjusted using neutral density (ND) filters. The laser beam was subsequently focused onto the investigated microstructure using a microscope objective with a numerical aperture of 0.25 and a magnification of 10×. The diameter of the focused beam was approximately 80 µm. The transmitted light was collected using a second objective with a numerical aperture of 0.4 and a magnification of 20×. Two photodetectors were used to measure the incident and transmitted light. A reference photodetector (PD1) positioned before the sample monitored the incident laser light, while a second photodetector (PD2) placed after the sample measured the power transmitted through the investigated microstructure. The transmittance was determined from the ratio of the transmitted and reference signals. Transmittance of the multi-level microstructures was measured in the spectral range from 400 nm to 700 nm.

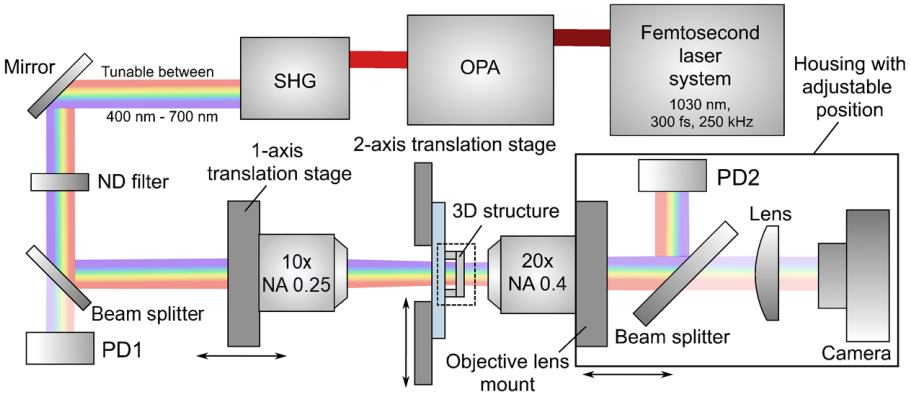


Figure 23. Schematic representation of the optical setup used for transmittance measurements of the stacked microstructures. OPA – optical parametric amplifier, SHG – second harmonic generation module, ND – neutral density filter, PD1 – reference photodetector, NA – numerical aperture, PD2 – transmitted signal photodetector.

RESULTS

The results obtained in this work are divided into two chapters, corresponding to the two main areas of research: improving the quality of micro-optical elements and enhancing the environmental stability of porous nanostructured coatings.

3 IMPROVING QUALITY OF MICRO-OPTICS

Recent progress in optical component manufacturing technologies has enabled the fabrication of highly complex and free-form micro-optical components, including micro-lenses, micro-lens arrays, stacked multi-lens elements, and other 3D microstructures. Highly rough surfaces are often observed in micro-optics fabricated by laser direct writing or laser ablation, with RMS roughness values reaching several hundreds of nanometers [10,19]. Such surface roughness can significantly degrade optical performance and imaging quality due to increased light scattering. Conventional surface finishing techniques can reduce roughness, but they can also alter the geometry of the optical elements, thereby affecting crucial parameters, such as the focal length of micro-lenses.

Moreover, many micro-optical components require AR coatings to minimize reflection losses and improve optical performance. However, intricate geometries of these elements introduce substantial challenges for coating technologies, particularly in achieving uniform coverage. Micro-optical elements with relatively simple shapes and a single exposed interface, such as micro-lenses and micro-lens arrays, can be coated using conventional PVD methods [130]. However, PVD techniques are generally not sufficient for uniformly coating multi-level micro-optical components. Alternative approaches, such as dip coating with silica nanoparticle suspensions, have been also investigated for reducing reflection losses [131]. Nevertheless, such methods typically produce only single-layer AR coatings, which limits the design flexibility for broadband or multi-wavelength optical applications.

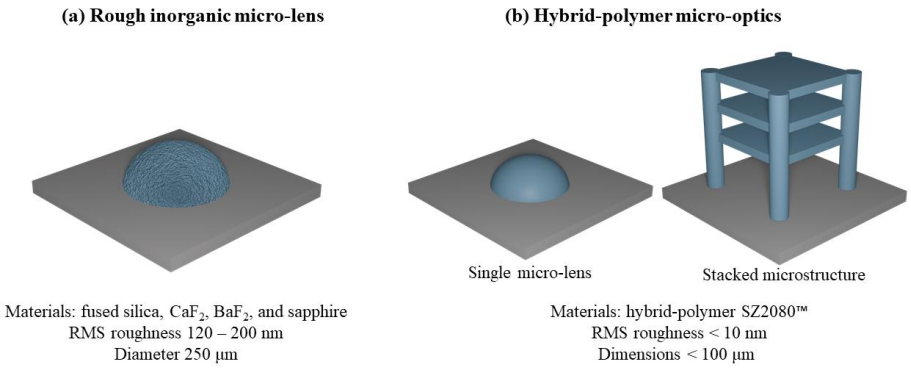


Figure 24. Schematics of the investigated micro-optical components: (a) rough inorganic micro-lens and (b) hybrid-polymer micro-lens and stacked microstructure.

In this thesis, the influence of ALD films on the surface morphology and geometry of micro-optical components is investigated. Previous studies have demonstrated that ALD-grown amorphous Al_2O_3 thin films can reduce the surface roughness of substrates with RMS roughness values of up to several tens of nanometers. The present work investigates the surface smoothing of 3D micro-lenses exhibiting a roughness on the order of 100 nm (Figure 24a). Furthermore, the deposition of conformal AR coatings using ALD on single surface and multi-level microstructures with dimensions of less than 100 µm is investigated (Figure 24b). ALD has been applied to produce conformal thin films on micro-lens arrays [20] and sub-millimeter scale multi-interface structures [7]. However, the impact of ALD coatings on the surface quality and geometry of micro-optical components has not yet been investigated.

3.1 Surface smoothing of micro-optical components

To investigate the surface smoothing capability of ALD, Al_2O_3 thin films were deposited on inorganic micro-lenses fabricated using femtosecond laser back-side ablation. For these experiments, micro-lenses with diameters of approximately 250 µm and heights of approximately 55 µm were fabricated. The micro-optical elements were made from four different materials: fused silica, CaF_2, BaF_2, and sapphire. Al_2O_3 films were deposited at 150 °C using a thermal ALD process. Each ALD cycle consisted of a TMA precursor pulse (0.02 s), a purge (6 s), a water pulse (0.02 s), and a second purge (6 s). Al_2O_3 single-layer coatings with a total thickness of 1200 nm were deposited, and the samples were characterized before deposition and after deposition of Al_2O_3 films with thicknesses of 100 nm, 200 nm, 400 nm, 800 nm, and 1200 nm. Film thickness was controlled by the number of ALD cycles. The

GPC of Al_2O_3 was approximately 1.04 Å/cycle. Consequently, deposition of each 100 nm of Al_2O_3 required 960 ALD cycles. Reference fused silica substrates were coated simultaneously with the investigated micro-optical components. The final film thickness was determined by fitting the measured transmittance and reflectance spectra (Figure 25a), confirming a film thickness of approximately 1200 nm.

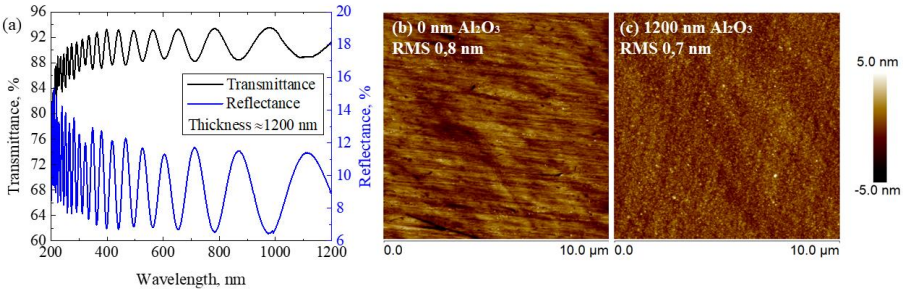


Figure 25. (a) Transmittance and reflectance spectra of ≈ 1200 nm thick Al_2O_3 film. AFM images of the reference fused silica substrate (b) before and (c) after deposition of the ≈ 1200 nm thick Al_2O_3 film.

First, the surface topography and RMS roughness of the reference fused silica substrates were evaluated using AFM before and after deposition of 1200 nm of Al_2O_3 (Figure 25 b and c). The deposited ALD film slightly reduced the roughness from 0.8 nm to 0.7 nm, indicating that the deposition process did not significantly change the surface roughness of the initially smooth substrate. Subsequently, the surface morphology of the fused silica, CaF_2, BaF_2, and sapphire micro-lenses was evaluated before and after deposition of Al_2O_3 films with different thicknesses. All AFM measurements were conducted on the top of the micro-lenses. Figure 26 shows the RMS roughness of the investigated samples as a function of the deposited Al_2O_3 thickness. All micro-lenses exhibited a reduction in surface roughness during ALD Al_2O_3 film growth. The smoothing was more pronounced during the first 200–400 nm of deposition and gradually decreased as film thickness increased.

The magnitude of the roughness reduction varied considerably among the investigated samples despite the same Al_2O_3 film thickness. Fused silica micro-lenses exhibited the highest initial roughness of 182 nm and showed a decrease by 30.8% after deposition of 1200 nm Al_2O_3. The surface roughness of CaF_2 and BaF_2 micro-lenses decreased by 39.7% and 43%, respectively, while the smallest reduction in RMS roughness (24.2%) was observed for sapphire micro-lenses after deposition of the same Al_2O_3 thickness.

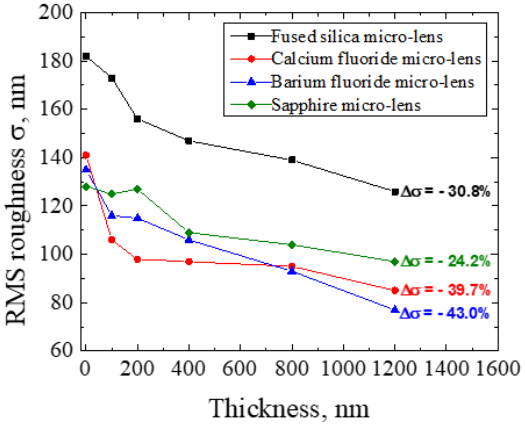


Figure 26. RMS surface roughness of fused silica, CaF_2, BaF_2, and sapphire micro-lenses as a function of ALD Al_2O_3 film thickness.

Although the initial RMS roughness values of the CaF_2, BaF_2, and sapphire micro-lenses were comparable, the achieved roughness reduction differed significantly after Al_2O_3 deposition. Previous studies have shown that ALD surface smoothing is strongly influenced by the lateral spacings of surface microirregularities, whereas RMS roughness describes only the vertical amplitude of surface topography and therefore does not fully characterize smoothing behavior [90,91]. Consequently, surfaces exhibiting similar RMS roughness may require substantially different thicknesses of ALD coating to achieve comparable smoothing if the lateral distances between surface features differ significantly. In general, larger lateral spacings between asperities require thicker ALD coatings to achieve surface smoothing.

To further investigate this behavior, the initial surface morphologies were analyzed (Figure 27). The representative surface topographies and corresponding surface profiles of the CaF_2, BaF_2, and sapphire micro-lenses differed considerably despite their comparable RMS roughness values. Furthermore, the average lateral spacings of surface features were evaluated from the surface profiles for all micro-lenses before deposition of Al_2O_3. The methodology used to characterize the lateral distances between surface peaks is described in Section 2.3.8. Among the investigated samples, the fused silica micro-lenses exhibited an average lateral spacing of approximately 400 nm before coating and showed an intermediate reduction in RMS roughness (30.8%) after deposition of 1200 nm thick ALD Al_2O_3. CaF_2 and BaF_2 micro-lenses exhibited finer surface features with average lateral spacings of approximately 270 nm and 260 nm, respectively, whereas sapphire micro-lenses contained larger asperities separated by average distances of

approximately 470 nm. Consistent with these differences in surface morphology, deposition of the same Al_2O_3 film thickness resulted in a smaller reduction in RMS roughness for sapphire micro-lenses (24.2%) than for CaF_2 and BaF_2 micro-lenses (RMS reduction by 39.7% for CaF_2 and 43% for BaF_2).

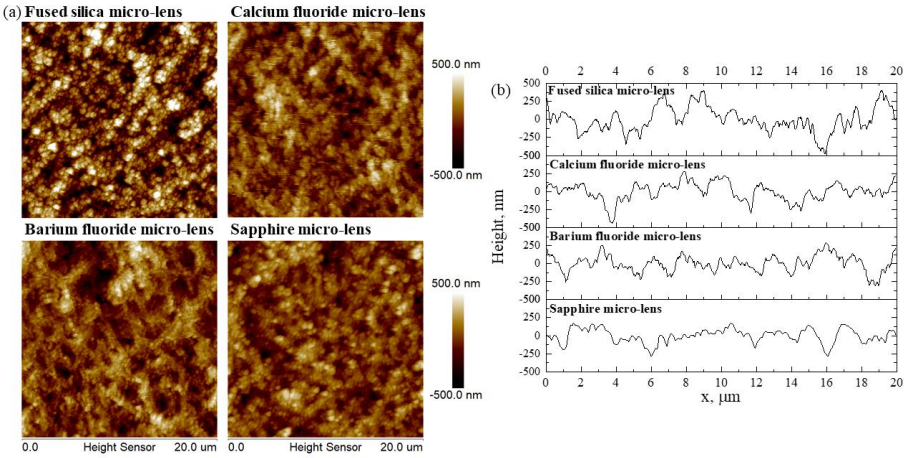


Figure 27. Initial surface morphology of fused silica, CaF_2, BaF_2, and sapphire micro-lenses: (a) AFM images and (b) representative surface profiles obtained from AFM measurements.

Subsequently, the evolution of surface morphology during ALD was analyzed. During film growth, surface irregularities broadened in the lateral direction while simultaneously decreasing in height, leading to an overall reduction in roughness (Figure 28). In addition, sharp surface features became increasingly rounded with increasing Al_2O_3 thickness. Surface irregularities with smaller lateral dimensions exhibited faster smoothing, whereas larger-scale surface features required thicker coatings to achieve significant surface flattening. However, increasing film thickness also increased the lateral spacing between neighboring asperities, leading to a reduction in smoothing rate because thicker coatings were required for further roughness reduction. Similar trends were observed for all investigated samples. These observations are consistent with previous studies showing that surface smoothing via ALD becomes increasingly limited as the lateral spacing between surface features increases [90].

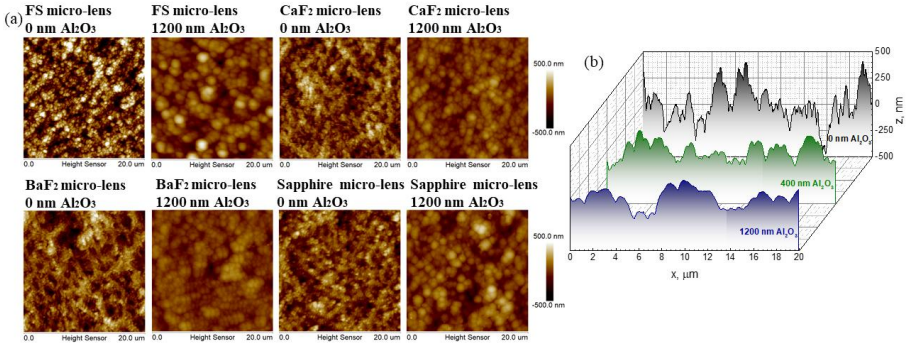


Figure 28. (a) Surface morphology of fused silica, CaF_2, BaF_2, and sapphire micro-lenses before and after deposition of 1200 nm Al_2O_3, and (b) representative surface profiles of the fused silica micro-lens before and after Al_2O_3 deposition of 400 nm and 1200 nm. Surface profiles were obtained from AFM measurements.

In addition, cross-sectional SEM imaging was performed to evaluate the conformality of the deposited ALD coating on the 3D micro-lenses. After deposition of an approximately 1200 nm thick Al_2O_3 film, a coated CaF_2 micro-lens was cleaved and cross-sectional SEM images were acquired (Figure 29). The SEM analysis confirmed that the Al_2O_3 film exhibited uniform thickness over the entire curved surface of the micro-lens. The determined film thickness was approximately 1200 nm, which is in good agreement with the thickness deposited on planar reference fused silica substrates.

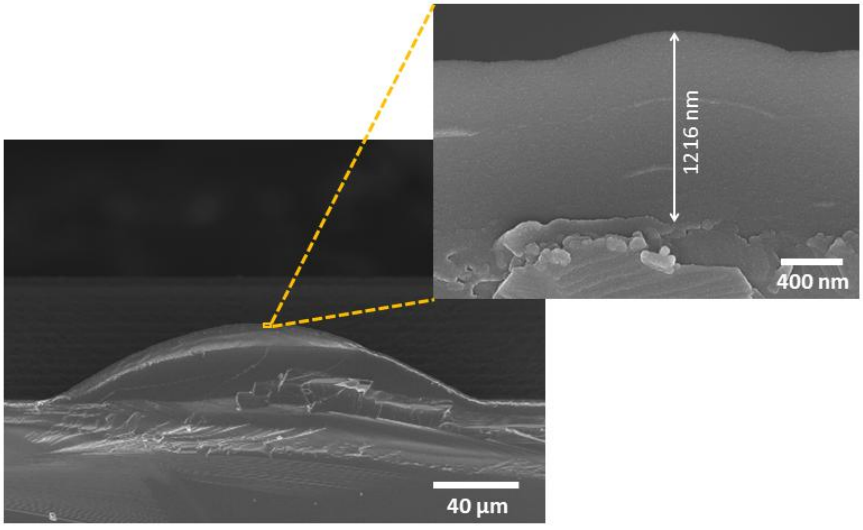


Figure 29. Cross-sectional SEM image of the cleaved CaF_2 micro-lens, showing both a lower magnification view and a magnified region used for determination of the Al_2O_3 film thickness.

Finally, the influence of the Al_2O_3 film on the geometry of the micro-lenses was evaluated. The geometry of micro-optical components is a critical parameter determining their optical performance. For example, changes in micro-lens geometry directly affect the focal length. Since ALD films can exhibit relatively high intrinsic stress, deposition of such films on the micro-optical components can induce deformations and alter the shape of the element. Also, crack formation in ALD films deposited on 3D micro-optics was observed which is also attributed to high stress [7]. To evaluate these effects, the profiles of the micro-lenses were measured using optical profilometry before and after deposition. No measurable changes in the shape, diameter, or height of the micro-lenses were observed after deposition of the 1200 nm thick Al_2O_3 film (Figure 30).

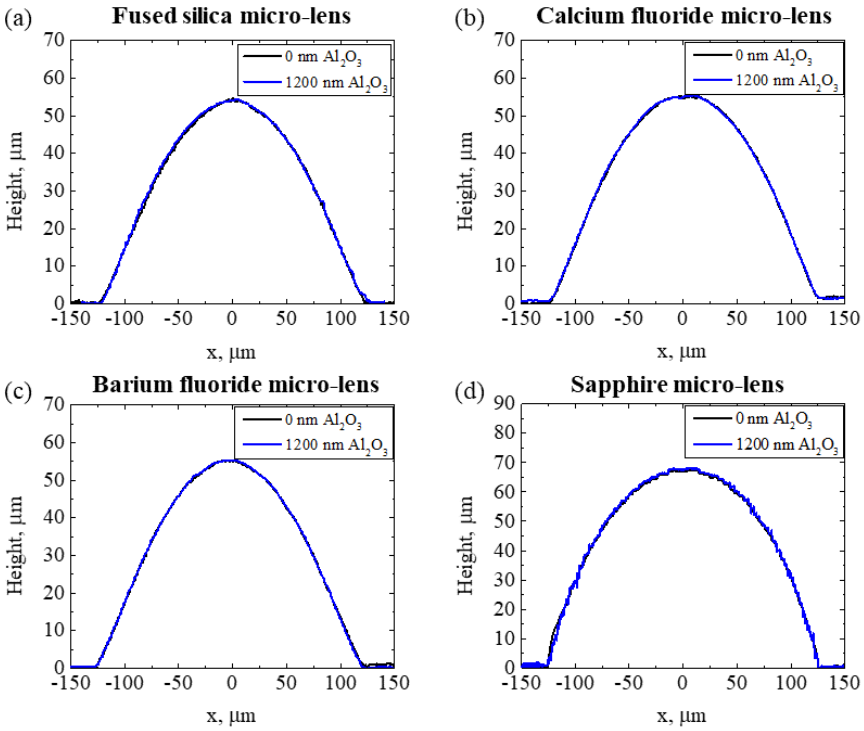


Figure 30. Profiles before and after deposition of a 1200 nm thick Al_2O_3 film for micro-lenses fabricated from (a) fused silica, (b) calcium fluoride, (c) barium fluoride, and (d) sapphire.

To compare the surface smoothing behavior on randomly rough surfaces and periodically modulated surfaces, Al_2O_3 films were also deposited on hybrid-polymer and fused silica gratings in the same ALD process. The initial modulation depths of hybrid-polymer and fused silica gratings were 194 nm

and 199 nm, respectively. Surface topography and modulation depths were characterized by AFM before and after deposition of 200 nm, 400 nm, 800 nm, and 1200 nm thick Al_2O_3 layers. With increasing Al_2O_3 thickness, the modulation depths of both gratings decreased to approximately 32 nm, corresponding to a reduction of approximately 84% (Figure 31). These results are in agreement with previously observed flattening of modulated substrates after deposition of ALD coatings with thicknesses exceeding 1 μm [38,132].

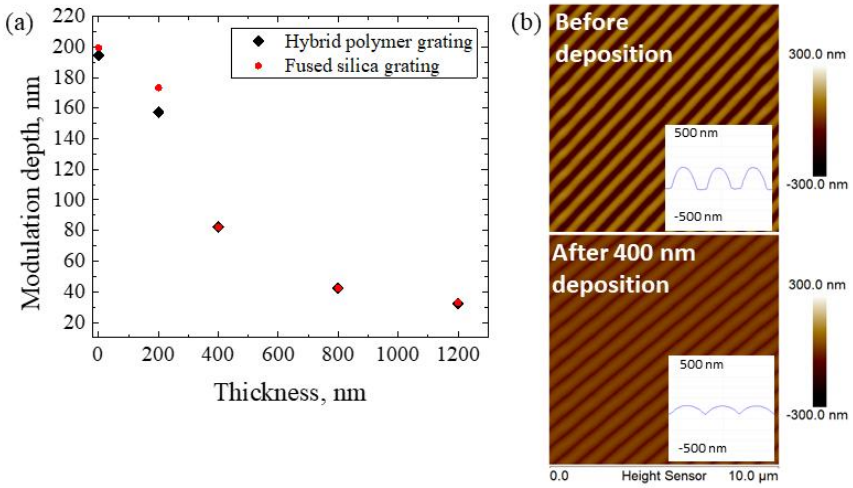


Figure 31. (a) Modulation depth of fused silica and hybrid-polymer gratings as a function of ALD Al_2O_3 film thickness, and (b) surface morphology of the hybrid-polymer grating before and after deposition of 400 nm Al_2O_3.

Although ALD exhibits a relatively low smoothing rate and requires thick coatings to effectively reduce surface roughness, it remains a valuable approach for optical applications, such as coating the complex 3D optical components. Additionally, ALD can be employed to produce amorphous AR coatings, which may simultaneously reduce light scattering and unwanted reflection losses.

3.2 Reduction of reflection losses in micro-optical components

3.2.1 Optical properties of hybrid-polymer SZ2080™

To model the design of the AR coating, the refractive index and optical losses of the substrate must be known. The hybrid organic-inorganic polymer SZ2080™ is not a standard optical substrate, and its optical characteristics depend on fabrication parameters [10]. Therefore, it is necessary to determine the dispersion of the refractive index and optical losses of SZ2080™. For this

purpose, a thin film of SZ2080™ with a thickness of a few micrometers was spin-coated onto a fused silica substrate, and its transmittance spectrum was measured (Figure 32a). Using this spectrum, the refractive index and optical losses were calculated (Figure 32b).

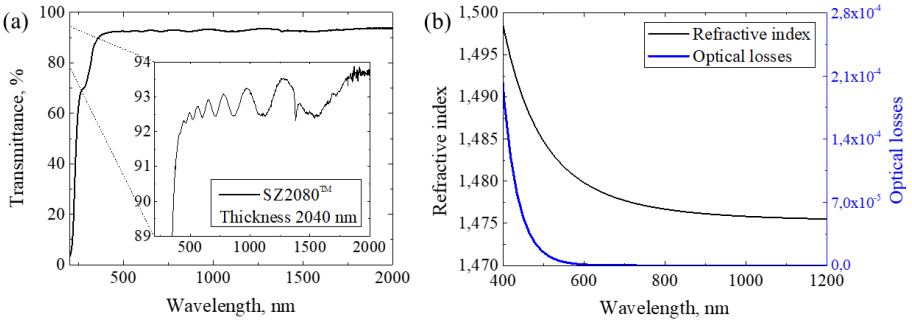


Figure 32. (a) Transmittance spectrum of spin-coated and thermally polymerized ≈ 2 μm thick SZ2080™ layer; (b) dispersions of refractive index and optical losses of spin-coated and thermally polymerized SZ2080™ layer.

At a wavelength of 633 nm, the refractive index of the spin-coated SZ2080™ film was found to be 1.48, which is slightly lower than the value of 1.5 – 1.6 reported in the literature [18,23]. This discrepancy could be attributed to the differences in the polymerization technique. Typically, SZ2080™ films are produced using UV curing with the addition of a photoinitiator, enabling a higher degree of cross-linking [23]. In this work, the use of a photoinitiator was intentionally avoided to eliminate potential time-dependent variability of polymer properties [133]. Instead, thermal curing was employed, which may result in a lower degree of cross-linking [134]. This, in turn, can explain the observed decrease in the refractive index.

Since chemical reactions during a conventional ALD process are driven by thermal energy, deposition is typically carried out at elevated temperatures. However, polymeric materials are often prone to thermal degradation. Therefore, it is crucial to evaluate the thermal stability of SZ2080™. Thus, thermal annealing of spin-coated SZ2080™ films was performed, and their optical properties were subsequently characterized. Annealing at 200°C resulted in a slight reduction in film thickness and an increase in the effective refractive index (Figure 33 a, b). At 300 °C, a significantly more pronounced decrease in thickness (exceeding 50%) was observed, along with a considerable increase in refractive index, indicating substantial changes in film structure and densification.

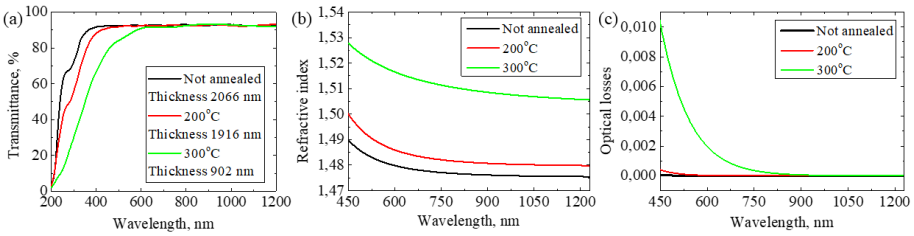


Figure 33. Optical properties of SZ2080™ films before and after thermal annealing at 200 °C and 300 °C: (a) transmittance spectra, (b) dispersions of refractive indices, and (c) optical losses.

However, annealing also led to increased optical losses, especially after treatment at 300 °C (Figure 33c). Moreover, visible changes in film color were observed after annealing. A slight yellowing of the film occurred after annealing at 200 °C, whereas annealing at 300 °C led to more pronounced darkening. These observations, together with the increased optical losses, indicate thermal degradation, likely associated with decomposition of the organic components in SZ2080™.

3.2.2 Optimization of TiO_2 thin film deposition

To enable the deposition of high-quality AR coatings on temperature-sensitive hybrid polymer micro-optics, the ALD process parameters must be optimized under low temperature deposition conditions. However, reduced deposition temperature often leads to decreased film density and insufficient oxidation. To improve film quality and achieve higher density at lower deposition temperatures, PE-ALD or multi-pulse ALD cycles could be applied [135,136]. In particular, optimization of the multi-pulse ALD process requires systematic establishment of precursor pulse durations, pulse numbers, and purge durations. This procedure is time-consuming when relying only on ex situ characterization, thereby promoting the use of in situ measurement techniques. In this context, time-resolved OES can be employed to analyze gas-phase species during the ALD process.

For the analysis of TiO_2 film growth, two characteristic spectral lines were selected: C≡N* at a wavelength of 385.3 nm and OH* at 308 nm. The CN* emission is attributed to dissociation of TDMAT precursor molecules and reaction products, while the OH* emission is associated with oxidizing species introduced during the process. Figure 34 presents the temporal evolution of CN* and OH* emission intensities during a representative multi-pulse ALD sequence consisting of 10 TDMAT pulses followed by 7 H_2O pulses. Analysis of the signal decay after each precursor exposure enables

estimation of the required purge durations. The CN* signal intensity returns to baseline within approximately 10 s following the TDMAT pulse, whereas the OH* signal requires approximately 12 s after the water pulse. Here, the baseline is defined as the emission intensity prior to precursor or oxidizer introduction into the reactor.

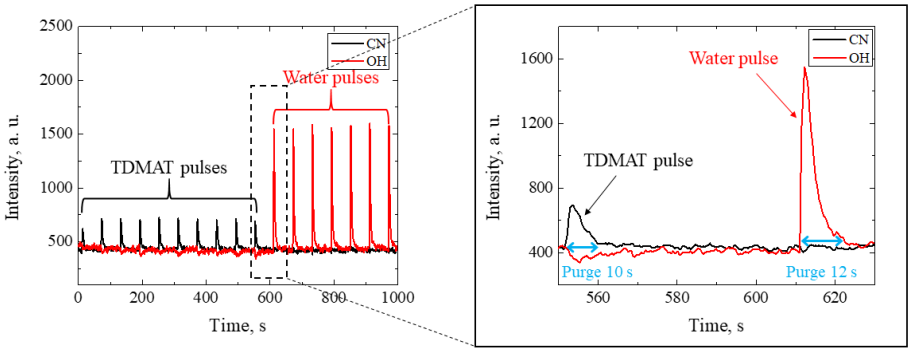


Figure 34. Changes in CN and OH emission during the multi-pulse ALD cycle measured using time-resolved OES.

To optimize the precursor dosing sequence, a series of multi-pulse ALD processes were carried out, where the TDMAT pulse duration was varied between 0.02 s and 0.1 s, while maintaining constant H_2O pulse durations and purge durations. The maximum CN* signal intensity was registered following each TDMAT pulse (Figure 35). At a pulse duration of 0.02 s, the CN* intensity observed after the first TDMAT pulse is lower than after subsequent pulses. This behavior suggests that initial precursor exposure is insufficient for reaction saturation, and that the detected emission primarily originates from reaction products rather than dissociation of unreacted precursor molecules. From the second pulse onward, the CN* intensity reaches a nearly constant level, indicating a steady state condition in which a similar amount of residual precursor and reaction products contributes to the observed CN* emission after each TDMAT pulse.

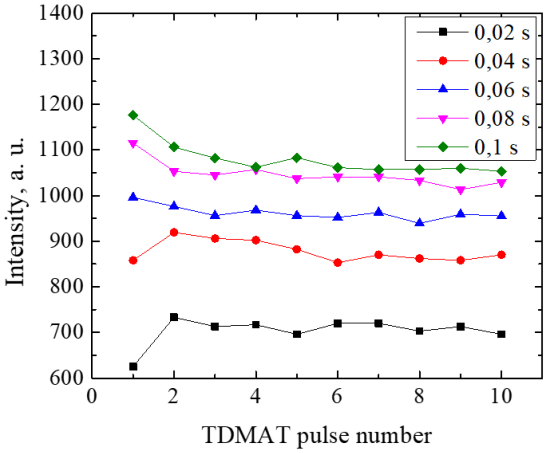


Figure 35. Maximum CN emission intensity after each TDMAT pulse during multi-pulse ALD cycles with varying TDMAT pulse durations measured using time-resolved OES.

Increasing the TDMAT pulse duration to 0.04 s revealed a similar tendency, with a lower CN* signal observed after the first pulse. However, from the second pulse, an increase in emission intensity was observed, suggesting that both unreacted precursor molecules and reaction by products contribute to the CN* signal. The CN* emission intensity decreased from the second to the fifth pulse, which may be related to a decreasing amount of reaction products. From the sixth TDMAT pulse, the CN* signal intensity stabilized, indicating saturation of surface reactions, where additional precursor doses no longer enhanced the surface reactions. Conversely, at longer pulse durations ($\geq$ 0.06 s), increased CN* intensity is observed during the first TDMAT pulses, suggesting that a significant fraction of the precursor remains unreacted and contributes to higher CN* emission. Such tendency suggests precursor overdosing and inefficient utilization. Based on these findings, a TDMAT pulse duration of 0.04 s was selected for further investigation.

Later, to determine the optimal technological deposition parameters for producing high-quality TiO_2 films at low deposition temperature (60 °C), four different approximately 150 nm thick TiO_2 single-layer coatings were deposited on the reference fused silica substrates using: (i) a standard thermal ALD cycle, in which the precursor and water were alternately delivered into the reactor following a conventional ALD cycle; (ii) a short multi-pulse thermal ALD cycle, where multiple precursor and water pulses were introduced into the reactor, separated by short purge durations; (iii) a long multi-pulse thermal ALD cycle, where multiple precursor and water pulses

were delivered into the reactor, separated by extended purge durations; (iv) a PE-ALD cycle, in which oxygen plasma was used as the oxidizer. The summarized deposition parameters are presented in Table 2.

Table 2. Parameters used for the optimization of TiO_2 thin films deposition.

ALD cycle	Oxidizer	Number of TDMAT pulses × pulse duration, s	Purge duration, s	Number of oxidizer pulses × pulse duration, s	Purge duration, s
Standard thermal	H_2O	1 × 0.15	15	1 × 0.02	15
Short multi-pulse	H_2O	10 × 0.04	2, last purge 15	5 × 0.02	2, last purge 15
Long multi-pulse	H_2O	6 × 0.04	15	5 × 0.02	15
Plasma	O_2 plasma	1 × 0.15	15	1 × 6	15

The refractive index and optical losses of the TiO_2 films were evaluated (Figure 36 a, b). The film deposited using the standard thermal ALD cycle exhibited the lowest refractive index. The short multi-pulse ALD mode enabled the deposition of a denser layer with a higher refractive index, which can be attributed to more complete surface reactions and improved surface saturation. The long multi-pulse sequence further increased the refractive index. This may be attributed to more efficient removal of reaction products during extended purge steps, which can lead to reduced blocking of reactive sites and more complete ALD reactions. The highest refractive index was achieved using PE-ALD. Plasma assistance enhances surface reactions and promotes more complete oxidation, enabling the formation of denser films even at low deposition temperatures [135].

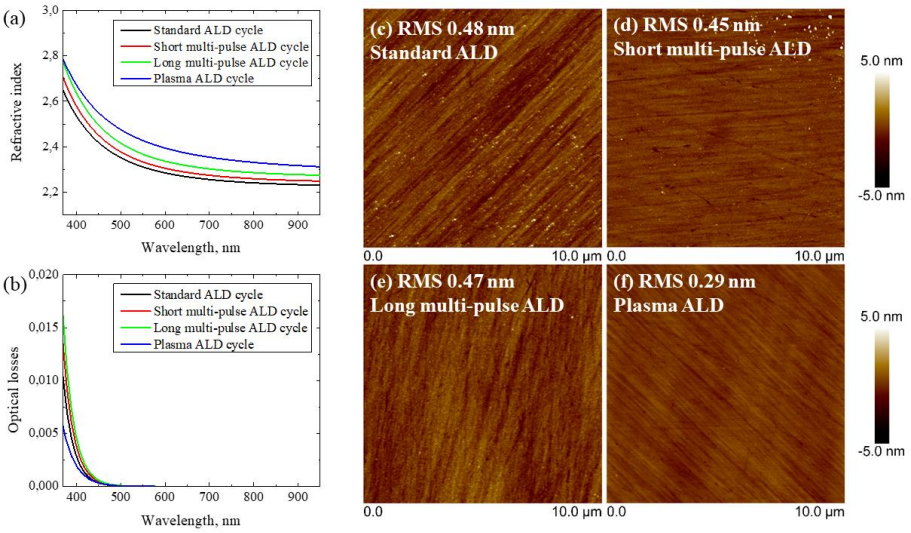


Figure 36. Dispersions of TiO_2 (a) refractive indices and (b) optical losses. Surface morphologies of TiO_2 films produced using (c) standard ALD cycle, (d) short multi-pulse ALD cycle, (e) long multi-pulse ALD cycle, (f) PE-ALD.

All thermally grown TiO_2 films, including the standard and both multi-pulse ALD processes, exhibited higher optical losses in the UV–visible spectral range compared to the films produced by PE-ALD. Consequently, the surface morphology and RMS roughness of the films were additionally analyzed using AFM (Figure 36 c–f). TiO_2 films deposited using water as the oxidizer exhibited higher surface roughness, with RMS values of approximately 0.5 nm. Higher surface roughness of these films could contribute to the observed higher optical losses. In contrast, the film produced by PE-ALD showed the lowest RMS roughness of 0.3 nm. According to these results, the PE-ALD process was selected for TiO_2 layer deposition in subsequent AR coating formation.

3.2.3 Al_2O_3 film growth on SZ2080™

The growth dynamics of ALD thin films strongly depend on the substrate, with the most pronounced differences occurring during the initial stages of film growth. The nucleation period plays a crucial role in the formation of continuous thin films required for optical coatings applications. While the growth dynamics of Al_2O_3 on various polymers have been extensively studied [137–140], no studies have been reported to date for hybrid organic-inorganic polymers such as SZ2080™.

One approach to investigate film growth dynamics and nucleation is based on a QCM, where the substrate material is deposited onto the quartz crystal

sensor, and mass changes during the ALD process are monitored. In this work, the growth dynamics of Al_2O_3 on drop-casted hybrid polymer SZ2080™ were analyzed using in situ QCM. Figure 37a shows the evolution of Al_2O_3 growth on SZ2080™. For comparison, growth on a bare Au-coated quartz crystal is also presented. During the first ≈ 50 cycles of Al_2O_3 growth on the Au-coated quartz crystal, the growth rate is initially low, indicating a nucleation delay associated with a limited number of reactive surface sites. This behavior is consistent with an island-like growth mode [141].

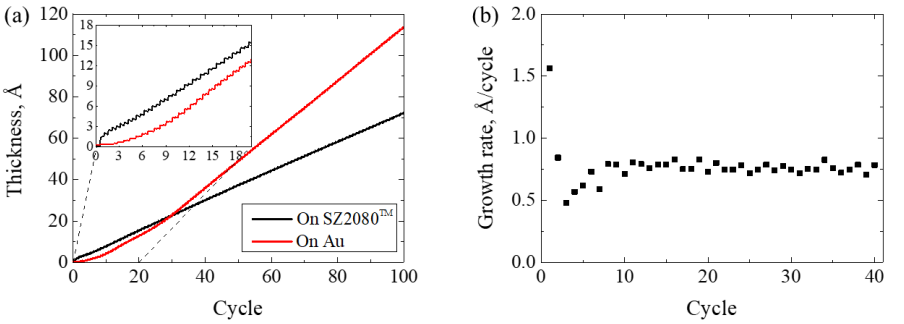


Figure 37. (a) Al_2O_3 film thickness as a function of the number of ALD cycles measured via QCM. The inset shows data collected in the first 20 cycles; (b) the growth per cycle of the Al_2O_3 as a function of the number of cycles determined from data collected through QCM.

In contrast, Al_2O_3 growth on SZ2080™ exhibits a different nucleation behavior (Figure 37b). During the first two cycles, a relatively high GPC is observed, followed by a rapid decrease and a subsequent gradual increase until a linear growth regime is reached. This behavior can be attributed to the initial interaction of the TMA precursor with the polymer surface. Since TMA molecules are relatively small, they can penetrate into the near surface region of porous polymeric materials [137,138]. Thus, adsorption of TMA into the hybrid polymer bulk may explain the higher GPC observed during the first two ALD cycles. The lower growth rate between the third and eighth ALD cycles can be associated with formation of Al_2O_3 clusters, as described in the Wilson et al. model for Al_2O_3 ALD nucleation and growth on polymers [137]. After approximately eight cycles, a linear ALD growth is observed, which is likely related to coalescence of Al_2O_3 clusters and formation of a continuous Al_2O_3 film.

3.2.4 Single-layer coatings on micro-optics

For the formation of AR coatings on hybrid-polymer micro-optics, TiO_2 and Al_2O_3 were selected as high and low refractive index materials,

respectively. Based on previous experiments, a low temperature (60 °C) PE-ALD process was chosen to obtain high-quality TiO_2 films without introducing thermal damage to the microstructures fabricated from hybrid-polymer SZ2080™. The deposition parameters of the investigated Al_2O_3 and TiO_2 single-layer coatings are summarized in Table 3.

Table 3. Optimized ALD process parameters for deposition of TiO_2 and Al_2O_3.

Material	Precursor pulse duration, s	Purge duration, s	O_2 plasma exposure duration, s	Purge duration, s	Plasma power, W
TiO_2	0.15	15	6	15	200
Al_2O_3	0.02	8	6	8	100

First, TiO_2 and Al_2O_3 were deposited as single-layer coatings on reference fused silica substrates to characterize their optical and physical properties. The transmittance spectra of Al_2O_3 and TiO_2 thin films with thicknesses of approximately 300 nm are shown in Figure 38a, while the dispersions of refractive indices and optical losses are presented in Figure 38b. The refractive indices of TiO_2 and Al_2O_3 at a wavelength of 633 nm were 2.38 and 1.61, respectively. These values are consistent with previously reported results obtained using the same precursors and similar deposition conditions [142]. The determined optical properties of TiO_2 and Al_2O_3 were subsequently used for AR coating design.

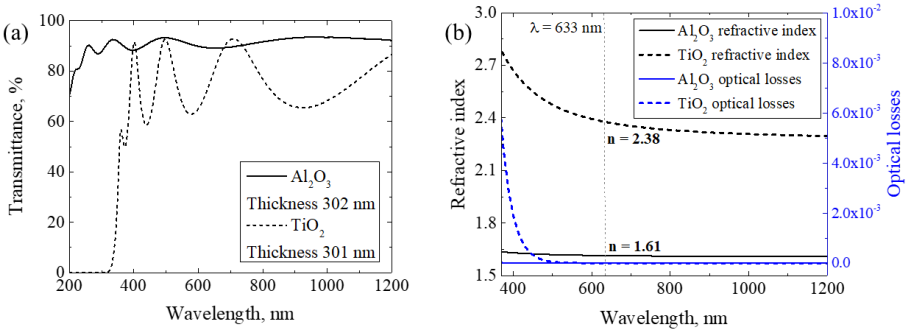


Figure 38. Optical properties of Al_2O_3 and TiO_2 single-layer coatings: (a) transmittance spectra and (b) dispersions of refractive index and optical losses.

The same ≈ 300 nm thick TiO_2 and Al_2O_3 single-layer coatings were also deposited on flat surface microstructures and micro-lenses fabricated via laser direct writing from hybrid-polymer SZ2080™ (Figure 39). Different micro-

optic geometries were employed to enable appropriate characterization of specific properties. For example, the micro-lenses used in this work were not suitable for AFM surface morphology analysis because of the stair-stepping effect (Figure 39b). Therefore, flat surface microstructures were primarily used to evaluate the surface roughness, whereas the micro-lenses were characterized in terms of their geometry and focal length.

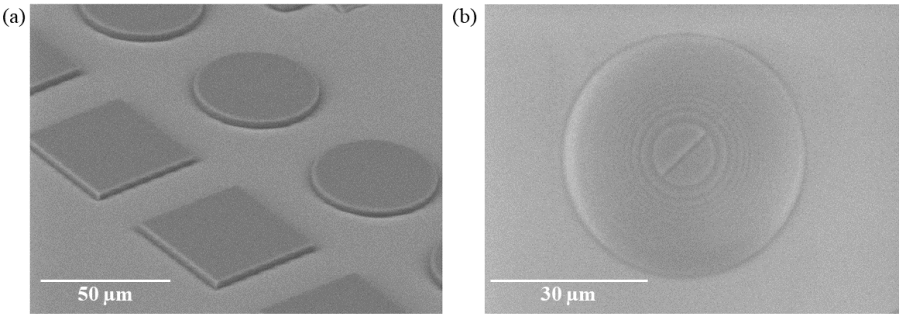


Figure 39. SEM images of micro-optical components: (a) flat surface microstructures and (b) micro-lens.

First, the influence of single-layer coatings on the geometry of the micro-optical elements was investigated using optical profilometry before and after film deposition. For these experiments, microstructures with different shapes and sizes were analyzed to reduce potential measurement errors and artifacts and to ensure that the observed changes in the profiles were induced by the deposited coating. Profiles of circular flat surface microstructures and micro-lenses with diameters of ≈ 50 µm and ≈ 80 µm before and after deposition of TiO_2 and Al_2O_3 thin films are presented in Figure 40 (TiO_2 – a and b, Al_2O_3 – c and d). The two coating materials affected the geometry of the micro-optical elements differently. Deposition of TiO_2 reduced the height of the microstructures, whereas deposition of Al_2O_3 led to an increase in their height.

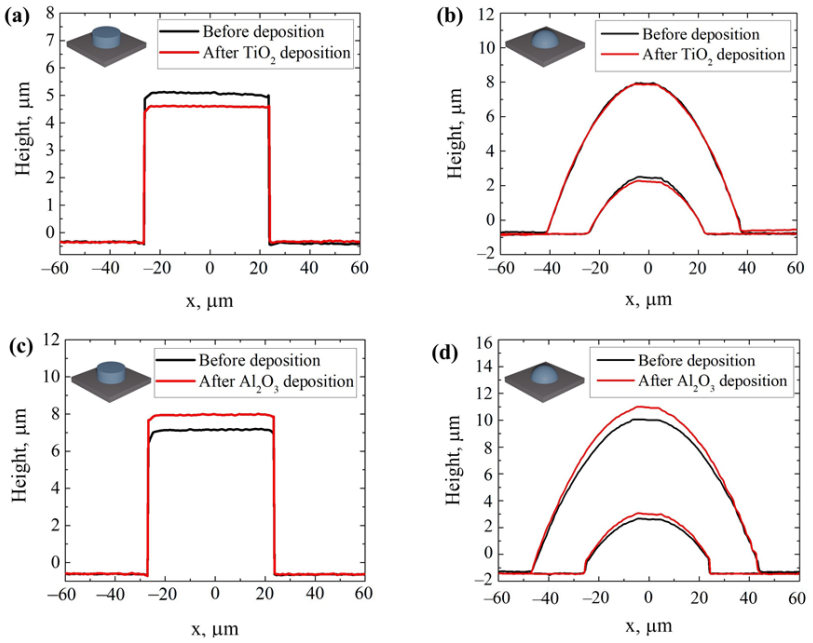


Figure 40. Profiles before and after deposition of TiO_2 thin film on (a) circular-shaped flat surface microstructure and (b) micro-lenses with diameters of ≈ 50 µm and ≈ 80 µm; profiles before and after deposition of Al_2O_3 thin film on (c) circular-shaped flat surface microstructure and (d) micro-lenses with diameters of ≈ 50 µm and ≈ 80 µm.

Moreover, the focal lengths of three ≈ 50 µm and three ≈ 80 µm diameter micro-lenses were measured before (f_0) and after (f) coating deposition. The averaged values and corresponding changes in focal length (Δf) are summarized in Table 4. Changes in focal length correlate with observed variations in micro-lens height. After the deposition of Al_2O_3, the focal length decreased by 7.5 – 8%, accompanied by an increase in micro-lens height. Also, an increase in height was observed for flat surface microstructures. In contrast, TiO_2 deposition results in a decrease in the height of both micro-lenses and flat microstructures, while the focal length increased by 2 – 7%.

Table 4. The stress of the single-layer coatings, the focal length of the micro-lenses before deposition (f_0) and after deposition (f) and coating-induced change in the micro-lens focal length (Δf).

Coating	Stress, MPa	Lens diameter, µm	f_0, µm	f, µm	Δf, %
Al_2O_3	135	50	187 ± 7	172 ± 2	– 8
		80	184 ± 6	170 ± 9	– 7.5
TiO_2	86	45	142 ± 4	152 ± 5	7
		80	156 ± 3	159 ± 5	2

To further understand these observations, the stress of the single-layer coatings deposited on reference fused silica substrates was evaluated using interferometry. Both coatings exhibited tensile stress, with values of 86 MPa for TiO_2 and 135 MPa for Al_2O_3. The reduction in microstructure height after TiO_2 deposition may be attributed to deformation induced by the tensile stress of the deposited film. However, the increase in height observed after Al_2O_3 deposition cannot be explained by film stress alone. It can be assumed that the growth of the Al_2O_3 film is likely related to these changes. TMA precursor molecules are relatively small and can diffuse into the near surface region of the porous polymer, leading to swelling and an increase in microstructure height. Possible penetration of TMA into the polymer bulk is consistent with the previously discussed QCM results (Subsection 3.2.3). Furthermore, TMA penetration into the porous polymers and similar swelling effects in polymer substrates following Al_2O_3 deposition by ALD have been reported in previous works [138,139]. Conversely, TDMAT molecules are significantly larger and probably less likely to permeate into the polymer. Therefore, the observed deformation of the micro-optics after TiO_2 deposition was likely predominantly caused by film stress.

Furthermore, the surface morphology of uncoated and ALD-coated microstructures was investigated using AFM. Figure 41 shows 3D AFM images of flat surface microstructures before and after deposition of Al_2O_3 and TiO_2. In both cases, a slight reduction in surface roughness was observed after coating. This decrease can be attributed to the ability of the ALD coating to fill in surface grooves and irregularities, resulting in a smoother substrate surface.

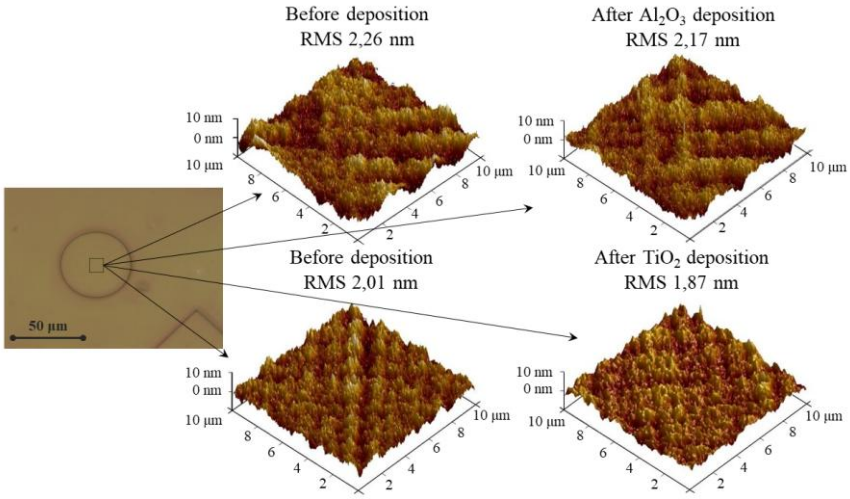


Figure 41. Surface morphology of flat surface microstructures before and after deposition of Al_2O_3 and TiO_2 films (scan area 10 µm × 10 µm).

3.2.5 Antireflective coatings on micro-optics

As the optical properties of the hybrid-polymer and individual layers were established, the AR coating for the target wavelength of 633 nm was designed (Figure 42). The coating was subsequently produced according to the optimized design and consisted of 23 nm TiO_2 and 131 nm Al_2O_3 layers. First, the optical performance of the AR coating deposited on a reference fused silica substrate was evaluated. The measured reflectance of the experimental coating was overall consistent with the theoretical design. Minor discrepancies between the theoretical and measured spectra in the UV spectral range can be attributed to absorption of TiO_2. The AR coating reduced the reflectance of a single SZ2080™ surface from 3.3% to 0.1% at a wavelength of 633 nm.

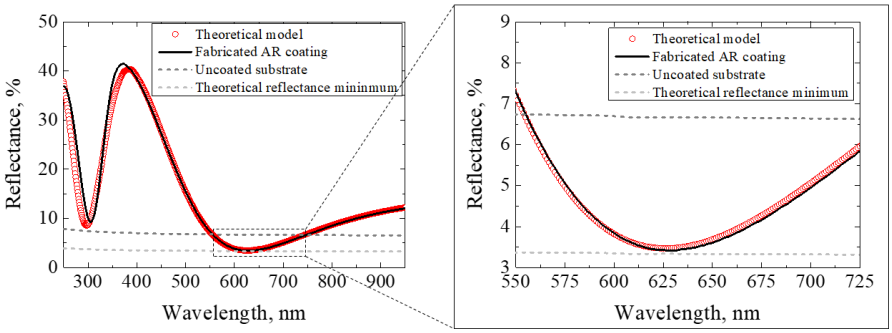


Figure 42. Simulated and experimental reflectance spectra of AR coating targeted for 633 nm.

The same deposition process of AR coating was applied to micro-optical elements. However, due to small dimensions of micro-lenses, direct measurement of absolute transmittance was not feasible. Instead, the relative transmittance of approximately 95 μm diameter micro-lenses was evaluated at a wavelength of 633 nm. Measurements were performed on three separate micro-lenses before and after AR coating deposition, and the averaged values are shown in Figure 43a. The relative transmittance of the micro-lenses increased by 3.7% after coating. In addition, the absolute transmittance of flat surface microstructures was measured, showing a comparable increase of 3.6% after AR coating deposition. Moreover, imaging quality was evaluated before and after coating using a USAF 1951 target. Representative images are shown in Figure 43 b, c, and no degradation in image quality was observed after coating.

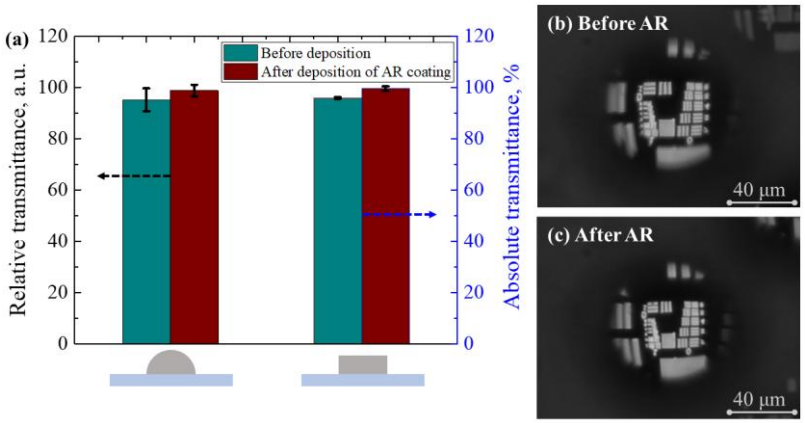


Figure 43. (a) Relative transmittance of the ≈ 95 µm diameter micro-lens and absolute transmittance of the flat surface microstructure before and after AR coating deposition at the wavelength of 633 nm; USAF image (b) before and (c) after AR coating deposition.

Furthermore, the influence of the AR coating on the geometry of the micro-optical components was determined. The profiles of circular flat surface microstructures and micro-lenses with diameters of ≈ 45 µm and ≈ 95 µm were evaluated before and after AR coating deposition (Figure 44 a, b). No significant changes in the geometry of the microstructures were observed. Nevertheless, the focal length increased by 1.5 – 3% after coating (Table 5).

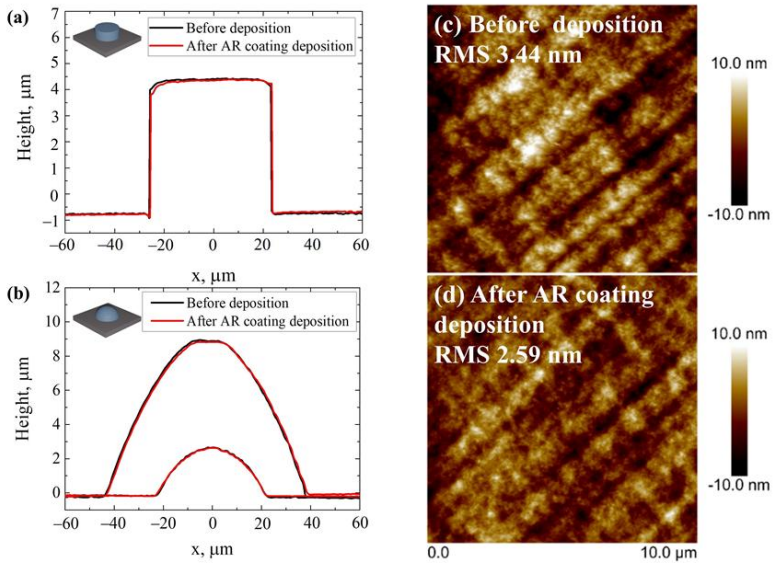


Figure 44. Profiles before and after the deposition of AR coating on (a) circular-shaped flat surface microstructures and (b) ≈ 45 µm and ≈ 95 µm diameter micro-lenses; AFM images of flat surface microstructures (c) before and (d) after the deposition of AR coating.

The AR coating exhibited tensile stress with a value of 127 MPa. Since the first deposited layer was TiO_2, the observed increase in focal length can be attributed to stress-induced deformation of the micro-lenses. However, the magnitude of the focal length change is close to the measurement errors, and thus a contribution of these errors cannot be fully excluded. The surface morphology of the microstructures was also evaluated before and after AR coating deposition. As shown in Figure 44 c and d, the coating reduced the surface roughness from 3.4 nm to 2.6 nm.

Table 5. The stress of the AR coating, the focal length of the micro-lenses before deposition (f_0) and after deposition (f) and coating-induced change in the micro-lens focal length (Δf).

Coating	Stress, MPa	Lens diameter, μm	f_0, μm	f, μm	Δf, %
AR	127	45	182 ± 7	185 ± 6	1.5
		95	190 ± 5	196 ± 5	3

Finally, the feasibility of ALD for depositing conformal AR coatings simultaneously on all surfaces of stacked micro-optical components with multiple interfaces was evaluated. Three different stacked microstructures were fabricated, each consisting of two, four, and six interfaces. SEM images of these multi-level microstructures are shown in Figure 45. After fabrication, the transmittance of the microstructures was measured at a wavelength of 633 nm. During characterization, the substrate on which microstructures were fabricated, was used as the reference, as a result, the measured values represent only the transmittance of the fabricated microstructures.

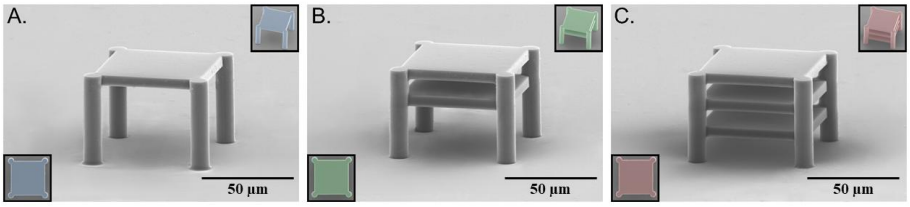


Figure 45. SEM images of fabricated stacked multi-level microstructures consisting of (a) two, (b) four, and (c) six interfaces.

Since each interface contributes to reflection losses, an increase in the number of interfaces leads to a reduction in total transmittance of the element, as shown in Figure 46. At 633 nm, the transmittance of the structures consisting of two, four and six interfaces were approximately 92%, 86%, and 77% for the microstructures consisting of two, four and six interfaces, respectively. Subsequently, an AR coating designed for 633 nm was deposited

on the same multi-level microstructures using ALD. After coating deposition, the transmittance increased to 99.0%, 98.5%, and 98.0%, respectively. The observed increase in transmittance is consistent with conformal deposition of the AR coating across multiple interfaces of the multi-level microstructures. Significant variations in coating thickness would be expected to shift the transmittance maximum and reduce the transmittance relative to the designed value. Although a significant improvement in transmittance was achieved, the measured values remained below the target transmittance of > 99%. This discrepancy is likely related to surface contamination prior to deposition process, as no cleaning procedure was performed before the ALD process. Therefore, surface preparation procedures before coating should be utilized in future experiments.

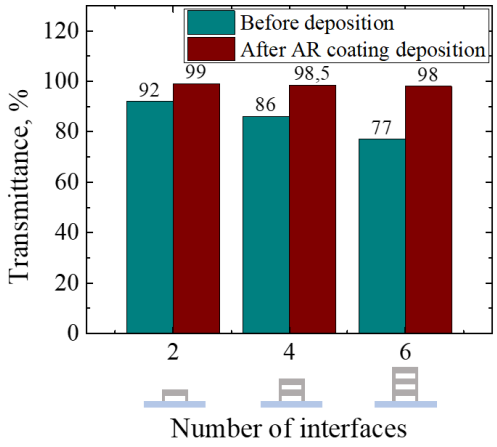


Figure 46. Transmittance of stacked microstructures before and after AR coating deposition measured at the wavelength of 633 nm.

Moreover, the same AR coating was also produced on micro-triplets consisting of three stacked micro-lenses. The imaging of the triplets was evaluated before and after coating deposition using USAF 1951 resolution target (Figure 47a). Comparison of the taken images revealed no observable optical aberrations or degradation in image quality after coating deposition. These results indicate that the AR coating had no measurable impact on the imaging quality of the multi-lens system. In addition, SEM images of the micro-triplets were acquired before and after AR coating deposition (Figure 47b). After these measurements, no deformation of the structure geometry was observed after ALD coating formation.

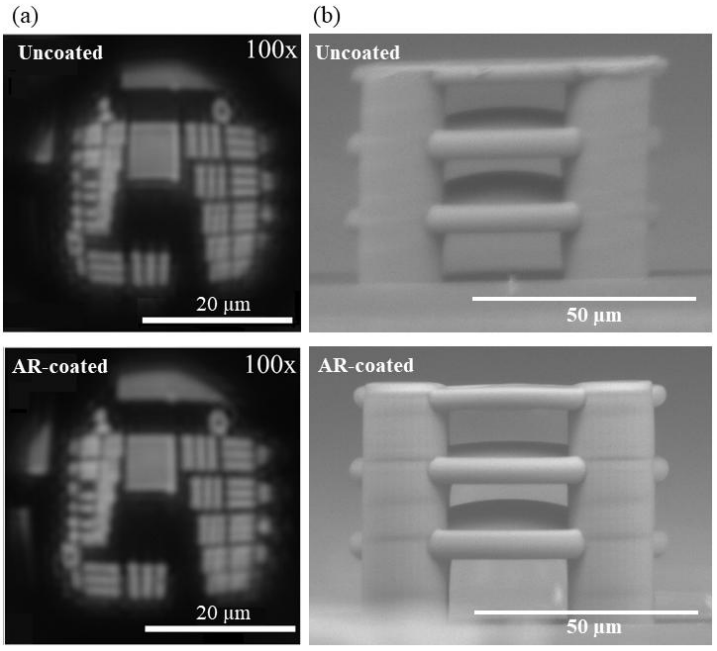


Figure 47. 70 µm diameter micro-triplet: (a) USAF 1951 image before and after AR coating deposition; (b) SEM side view before and after AR coating deposition.

3.3 Main results and conclusions

The potential of ALD thin films to improve the quality and performance of micro-optical components was investigated. First, surface smoothing of micro-lenses exhibiting initial roughness exceeding 100 nm was demonstrated using Al_2O_3 films deposited by ALD. The surface roughness reduction efficiency was confirmed to depend primarily on lateral surface profile rather than on the initial surface roughness. For surfaces exhibiting larger lateral spacings between surface irregularities, deposition of 1200 nm Al_2O_3 reduced the surface roughness by 24%, whereas for micro-lenses with smaller lateral distances between surface asperities, roughness reduction exceeding 39% was observed.

Second, the deposition of thin films on complex hybrid-polymer micro-optical components was investigated. Low temperature PE-ALD was employed to maintain coating quality while preventing thermal degradation of hybrid-polymer optics. After deposition of single-layer Al_2O_3 and TiO_2 coatings on micro-lenses, it was observed that although both films exhibited tensile stress, their impact on micro-lens geometry and focal length was different. TiO_2 films resulted in a decreased micro-lens height and increased

focal length of micro-lenses, which can be related to deformation induced by tensile film stress. Conversely, Al_2O_3 films increased micro-lens height and reduced focal length, which could be associated with diffusion of precursor molecules into the near surface region of the porous polymer substrate, resulting in partial swelling of the material. Furthermore, AR coatings deposited by ALD exhibited low stress and had no significant impact on the geometry and imaging quality of the micro-optics. After AR coating deposition, the relative transmittance of the micro-lenses increased by 3.7%, the absolute transmittance of flat surface microstructures increased by 3.6%, and the transmittance of stacked flat surface microstructures consisting of six interfaces increased from 77% to 98%.

4 IMPROVING ENVIRONMENTAL STABILITY OF NANOSTRUCTURED COATINGS

Nanostructured waveplates enable the fabrication of zero-order waveplates, thereby reducing the size of the optical components and facilitating their integration into compact systems. SiO_2 is one of the most widely investigated materials for nanostructured waveplates due to its wide bandgap of approximately 8.9 eV [143]. All-SiO_2 waveplates exhibit high LIDT, high transmittance, and low optical losses, making them attractive for high-power photonic applications, particularly in the UV spectral range [31]. Nanostructured waveplates are also being considered for polarization smoothing applications in high-power laser systems such as Laser MegaJoule in France [144]. Furthermore, the birefringence of nanostructured waveplates can be locally modified by laser melting, enabling spatial birefringence control for applications such as spatial light modulators [29].

Despite these advantages, porous nanostructured SiO_2 waveplates are sensitive to environmental conditions and can exhibit limited short- and long-term stability of their optical and physical properties. Different approaches have been investigated to reduce the humidity sensitivity of porous GLAD coatings, including hydrophobic surface functionalization, passivation of surface defects, and the use of alternative materials exhibiting lower affinity to water [43,103,104,113]. Hydrophobic functionalization has been shown to reduce spectral shifts in GLAD interference coatings, although minor spectral shifts remained, and an increase in the effective refractive index was observed after treatment [113]. In addition, alternative materials such as Al_2O_3 demonstrated improved retardance stability under changing humidity conditions compared with SiO_2 waveplates [43]. Nevertheless, measurable variations in retardance were still observed in these coatings, indicating that

achieving environmentally stable porous anisotropic coatings remains a challenge.

To address these limitations, two approaches for improving the environmental stability of nanostructured waveplates were investigated in this thesis. First, the utilization of a substitute material for SiO_2 was investigated. LaF_3 was selected because of its large bandgap of approximately 9.4 eV [145]. Its bandgap is larger than those of SiO_2 and Al_2O_3 (≈ 7 eV). Moreover, LaF_3 is suitable for deep UV optical applications, whereas many metal oxide films in this spectral range suffer from optical performance degradation due to intrinsic absorption and laser-induced defect formation [146–148]. Dense isotropic LaF_3 films have been investigated for deep UV and near UV optical coatings [149–152]. However, only limited studies on anisotropic LaF_3 coatings have been reported [31,39], and their potential for UV waveplate applications has not yet been systematically evaluated. In addition, the environmental stability of porous LaF_3 films has not yet been investigated previously.

Second, ALD encapsulation of nanostructured SiO_2 waveplates was investigated. ALD has been widely applied for protection of environmentally sensitive materials, including perovskite and polymer-based optoelectronic devices [115–117]. In optical coating applications, ALD has also been used for stabilization of porous evaporated optical coatings [102,105]. However, ALD encapsulation of highly porous anisotropic GLAD coatings has not yet been systematically studied. Encapsulation of nanostructured waveplates for high-power UV laser applications introduces additional requirements for the protective films. The encapsulating layers must exhibit low absorption, high laser resistance, and sufficiently low residual stress to avoid failure of the porous coatings. Therefore, this work investigates both alternative materials and ALD encapsulation strategies for improving the environmental stability of nanostructured UV waveplates while maintaining low optical losses and high LIDT.

4.1 Nanostructured anisotropic LaF_3 coatings

4.1.1 Single-layer anisotropic LaF_3 coatings

Fabrication of nanostructured UV waveplates operating in transmission requires coatings exhibiting high transmittance, low optical losses, and high birefringence. To optimize deposition process parameters for achieving high birefringence with minimal optical losses, porous anisotropic single-layer LaF_3 coatings with thicknesses of approximately 1 µm were fabricated by

resistive heating evaporation at deposition angles of 60°, 70°, and 80°. For comparison, an anisotropic LaF_3 coating of comparable thickness was deposited by EBE at a deposition angle of 70°. Transmittance and reflectance spectra of nanostructured coatings were measured along both the fast and slow optical axes. At 266 nm, increasing the deposition angle from 60° to 80° resulted in reduced transmittance and increased optical losses, from 3.42% to 10.47% for the fast axis and from 2.26% to 16.32% for the slow axis (Figure *48* a and b). The increase in optical losses at higher deposition angles is attributed to increased porosity and the formation of larger scale surface structures, which increase light scattering. This tendency is consistent with the surface morphology analysis performed using SEM. Top-view SEM images revealed surface coarsening with increasing deposition angle (Figure 48 c–f). In contrast, the EBE-deposited film produced at 70° exhibited higher transmittance and approximately three times lower optical losses compared with the thermally evaporated LaF_3 coating deposited at the same angle. These results can be attributed to the denser film morphology and finer surface structure observed in the SEM images, resulting in reduced scattering losses.

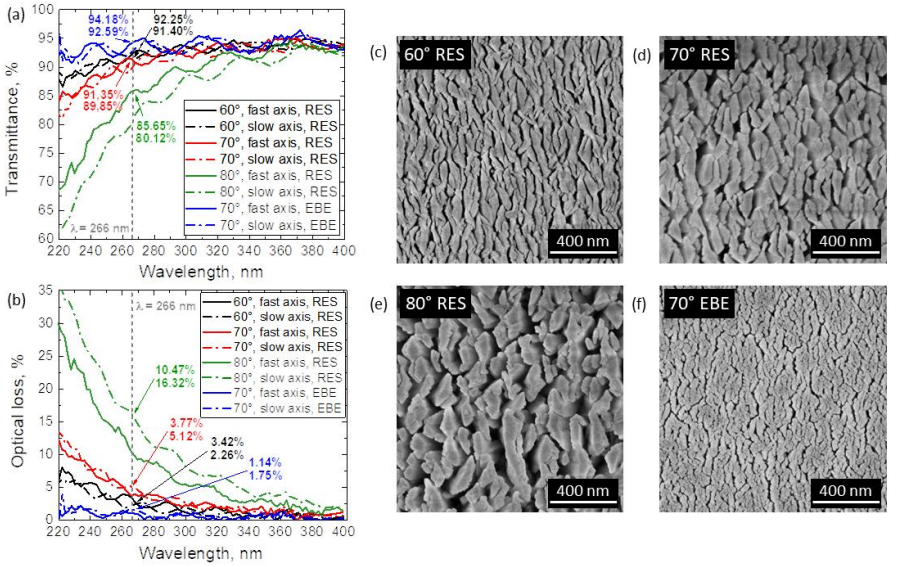


Figure 48. Anisotropic single-layer LaF_3 coatings: (a) transmittance spectra, (b) optical losses, and top-view SEM images of coatings deposited by (c) resistive heating (RES) evaporation at 60°, (d) RES evaporation at 70°, (e) RES evaporation at 80°, and (f) EBE at 70°.

The birefringence of single-layer anisotropic LaF_3 coatings was determined from refractive index dispersions (Figure 49a). Increasing the deposition angle reduced the effective refractive index, consistent with increased porosity arising from enhanced shadowing effects. The highest

birefringence was obtained for LaF_3 coatings deposited using thermal evaporation at 70° angle, reaching Δn = 0.044 at 266 nm. In contrast, LaF_3 thin films deposited using EBE at the same angle exhibited significantly lower birefringence (Δn = 0.030). In addition, the dispersions of retardance were evaluated using spectroscopic ellipsometry (Figure 49b). Retardance values were normalized to a 1 nm film thickness, with thicknesses determined from cross-sectional SEM images (Figure 49c). These measurements confirmed the tendencies observed using spectrophotometry, showing that the highest retardance was achieved in thermally evaporated films at a 70° angle, while EBE-deposited coatings showed the lowest retardance values.

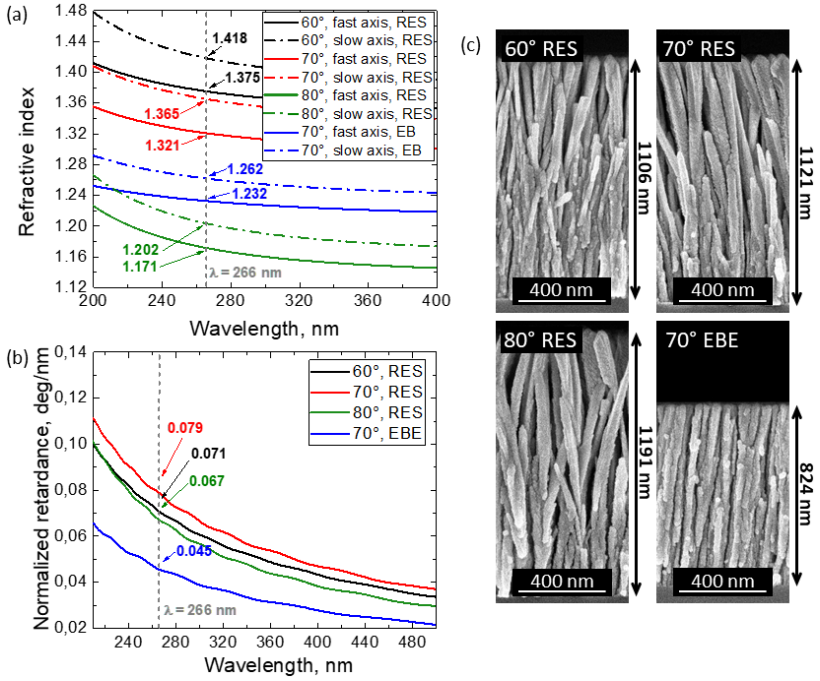


Figure 49. Anisotropic single-layer LaF_3 coatings: (a) effective refractive index dispersions, (b) normalized retardance dispersions, and (c) cross-sectional SEM images.

Since high defect density can reduce the LIDT and increase scattering losses, the defect density of the nanostructured LaF_3 coatings was evaluated using dark-field optical microscopy. Dark-field imaging was chosen because it enhances the contrast of small-scale surface features by collecting only light scattered from defects. For each sample, the surface was scanned using 5× magnification, acquiring 117 micrographs to obtain a complete spatial map (unprocessed images are shown in Figure 50a). The images were subsequently inverted and analyzed using ImageJ software (processed images are presented

in Figure 50b). Increasing the deposition angle from 60° to 80° increased the defect density, from 1.79 defects/mm^2 to 20.31 defects/mm^2. This can be attributed to enhanced coalescence of the columns into larger features at higher deposition angles, which promotes defect formation.

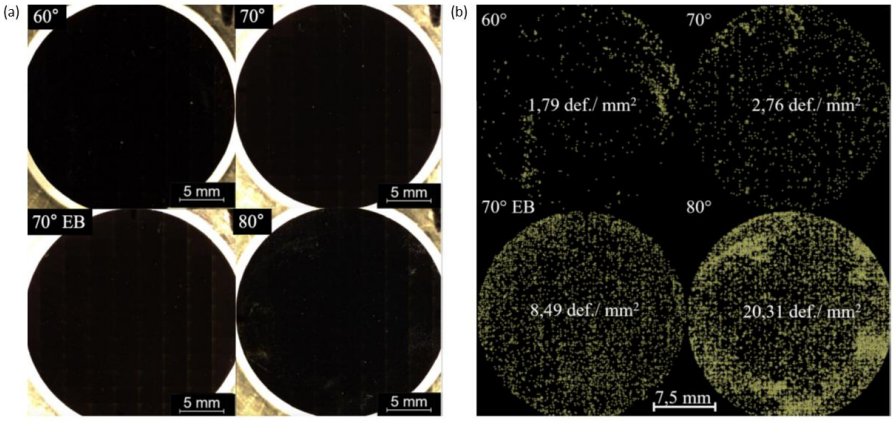


Figure 50. Defect density analysis of anisotropic single-layer LaF_3 coatings: (a) unprocessed images of the samples and (b) processed images of the samples used for defect density calculations.

In contrast, the coating deposited via EBE at a 70° deposition angle exhibited approximately three times higher defect density (8.49 defects/mm^2) than the film deposited via resistive heating evaporation at the same angle. Such defect density in EBE-deposited films may result from random bursts of material ejected toward the substrate during the evaporation process, leading to the incorporation of larger particles and surface defects. During resistive heating evaporation, such effects were mitigated by a protective cover with apertures positioned above the source material, which reduced the deposition of large, ejected particles onto the substrate.

4.1.2 Multilayer anisotropic LaF_3 coatings

In thin film waveplate fabrication using GLAD, the simplest approach is the deposition of a single porous anisotropic layer with sufficient thickness to achieve the required phase retardation. However, increasing the thickness of the anisotropic layer enhances lateral nanocolumn expansion and coalescence, resulting in increased light scattering and reduced transmittance. To suppress these effects, multilayer coatings incorporating dense isotropic interlayers were employed to interrupt column broadening during film growth [31]. In addition, alternating porous (low refractive index) and dense (high refractive index) layers enable the formation of optical interference coatings, allowing

the transmittance of the waveplate to be optimized through layer thickness design.

To optimize the combination of dense isotropic and porous anisotropic layers for achieving highly transparent and low-loss multilayer coatings, a series of multilayer anisotropic coatings were deposited. The main design parameters of the investigated coatings are summarized in Table 6. In all multilayer coatings, the dense layers were deposited at an angle of 30°. Based on the analysis of the single-layer anisotropic LaF_3 coatings, thermally evaporated LaF_3 layers deposited at 60°, which exhibited sufficiently high birefringence and low defect density, were first selected as the anisotropic layers for the multilayer structures.

Table 6. Structure and deposition parameters for multilayer anisotropic LaF_3-based coatings.

Porous anisotropic layers					Dense isotropic layers			
Material	Evaporation method	χ, °	Number of layers	Total thickness, nm	Material	Evaporation method	Number of layers	Total thickness, nm
LaF_3	RES	60	3	1500	LaF_3	RES	3	900
LaF_3	RES	60	5	1500	LaF_3	RES	5	500
LaF_3	EBE	70	5	1500	LaF_3	EBE	5	500
LaF_3	EBE	70	6	1760	SiO_2	EBE	7	410

The first multilayer design consisted of six layers – three porous layers (500 nm thick each) and three dense layers (300 nm thick each). Cross-sectional SEM imaging of nanostructured LaF_3 coatings revealed that the dense interlayers did not form as intended (Figure 51a). Instead, the uninterrupted columnar structure remained through the entire coating, resulting in high optical losses. A second design consisting of ten thinner layers (five porous layers with a thickness of 300 nm and five dense layers with a thickness of 100 nm) was also investigated. For this structure, LaF_3 coatings deposited by both resistive heating evaporation and EBE exhibited behavior similar to that of the six-layer design, characterized by uninterrupted columnar growth and correspondingly high optical losses (Figure 51b). This could be attributed to crystalline or polycrystalline growth of LaF_3 [153], in which adatoms preferentially propagate along the existing lattice planes rather than filling intercolumnar voids.

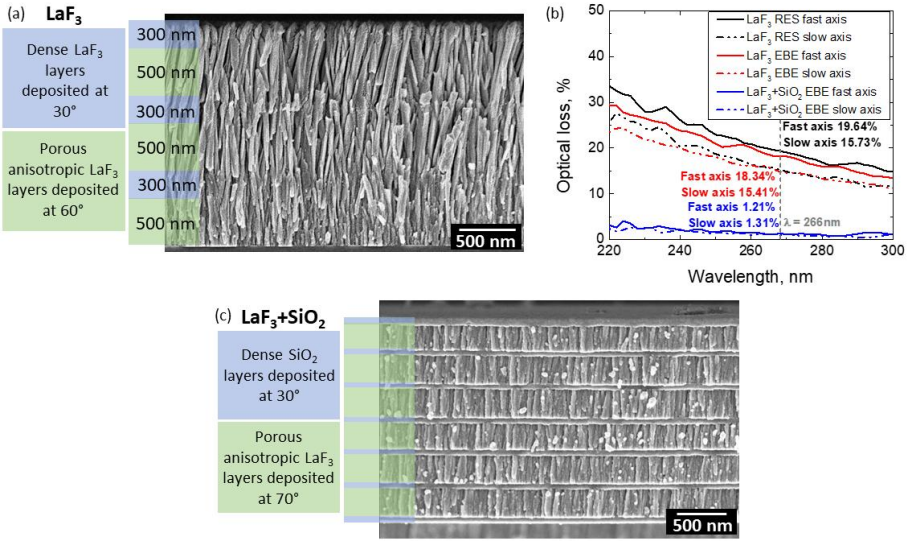


Figure 51. Multilayer anisotropic coatings: (a) cross-sectional SEM image of a 6-layer LaF_3 coating showing regions where dense layers did not form, (b) optical losses of 10-layer LaF_3 and LaF_3+SiO_2 coating, and (c) cross-sectional SEM image of LaF_3+SiO_2 coating.

In the final design, porous anisotropic LaF_3 layers were alternated with dense isotropic SiO_2 interlayers. SiO_2 tends to grow in an amorphous phase and consequently nucleated as continuous dense layers (Figure 51c). Such an approach reduced optical losses at 266 nm from > 18% to 1.21% for the fast axis and from > 15% to 1.31% for the slow axis (Figure 51b).

4.1.3 Waveplates based on nanostructured coatings

Finally, λ/4 waveplates based on porous nanostructured coatings for the wavelength of 266 nm were fabricated. Three different designs were investigated and compared: i) multilayer LaF_3 waveplate, consisting of anisotropic LaF_3 layers and isotropic SiO_2 interlayers (LaF_3+SiO_2 waveplate); ii) single-layer LaF_3 waveplate, protected with a dense SiO_2 cladding layer (LaF_3+SiO_2 c.l. waveplate); iii) multilayer SiO_2 coating, consisting of alternating porous anisotropic and dense isotropic SiO_2 layers (all-SiO_2 waveplate). The deposition parameters and structure of these coatings are listed in Table 7. The design and deposition parameters for all-SiO_2 waveplate were based on the earlier studies [31,121].

Table 7. Structure and deposition parameters for quarter-wave nanostructured waveplates for 266 nm.

Porous anisotropic layers					Dense isotropic layers		
Material	Evaporation method	χ, °	Number of layers	Total thickness, nm	Material	Evaporation method	Total thickness, nm
LaF_3	EBE	70	7	1922	SiO_2	EBE	435
LaF_3	RES	60	1	1200	SiO_2 (c.l.)	EBE	100
SiO_2	EBE	70	7	1910	SiO_2	EBE	440

First, the transmittance and optical losses of the fabricated waveplates were evaluated (Figure 52). The multilayer LaF_3+SiO_2 waveplate exhibited transmittance values of 91.72% and 90.78% for the fast and slow axes, respectively, with optical losses of 1.13% (fast axis) and 0.85% (slow axis). In contrast, the single-layer LaF_3+SiO_2 c.l. waveplate exhibited lower transmittance (< 90%) and higher optical losses of 4.11% and 3.06% for the fast and slow axes, respectively. Since this waveplate consisted of a single-layer porous anisotropic LaF_3 coating with a dense SiO_2 protective layer, the thickness of the porous LaF_3 layer was more than 4 times larger compared to the individual LaF_3 layer thickness in the multilayer LaF_3+SiO_2 waveplate design (Table 7). The increased thickness of the porous anisotropic layer may have enhanced column broadening and enhanced light scattering, which likely contributed to the increased optical losses observed in the single-layer LaF_3+SiO_2 c.l. waveplate.

The all-SiO_2 waveplate achieved the highest transmittance of 93.82% for the slow axis. However, the transmittance for the fast axis was approximately 3% lower. This difference can be attributed to layer thickness deviations, which shifted the experimental spectrum toward shorter wavelengths compared to the theoretical design (Figure 52c). The optical losses of the SiO_2 waveplate were 2.11% (fast axis) and 2.08% (slow axis). Although the multilayer LaF_3+SiO_2 waveplate exhibited the lowest optical losses, its transmittance for one surface was approximately 96%. During deposition of the LaF_3+SiO_2 coating, limited process reproducibility was observed, which can be associated with QCM instability during the alternating deposition of different materials. Consequently, poor thickness control may contribute to discrepancies between the calculated design and the deposited coatings.

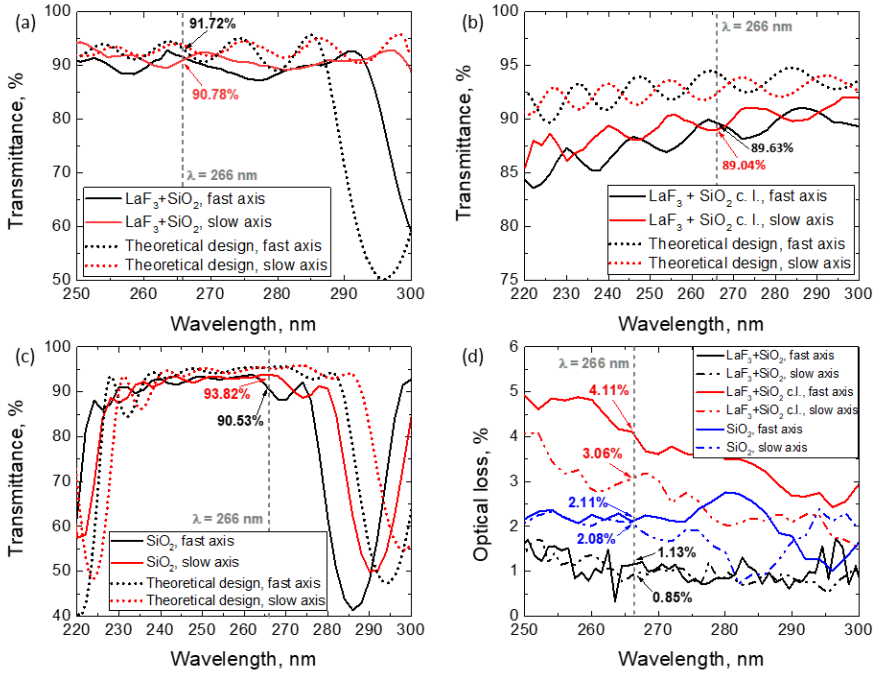


Figure 52. Optical properties of fabricated waveplates: (a) transmittance of multilayer LaF_3+SiO_2 waveplate, (b) transmittance of single-layer LaF_3 waveplate with SiO_2 cladding layer, (c) transmittance of SiO_2 waveplate, and (d) optical losses of all three waveplates.

Furthermore, 1-on-1 LIDT measurements were conducted (Figure 53). For these measurements, nanostructured coatings were deposited on high-quality, chemically etched fused silica substrates. LIDT tests were performed at 266 nm using nanosecond pulses with a pulse duration of 1.7 ns, and a beam diameter of 98.1 μm. Among the investigated samples, the multilayer LaF_3+SiO_2 waveplate exhibited the lowest LIDT of 2.1 J cm^{-2} for fast axis and 3.0 J cm^{-2} for slow axis. This reduced laser damage resistance in the LaF_3+SiO_2 waveplate may be associated with the high density of defects in EBE-deposited LaF_3 layers (Figure 50), with a high number of defects also visible in the laser damage image in Figure 53a. Such defects can absorb laser radiation, leading to heat accumulation, local melting, or stress-induced damage [77]. In contrast, the single-layer LaF_3+SiO_2 c.l. waveplate exhibited the highest LIDT values of 15.6 J cm^{-2} and 15.7 J cm^{-2} for the fast and slow axes, respectively. The highest laser fluence value at which LaF_3+SiO_2 c.l. waveplate could potentially operate is 27.9 J cm^{-2} (fast axis) and 23.4 J cm^{-2} (slow axis). The all-SiO_2 waveplate exhibited significantly lower LIDT values of 6.0 J cm^{-2} (fast axis) and 3.5 J cm^{-2} (slow axis), corresponding to reductions by factors of approximately 2.5 and 4.5 compared to the single-layer

LaF_3+SiO_2 c.l. waveplate for the fast and slow axes, respectively. For comparison, commercially available 266 nm waveplates typically exhibit LIDT values of around 10 J cm^{-2} under nanosecond pulse conditions (e.g., Thorlabs) [154]. Therefore, the LIDT measurements of single-layer LaF_3-based nanostructured waveplates indicate the potential to develop true zero-order waveplates with higher LIDT values than commercial components.

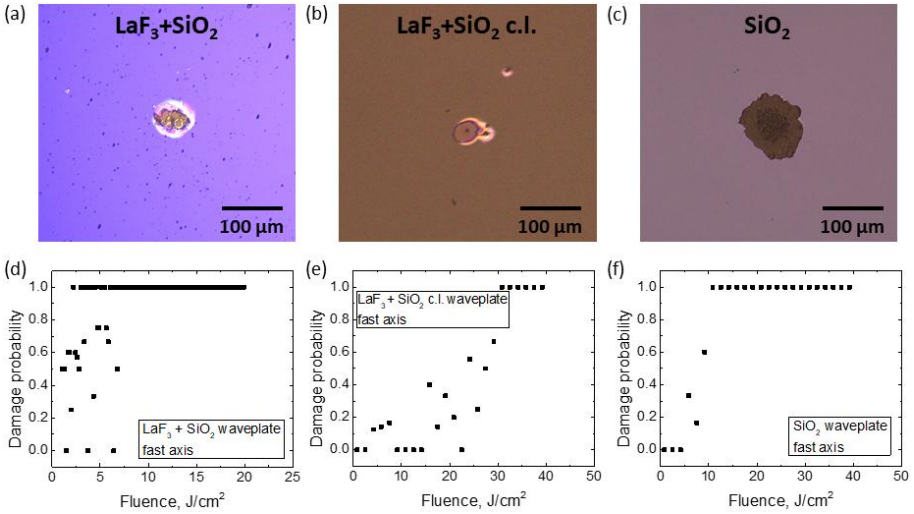


Figure 53. Laser damage morphologies of (a) LaF_3+SiO_2 waveplate, (b) LaF_3 waveplate with SiO_2 cladding layer, and (c) SiO_2 waveplate. Laser damage probabilities of (d) LaF_3+SiO_2 waveplate, (e) LaF_3 waveplate with SiO_2 cladding layer, and (f) SiO_2 waveplate.

Porous nanostructured coatings are known to adsorb water from the atmosphere, which can alter optical properties such as effective refractive index and retardance. Therefore, the environmental stability of the fabricated waveplates was investigated. The short-term stability was evaluated by measuring retardance under varying relative humidity using a birefringence imaging system (Figure 54). The all-SiO_2 waveplate exhibited the largest variation, with retardance decreasing by approximately 5% as humidity was reduced from 30% to 15%. In contrast, the multilayer LaF_3+SiO_2 and single-layer LaF_3+SiO_2 c.l. waveplates were less sensitive to ambient conditions, with retardance changes of –1.2% and –0.8%, respectively.

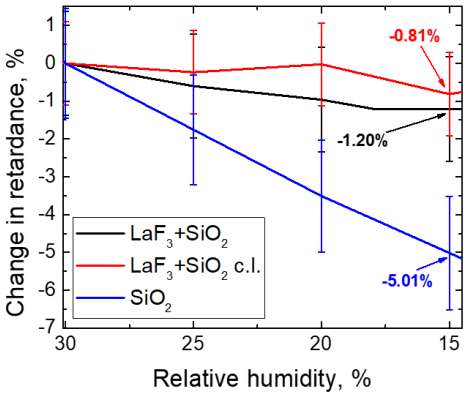


Figure 54. Change in retardance as a function of relative humidity for all fabricated waveplates.

The strong humidity sensitivity of porous nanostructured SiO_2 coatings can be attributed to surface hydroxylation. A high density of silanol groups can promote hydrophilicity and water physisorption [155,156], thereby affecting optical properties of porous films. It has been shown that the presence of water can increase the birefringence and retardance of waveplates based on nanostructured SiO_2 coatings [43,44]. Conversely, LaF_3-based waveplates demonstrated improved retardance stability under varying humidity conditions. Rare-earth oxides, including La_2O_3, have been reported to exhibit low water affinity and hydrophobicity which is attributed to their electronic structure [157,158]. Other La-containing compounds, such as $LaPO_4$, have also been reported as hydrophobic [159]. Moreover, LaF_3 itself is highly insoluble in water [160], and dense LaF_3 coatings have been reported to be moisture-resistant [161]. These observations can explain the enhanced environmental stability of LaF_3-based coatings. Nevertheless, since none of the fabricated waveplates consisted solely of LaF_3, the presence of SiO_2 likely introduces the observed retardance variations. This interpretation is supported by the obtained results – the multilayer LaF_3+SiO_2 waveplate, which contained a higher amount of SiO_2, exhibited a larger retardance decrease, whereas the single-layer LaF_3+SiO_2 c.l. waveplate, with a lower SiO_2 content, (Table 7) showed a smaller change in retardance.

4.2 Encapsulation of nanostructured anisotropic SiO_2 coatings

4.2.1 Analysis of Al_2O_3 films

Encapsulation of porous nanostructured coatings requires conformal, dense films with a low density of defects while maintaining low residual

stress, since porous anisotropic coatings are mechanically fragile and high stress may induce cracking or delamination. Furthermore, the targeted application was environmental stabilization of UV waveplates for high-power lasers, requiring encapsulation layers with minimal optical losses in the UV spectral range.

Since the properties of ALD films strongly depend on the deposition conditions, four different ALD processes for formation of Al_2O_3 encapsulation layers were investigated. Approximately 150 nm thick single-layer alumina coatings were deposited on fused silica substrates using thermal ALD and PE-ALD at deposition temperatures of 60 °C and 150 °C. The deposition parameters of the investigated Al_2O_3 films are summarized in Table 8. The plasma power during Al_2O_3 depositions was set to 100 W. The deposited films were subsequently characterized in terms of refractive index, optical losses, absorption, and residual stress.

Table 8. Deposition parameters for single-layer Al_2O_3 coatings.

ALD process	Deposition temperature, °C	TMA pulse duration, s	Purge duration, s	Oxidizer pulse duration, s	Purge duration, s
Thermal	60	0.02	15	0.02	15
PE-ALD	60	0.02	8	6	8
Thermal	150	0.02	6	0.02	6
PE-ALD	150	0.02	6	6	6

The transmittance and reflectance spectra of the single-layer Al_2O_3 coatings are shown in Figure 55a, while the corresponding refractive indices and optical losses calculated using these spectra are presented in Figure 55b. Thermally grown Al_2O_3 films deposited at low temperature exhibited the lowest refractive index, whereas low-temperature PE-ALD yielded higher refractive index values, consistent with enhanced film densification promoted by energetic plasma species during the plasma-assisted surface reactions [80]. Increasing the deposition temperature to 150 °C during thermal ALD further increased the refractive index, suggesting increased density of the film. The highest refractive indices were obtained for alumina films deposited by PE-ALD at 150 °C.

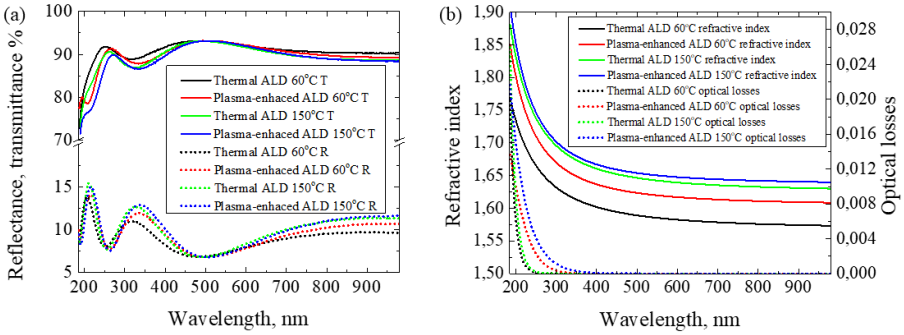


Figure 55. Optical characterization of Al_2O_3 single-layer coatings: (a) transmittance and reflectance spectra and (b) dispersions of refractive indices and optical losses.

While analyzing optical losses, it was observed that thin films produced using thermal ALD demonstrated significantly lower optical losses at 355 nm, whereas PE-ALD films showed losses approximately three and four orders of magnitude greater at low and high deposition temperatures, respectively. To clarify the origin of the optical losses in Al_2O_3 layers, absorption measurements were performed using the LID technique at 355 nm (Figure 56). The lowest absorption was observed for Al_2O_3 films deposited using low temperature thermal ALD. Increasing the deposition temperature led to an increase in absorption, while PE-ALD films exhibited significantly higher absorption values, following the same temperature-dependent trend. The correlation between optical losses derived from spectrophotometric measurements and absorption values obtained by the LID technique indicates that optical losses in ALD-grown Al_2O_3 layers at 355 nm are mainly caused by absorption.

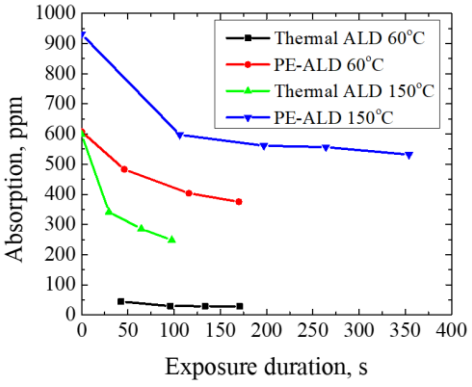


Figure 56. Absorption of Al_2O_3 single-layer coatings measured at 355 nm.

According to previous studies, absorption in ALD Al_2O_3 films deposited at low temperatures commonly originates from intralayer defects, such as

carbon impurities resulting from precursor condensation or insufficient oxidation [162]. At higher deposition temperatures, defects at the film-substrate interface can become increasingly significant, as heating may cause diffusion and defect coalescence thereby leading to the formation of larger defect aggregates that act as absorption centers [163,164]. Moreover, high temperature PE-ALD processes may result in more oxygen vacancies that can also enhance absorption [162]. Furthermore, during LID measurements, a gradual decrease in absorption was noticed with prolonged laser exposure, suggesting the presence of a local laser-annealing or laser conditioning effect [165]. Under UV irradiation, weakly bonded impurities can be removed, leading to a reduction in absorption.

Additionally, the residual stress of the single-layer Al_2O_3 coatings was determined. Thermally grown Al_2O_3 films exhibited relatively high tensile stress, reaching 436 MPa and 361 MPa at lower and higher deposition temperatures, respectively. These values are consistent with previously reported results, where higher stress is observed at lower deposition temperatures and decreases with increasing deposition temperature [85,86]. In contrast, films deposited using PE-ALD exhibited significantly lower stress. A tensile stress of 156 MPa was observed for films deposited at 60 °C, while a transition to compressive stress of 76 MPa occurred at 150 °C. With increasing deposition temperature, the contribution of thermal stress to the total residual stress in ALD Al_2O_3 films increases. However, even at 150 °C, the impact of thermal stress remains limited, with only ≈ 10% of the total stress originating from thermal stress [85,166]. The dominant contribution to stress in ALD Al_2O_3 films is intrinsic stress associated with film growth, where strained bonds are formed, resulting in tensile stress. The compressive stress observed in PE-ALD films deposited at 150 °C can be attributed to the impact of ion bombardment and higher kinetic energy of the molecules [167]. A transition from tensile to compressive stress in PE-ALD Al_2O_3 films with changing deposition temperature has been also reported in the literature [87].

4.2.2 Encapsulation of nanostructured SiO_2 coatings

After evaluating the properties of the Al_2O_3 single-layer coatings, 1.85 µm thick multilayer anisotropic all-SiO_2 coatings were produced using the GLAD technique. The coating design consisted of nine alternating dense isotropic and porous anisotropic SiO_2 layers: five dense layers deposited at a 30° deposition angle, and four porous layers deposited at a 70° angle. The detailed design of the nanostructured SiO_2 coating is provided in Table 9.

Table 9. Structure of the multilayer anisotropic SiO_2 coating. The design is expressed in the order from the substrate to the air.

Layer number	Material	Deposition angle, °	Thickness, nm
9	Dense SiO_2	30	50
8	Porous SiO_2	70	400
7	Dense SiO_2	30	50
6	Porous SiO_2	70	400
5	Dense SiO_2	30	50
4	Porous SiO_2	70	400
3	Dense SiO_2	30	50
2	Porous SiO_2	70	400
1	Dense SiO_2	30	50

Encapsulating Al_2O_3 layers of varying thickness were then deposited on porous anisotropic SiO_2 coatings to evaluate the feasibility of ALD encapsulation for mechanically sensitive porous nanostructured coatings. 5 nm, 25 nm, and 45 nm thick Al_2O_3 encapsulation layers were deposited using thermal ALD at 60 °C. An illustration of the porous nanostructured coatings before and after encapsulation is presented in Figure 57 a and b, respectively.

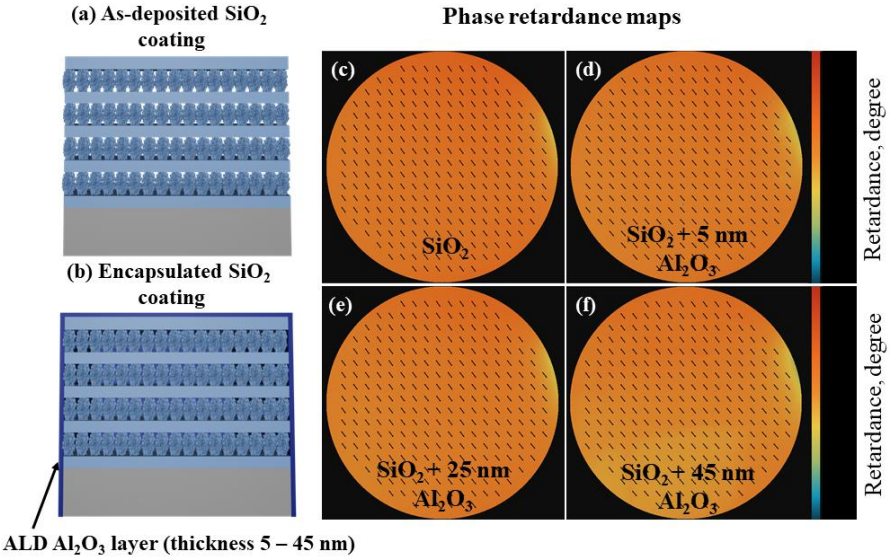


Figure 57. Schematic representation of (a) as-deposited and (b) encapsulated nanostructured anisotropic SiO_2 coatings with thin Al_2O_3 layers. Retardance maps of the anisotropic SiO_2 coatings: (c) before encapsulation, (d) after encapsulation with 5 nm Al_2O_3, (e) after encapsulation with 25 nm Al_2O_3, and (f) after encapsulation with 45 nm Al_2O_3. Measurements were performed at 488 nm.

The retardance of both as-deposited and encapsulated nanostructured coatings was analyzed using a birefringence imaging system. Retardance maps of as-deposited and encapsulated SiO_2 coatings are demonstrated in Figure 57 c–f. All maps were obtained 8 months after deposition to ensure sample stabilization. No significant changes in retardance across the entire sample were observed after encapsulation. Retardance measurements were conducted over a period of up to 8 months.

It has been reported that the retardance of moisture-sensitive anisotropic coatings gradually increases due to water adsorption within the porous nanocolumnar nanostructure, which leads to an increase in the effective refractive index and birefringence [44,103]. To investigate this long-term degradation effect, the temporal evolution of retardance was monitored (Figure 58a). It was observed that the retardance of unprotected SiO_2 coating increased over time until it stabilized at a maximum value. The observed increase in retardance over time is consistent with previously reported behavior of anisotropic GLAD films. After deposition of Al_2O_3 layers, nanostructured SiO_2 coatings have also shown an increase in retardance.

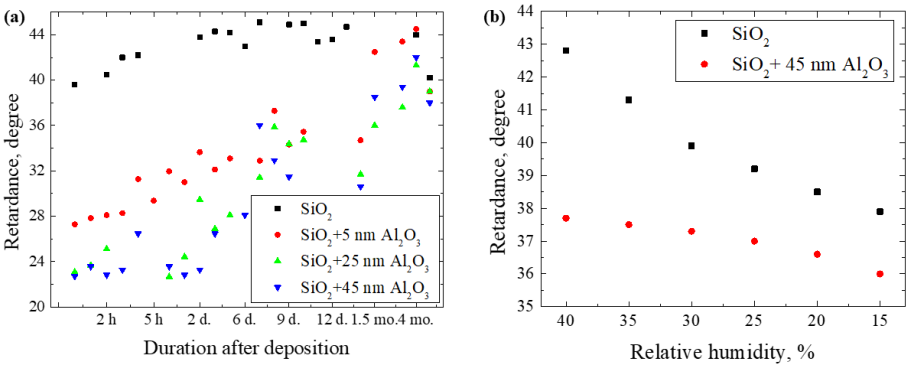


Figure 58. (a) Dependence of retardance on ambient exposure duration and (b) dependence of retardance on relative humidity for the as-deposited anisotropic SiO_2 coating and the coating encapsulated with 45 nm Al_2O_3. Measurements were performed at 488 nm.

Additionally, the retardance of the as-deposited and encapsulated SiO_2 coatings was measured under varying relative humidity conditions to evaluate short-term environmental stability (Figure 58b). For as-deposited anisotropic coatings, the retardance decreased from $\approx 43°$ in a humid environment to $\approx 38°$ in a dry environment. After encapsulation by ALD, the retardance variation was reduced, changing from $\approx 38°$ to $\approx 36°$. The ALD encapsulation with 45 nm thick Al_2O_3 layer reduced the impact of humidity on retardance of the nanostructured coating, however, slight changes in retardance were still observed. These changes can be related to lower density of Al_2O_3 film

produced using low temperature ALD process or insufficient thickness of encapsulating layer.

In the second step, thicker protective Al_2O_3 films were deposited on porous nanostructured SiO_2 coatings using different ALD process parameters. Approximately 150 nm thick Al_2O_3 films were produced using four different ALD process conditions: (i) thermal ALD at 60 °C, (ii) thermal ALD at 150 °C, (iii) PE-ALD at 60 °C, (iv) PE-ALD at 150 °C (Figure 59).

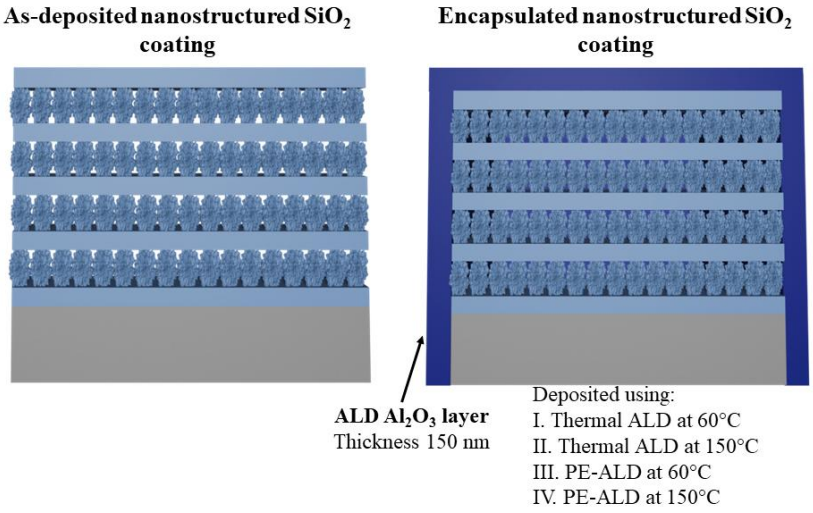


Figure 59. Schematic representation of the nanostructured anisotropic SiO_2 coatings (a) before encapsulation and (b) after encapsulation with 150 nm thick Al_2O_3 layer.

However, thermal ALD encapsulation at both lower and higher deposition temperatures resulted in the formation of cracks within the nanostructured coatings (Figure 60a), which can be attributed to the relatively high stress of thermally grown Al_2O_3 layers (Subsection 4.2.1). The damaged areas were also visible in the retardance maps of the anisotropic coatings, confirming degradation of the nanostructured film (Figure 60 b and c). In contrast, Al_2O_3 films produced via PE-ALD exhibited lower stress and did not induce mechanical damage in the porous coatings, demonstrating better compatibility between the encapsulating layer and the underlying nanostructured coating (Figure 60d).

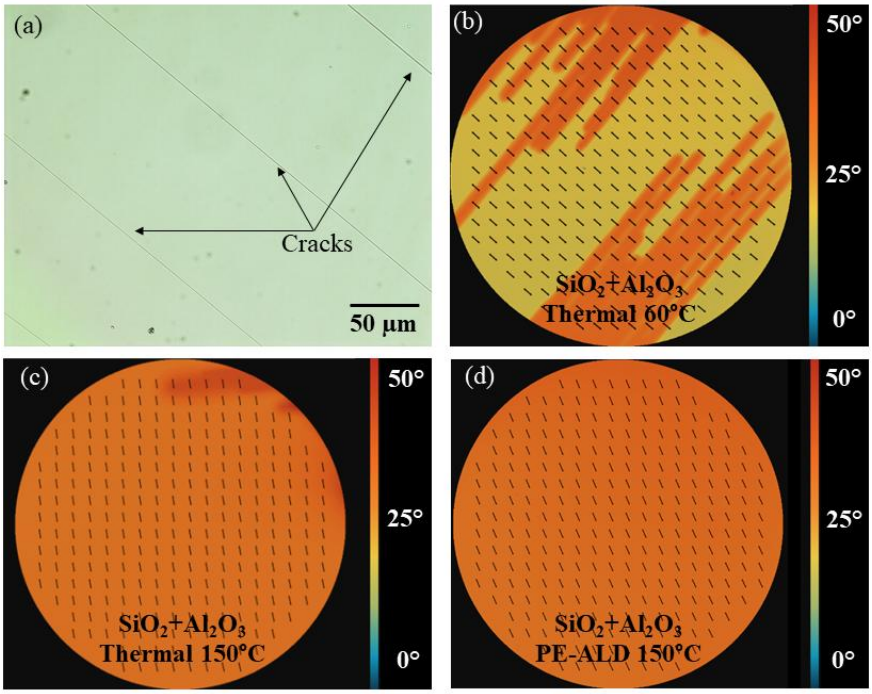


Figure 60. (a) Optical micrograph of anisotropic SiO_2 coating encapsulated using thermal ALD at 60 °C. Retardance maps of anisotropic SiO_2 coatings encapsulated using (b) thermal ALD at 60 °C, (c) thermal ALD at 150 °C, and (d) PE-ALD at 150 °C. Measurements were performed at 488 nm.

Subsequently, the long-term environmental stability of both as-deposited and encapsulated anisotropic SiO_2 coatings was investigated (Figure 61a). The retardance of the SiO_2 anisotropic coatings increased by approximately 25% after 14 days of storage under cleanroom conditions. During long-term retardance monitoring, all investigated samples, including those encapsulated using PE-ALD, exhibited an increase in retardance (Figure 61a). This behavior can be attributed to delayed penetration of air and moisture into the porous structure through defects within the encapsulating layer. During the ALD process, the nanostructured coatings are exposed to vacuum and subsequently sealed by the deposited Al_2O_3 layer. After exposure to ambient atmospheric conditions, pressure equilibration between the encapsulated porous coating and the surrounding environment is expected to occur, resulting in gas and moisture diffusion into the porous structure. As water adsorption within the nanostructured coating increases the effective refractive index and birefringence, a corresponding increase in retardance is observed. Previous studies have shown that defects in ALD Al_2O_3 films may contribute to moisture permeation through the coating [119,168,169]. In particular,

hydroxyl defect clusters can form diffusion pathways that facilitate water transport through chemical exchange reactions, such as $AlO(OH) + H_2O \rightarrow Al(OH)_3$ [168]. These defects originate from the relatively high hydrogen content in ALD Al_2O_3, which varies from < 1 at.% to 22 at.%, depending on deposition temperature and oxidizer type [170,171]. Therefore, it is assumed that defects in the Al_2O_3 encapsulating layers facilitate moisture permeation through the coating, contributing to the observed increase in retardance.

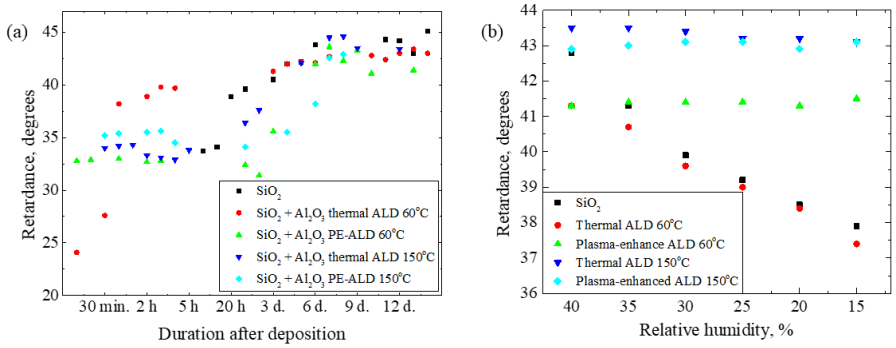


Figure 61. Dependence of retardance on (a) storage duration under ambient conditions and (b) relative humidity for as-deposited and encapsulated nanostructured SiO_2 coatings with 150 nm thick Al_2O_3 layers. Measurements were performed at 488 nm.

After the retardance of all coatings reached a stable value, the dependence of retardance on relative humidity was evaluated, referred to as short-term environmental stability (Figure 61b). The as-deposited SiO_2 nanostructured coatings exhibited the largest retardance variation as the relative humidity was reduced, showing strong sensitivity to the ambient conditions. Anisotropic coatings encapsulated using thermal ALD also showed instability under varying environmental conditions. As discussed in Subsection 4.2.1, thermally grown Al_2O_3 films exhibited high tensile stress, which resulted in cracking of the anisotropic coatings. These cracks likely acted as water desorption sites from the porous coating as the relative humidity of the environment was reduced. Notably, SiO_2 coatings encapsulated using low temperature thermal ALD process exhibited a larger change in retardance compared to coatings encapsulated at higher deposition temperature. This difference can be explained by a higher number of cracks formed during the low temperature ALD process, enabling faster water exchange between the environment and the nanostructured coating when the relative humidity changes. Conversely, coatings encapsulated at higher temperature contained fewer cracks, resulting in slower moisture exchange and consequently smaller retardance variations. In comparison, nanostructured coatings encapsulated

using PE-ALD demonstrated stable retardance values under varying humidity conditions. These PE-ALD Al_2O_3 films appear to function as barrier layers, limiting the desorption of water from porous coating under dry conditions and thereby stabilizing the optical performance of GLAD coatings.

4.2.3 Encapsulation of nanostructured SiO_2 waveplates

Finally, λ/4 waveplates based on nanostructured anisotropic SiO_2 coatings and designed for operation at 355 nm were fabricated. The SiO_2 coatings were deposited using GLAD, applying the same deposition parameters as described in the previous section. The nanostructured anisotropic coating consisted of 23 alternating dense and porous SiO_2 layers, with a total thickness of approximately 3.9 µm. Based on previously discussed results, only PE-ALD Al_2O_3 films deposited at 60 °C and 150 °C were selected as encapsulating layers, as these films exhibited significantly lower stress and did not induce mechanical damage in the underlying anisotropic coatings (Figure 62).

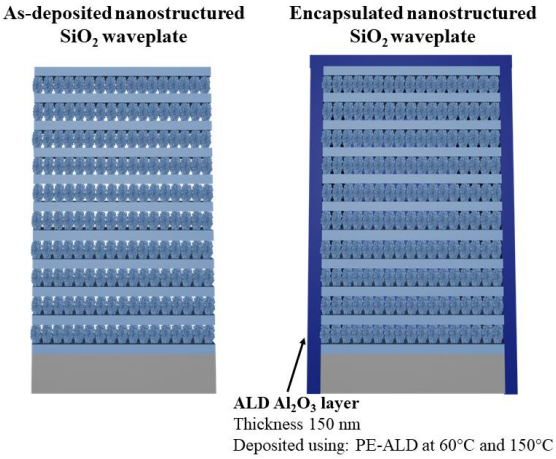


Figure 62. Schematic representation of the waveplates based on nanostructured SiO_2 coatings (a) before encapsulation and (b) after encapsulation with 150 nm thick Al_2O_3 layer.

The short-term environmental stability of the waveplates was evaluated by monitoring the retardance under varying humidity conditions before and after encapsulation (Figure 63 a, b). The measurements demonstrated stabilization of retardance following PE-ALD encapsulation at both higher and lower deposition temperatures, with constant retardance maintained under varying humidity levels. Notably, the λ/4 waveplates were more than twice as thick as the previously studied anisotropic SiO_2 coatings, indicating that PE-ALD encapsulation is applicable to a broader range of coating designs. In addition, the stability of the encapsulated waveplates during prolonged exposure to dry

conditions was investigated (Figure 63c). For these measurements, the encapsulated waveplates were maintained in a dry environment (relative humidity was approximately 15%) for three hours, and the retardance was measured at 15 min intervals. No significant changes in retardance were observed throughout the measurement period. These results indicate that, following an initial pressure equilibration stage, the encapsulated nanostructured coatings exhibit stable optical performance for at least 3 hours. This behavior suggests that although moisture penetration into the porous structure can initially modify the absolute retardance, the encapsulating layer significantly suppresses further humidity-induced changes, thereby enabling stable operation under varying environmental conditions.

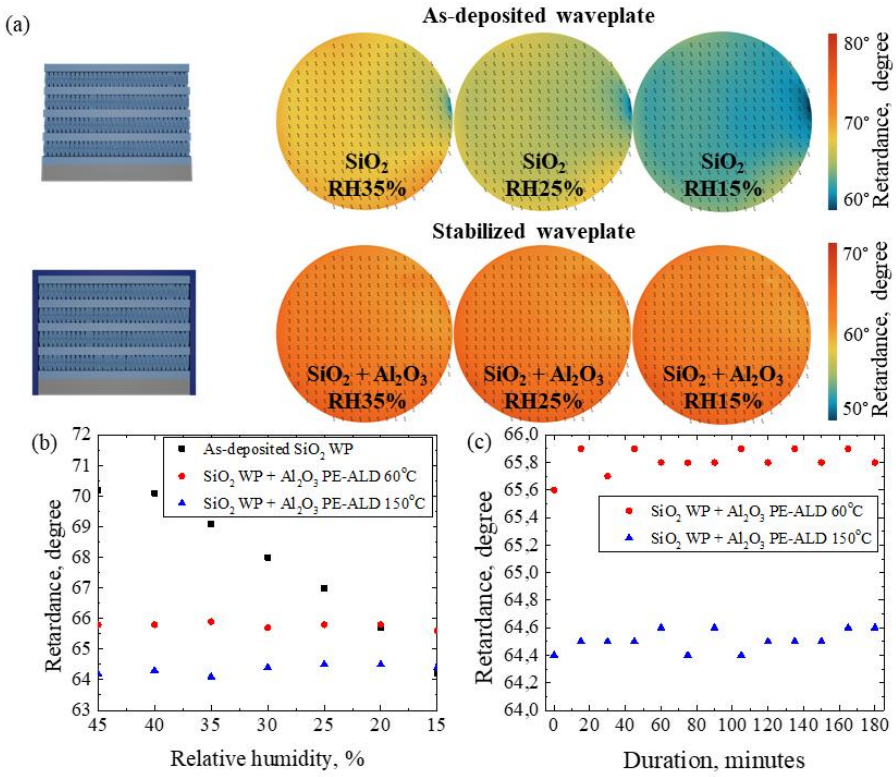


Figure 63. (a) Retardance maps of as-deposited (top) and encapsulated (bottom) SiO_2 waveplates acquired under varying relative humidity (RH) conditions. Dependence of retardance on (b) relative humidity and (c) exposure duration under dry conditions (RH 15%). Measurements were performed at 488 nm.

Nanostructured silica waveplates are widely considered for applications in high-power laser systems. Therefore, it is essential to verify that the encapsulation does not degrade the resistance to laser radiation of the SiO_2

waveplates. 1-on-1 LIDT measurements were performed at 355 nm for both fast and slow optical axes of the waveplates (Figure 64). During LIDT measurements, the laser pulse duration was 2.08 ns, the beam diameter was 61 μm, and the repetition rate was 15 Hz. For these measurements, nanostructured coatings were deposited on high-quality, chemically etched fused silica substrates. The as-deposited SiO_2 waveplate exhibited the highest laser resistance, with LIDT values of 18.6 J cm^{-2} and 18.1 J cm^{-2} for the fast and slow axes, respectively. Encapsulation using low temperature PE-ALD reduced the LIDT to 1.8 J cm^{-2} for the fast axis and 5.3 J cm^{-2} for the slow axis. For waveplates encapsulated using the higher temperature PE-ALD process, resistance to laser damage was further reduced to 1.7 J cm^{-2} for both optical axes. The reduced LIDT observed after encapsulation is most likely related to absorption of the PE-ALD Al_2O_3 layers. Under nanosecond UV radiation, laser damage in dielectric coatings is commonly associated with photothermal mechanisms, where absorption-induced localized heating leads to thermal stress accumulation and subsequent damage of the film [162].

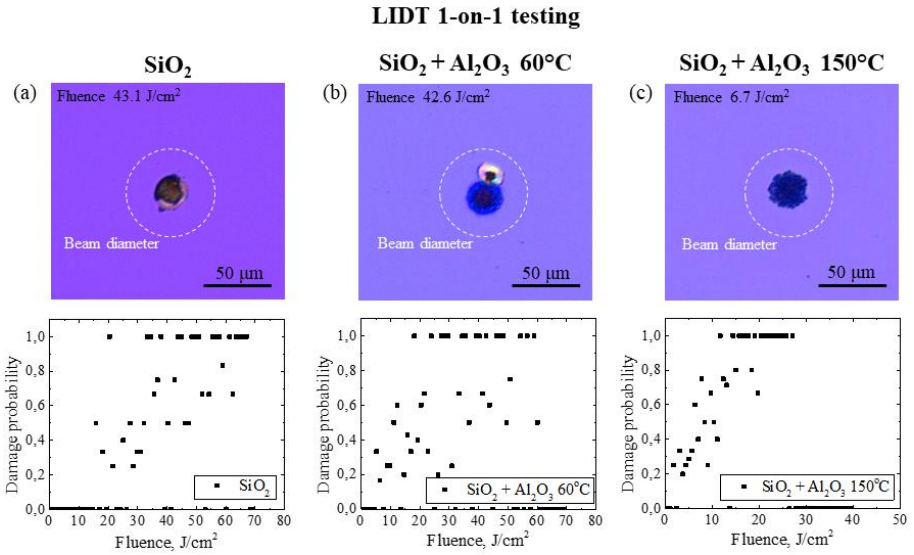


Figure 64. Laser-induced damage characteristics of as-deposited and encapsulated SiO_2 waveplates. Laser damage morphologies (top) and damage probabilities (bottom) for (a) the as-deposited waveplate, (b) the waveplate encapsulated using PE-ALD at 60 °C, and (c) the waveplate encapsulated using PE-ALD at 150 °C. The damage probability data are shown for the slow optical axis.

Thermal annealing is frequently employed to reduce absorption losses in optical coatings [172,173]. Therefore, the samples were annealed at 300 °C

for 2 h and 4 h under an ambient atmosphere. A relatively low annealing temperature was selected because higher annealing temperatures can lead to densification and changes in the microstructure of the anisotropic coating. Such changes are undesirable, as they may affect birefringence or increase light scattering [174,175]. Initially, single-layer Al_2O_3 coatings were annealed to evaluate the effect of thermal treatment on their optical properties. Annealing of Al_2O_3 films deposited using PE-ALD at 60 °C resulted in a minor decrease in film thickness followed by a slight blue shift of the transmittance spectrum (Figure 65a), while no detectable changes in refractive index were observed (Figure 65b). In addition, annealing reduced the optical losses at 355 nm from approximately 0.04% to below 0.01% (Figure 65c). Prolonged annealing did not result in any further measurable changes in the optical properties of the Al_2O_3 films.

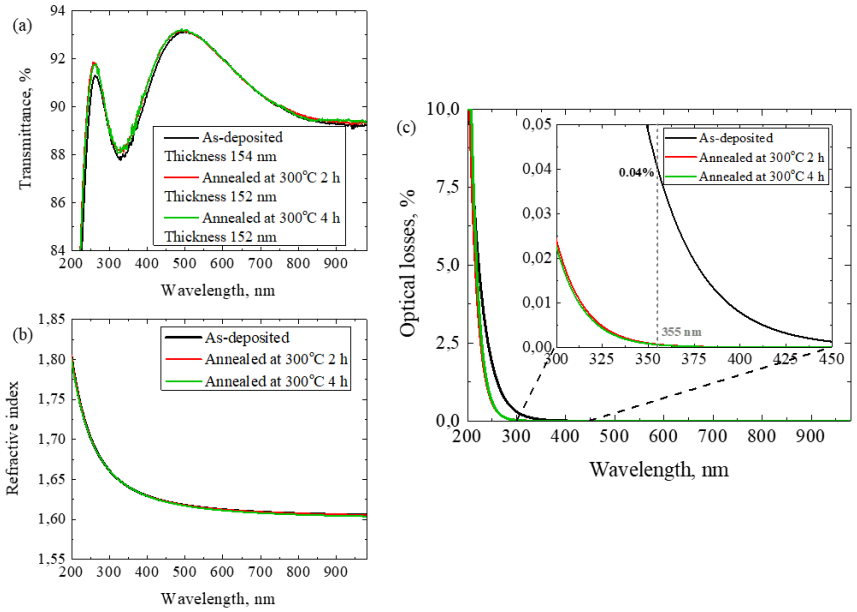


Figure 65. Optical properties of Al_2O_3 films deposited using PE-ALD at 60 °C before and after annealing at 300 °C for 2 h and 4 h: (a) transmittance spectra, (b) dispersions of refractive indices, and (c) optical losses (the inset shows a magnified view of the 300 – 450 nm spectral region).

For Al_2O_3 deposited by PE-ALD at 150 °C, thermal annealing also led to a slight decrease in film thickness (Figure 66a), in addition to a minor increase in refractive index (Figure 66b). After annealing for 2 h, the optical losses at 355 nm decreased from 0.05% to 0.02%, while annealing for 4 h further reduced the losses to approximately 0.006% (Figure 66c). The reduction in optical losses after annealing can be associated with decomposition of residual

organic species originating from the precursor, further oxidation of the film, or reduction of oxygen vacancies, resulting in improved film stoichiometry [173,176].

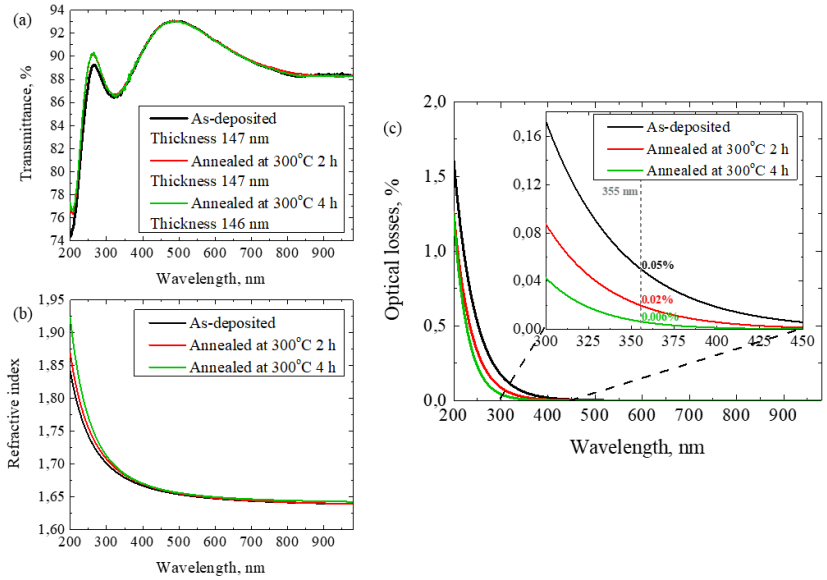


Figure 66. Optical properties of Al_2O_3 films deposited using PE-ALD at 150 °C before and after annealing at 300 °C for 2 h and 4 h: (a) transmittance spectra, (b) dispersions of refractive indices, and (c) optical losses (the inset shows a magnified view of the 300 – 450 nm spectral region).

Subsequently, SiO_2 waveplates encapsulated with Al_2O_3 films deposited by PE-ALD at 60 °C and 150 °C were annealed under the same conditions for 2 h. However, cracking of the coatings was observed after annealing (Figure *67*). For comparison, annealing of the as-deposited anisotropic coating without the ALD encapsulation layer did not result in visible film damage. Previous studies have shown that annealing of porous evaporated coatings can increase tensile stress [177]. In addition, an increase in tensile stress in ALD Al_2O_3 films after annealing has been also reported [178]. Therefore, it can be assumed that annealing of the individual nanostructured coating and individual ALD layer separately did not lead to coating failure because the critical stress required for crack formation was not reached. In contrast, for the encapsulated nanostructured coatings, simultaneous stress changes in both porous SiO_2 coatings and the ALD encapsulation layer may have resulted in higher cumulative tensile stress, leading to crack formation during annealing. However, confirmation of this interpretation would require a comprehensive analysis of stress evolution during annealing for all investigated coatings,

including the nanostructured SiO_2 coatings without encapsulation layer, the individual ALD films, and the encapsulated nanostructured coatings.

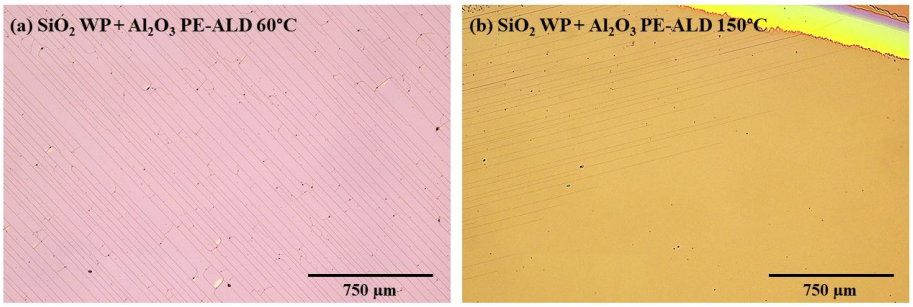


Figure 67. Optical micrographs of nanostructured SiO_2 coatings encapsulated using PE-ALD (a) at 60 °C and (b) at 150 °C after annealing at 300 °C for 2 h.

Additionally, during LID measurements of single-layer Al_2O_3 coatings, a gradual reduction in absorption was observed with prolonged laser exposure, suggesting the possibility of a laser annealing or conditioning effect (Subsection 4.2.1). To further investigate this phenomenon, additional local laser irradiation experiments were performed on encapsulated waveplates. Measurements were conducted along the fast optical axis. During these measurements, a single test site was continuously irradiated while the energy fluence was gradually increased until laser-induced damage was detected. The protocol used for the local laser annealing experiments is described in [179,180].

Three experiments were performed at three separate test sites. In Tests 1 and 2, the energy fluence was continuously increased using approximately 0.5 J cm^{-2} and 0.4 J cm^{-2} increments per pulse for samples encapsulated at lower and higher temperatures, respectively. In Test 3, the fluence gradually increased to a value of 5 J cm^{-2} lower than the highest fluence without damage determined in Tests 1 and 2. The fluence was then maintained constant for an extended period to evaluate whether the sample could withstand prolonged irradiation before further increasing the energy fluence.

For the SiO_2 waveplate encapsulated with an Al_2O_3 film deposited by PE-ALD at 60 °C, the highest energy fluence without laser damage in Tests 1 and 2 was determined to be 35 J cm^{-2} (Figure 68a). In Test 3, the laser fluence was gradually increased to 28 J cm^{-2} and maintained for approximately 130 pulses without observable damage. After further increasing the fluence, damage occurred only when the fluence exceeded 35 J cm^{-2}. This value was significantly higher than the LIDT determined using the conventional 1-on-1 test procedure, where the LIDT along the fast axis was below 2 J cm^{-2}.

A similar tendency was observed for SiO_2 waveplate encapsulated with an Al_2O_3 layer deposited by PE-ALD at 150 °C (Figure 68b). In this case, laser-induced damage occurred only after the fluence exceeded 22 J cm^{-2}. During Test 3, the sample was irradiated at 17 J cm^{-2} for approximately 70 pulses without detectable damage. Subsequent increases in energy fluence resulted in damage when the fluence exceeded 22 J cm^{-2}. In comparison, the LIDT measured using the 1-on-1 test for the fast axis was below 2 J cm^{-2}.

Compared with the conventional 1-on-1 measurements, the local laser irradiation experiments with gradual fluence ramping demonstrated that the encapsulated waveplates were able to withstand substantially higher fluences before damage initiation. Since PE-ALD encapsulation resulted in a reduction of the LIDT and PE-ALD Al_2O_3 films exhibited relatively high absorption, the reduced laser resistance of encapsulated waveplates can be associated with the ALD encapsulation layers. Moreover, a gradual reduction in absorption of PE-ALD Al_2O_3 films during laser exposure was previously observed during LID characterization. These observations suggest the possibility of a local laser annealing or conditioning effect. One possible explanation of improved resistance to laser radiation after local laser annealing is that prolonged laser irradiation can promote removal of residual impurities, further oxidation of the films, or reduction of the defect density in the ALD layers. However, the present experiments do not allow identification of the underlying mechanisms, and additional investigations would be required to verify these assumptions.

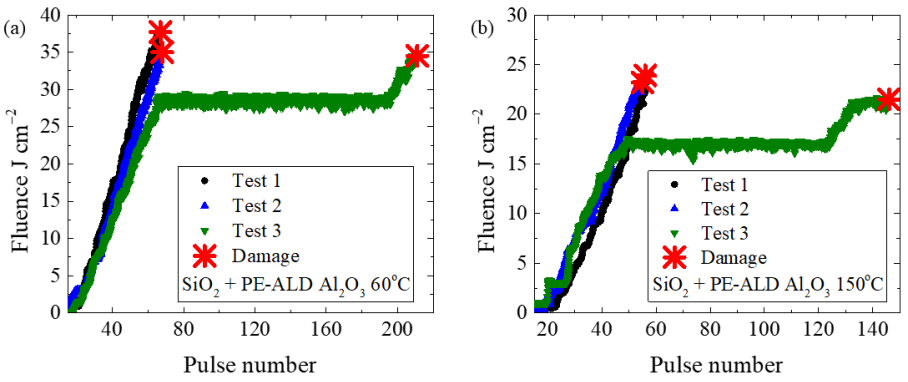


Figure 68. Local laser irradiation experiment performed by gradual increase of laser fluence until damage initiation for (a) the waveplate encapsulated using PE-ALD at 60 °C and (b) the waveplate encapsulated using PE-ALD at 150 °C. Measurements were performed at 355 nm using a pulse duration of 2.08 ns, a beam diameter of 61 µm, and a repetition rate of 15 Hz.

Nevertheless, although PE-ALD encapsulation significantly reduced the LIDT of nanostructured SiO_2 waveplates, the results demonstrate that their laser resistance can be improved with controlled laser irradiation. These findings are particularly important for high-power laser applications, where nanostructured waveplates can be beneficial due to their high laser resistance. The combination of environmental stabilization by ALD encapsulation and local laser annealing may therefore be a promising method for achieving both stable optical performance and high laser resistance.

4.3 Main results and conclusions

Two approaches for improving environmental stability of nanostructured anisotropic coatings were investigated, including the formation of LaF_3-based nanostructured coatings and ALD encapsulation of porous nanostructured SiO_2 coatings. The formation of porous anisotropic LaF_3 coatings was investigated in detail. Resistive heating evaporation and EBE were compared for deposition of anisotropic LaF_3 coatings, and EBE was shown to result in higher defect density compared to resistive heating evaporation. The impact of deposition angle on optical losses, birefringence, and defect density was evaluated. Increasing the deposition angle resulted in increased defect density and optical losses. The highest birefringence was achieved in LaF_3 anisotropic coatings deposited by resistive heating evaporation at 70° angle of substrate incidence.

Combination of porous anisotropic LaF_3 layers and dense isotropic SiO_2 layers enabled the formation of multilayer anisotropic coatings exhibiting significantly reduced optical losses (≈ 1%) compared with single-layer anisotropic LaF_3 coatings (> 3%). However, waveplates consisting of LaF_3 and SiO_2 exhibited lower LIDT (≈ 2 J cm^{-2}), which was attributed to the higher defect density in EBE-deposited coatings, compared with single-layer LaF_3 waveplates (≈ 15 J cm^{-2}). Furthermore, LaF_3-based waveplates showed improved environmental stability. The retardance changed by 0.8% and 1.2% between humid and dry environments for single-layer and multilayer LaF_3-based waveplates, respectively, compared to 5% for nanostructured SiO_2 waveplates.

As a second approach, ALD encapsulation of nanostructured SiO_2 waveplates was investigated. Although thermal ALD enabled the formation of Al_2O_3 films exhibiting low optical losses, the thermally grown films exhibited high residual stress (> 300 MPa), and encapsulation of nanostructured SiO_2 coatings using thermal ALD resulted in cracking of the coatings. Conversely, PE-ALD Al_2O_3 thin films exhibited lower residual

stress (< 200 MPa) and enabled encapsulation of nanostructured waveplates without mechanical damage. The encapsulated waveplates maintained stable retardance under varying humidity conditions. Although PE-ALD encapsulation reduced the LIDT of the waveplates from ≈ 18 J cm^{-2} to below 2 J cm^{-2} for the fast axis due to increased UV absorption, local laser irradiation with gradual laser energy fluence ramping increased the laser resistance of the encapsulated waveplates to values exceeding 20 J cm^{-2} at 355 nm.

CONCLUSIONS

1. The conformal Al_2O_3 films growth during atomic layer deposition enabled surface smoothing of inorganic micro-lenses made from fused silica, CaF_2, BaF_2, and sapphire through progressive filling of surface irregularities. The degree of roughness reduction primarily depends on the initial lateral surface geometry. Al_2O_3 films deposited by atomic layer deposition reduced surface roughness without changing the geometry of the investigated inorganic micro-optical components.
2. Low stress (127 MPa) antireflective coatings deposited by atomic layer deposition on 3D hybrid-polymer micro-optical components minimized reflection losses without distorting component geometry or degrading imaging quality. For multi-level microstructures consisting of six interfaces, the antireflective coatings increased transmittance from 77% to 98%.
3. Retardance variations under varying humidity conditions of LaF_3-based nanostructured waveplates were reduced to 1.2% for multilayer coatings and 0.8% for single-layer coatings, compared with 5% for all-SiO_2 waveplates. The combination of porous anisotropic LaF_3 layers and dense isotropic SiO_2 layers enabled the fabrication of multilayer waveplates exhibiting significantly lower optical losses ($\approx$ 1.1%) compared to single-layer LaF_3 waveplates (> 3%).
4. Plasma-enhanced atomic layer deposition encapsulation stabilized the retardance of nanostructured SiO_2 waveplates under changing humidity conditions after initial equilibration. Although encapsulation reduced the laser-induced damage threshold from $\approx$ 18 J cm^{-2} for the as-deposited waveplate to below 5 J cm^{-2}, local laser annealing through gradual energy fluence ramping increased the damage resistance to $\approx$ 35 J cm^{-2} and $\approx$ 22 J cm^{-2} for waveplates encapsulated with Al_2O_3 deposited at 60 °C and 150 °C, respectively.

SANTRAUKA

Įvadas

Šiuolaikines optines ir lazerines sistemas sudaro įvairūs optiniai komponentai, pavyzdžiui, lęšiai, prizmės, netiesiniai kristalai ir optinės dangos. Šie komponentai yra naudojami šviesos pluošto krypties, formos, pralaidumo, atspindžio ir poliarizacijos valdymui. Be to, pažangiose fotoninėse sistemose vis dažniau reikia nestandartinių komponentų, tokių kaip struktūrizuoti optiniai elementai, kurie pasižymi sudėtinga paviršiaus topografija, 3D geometrija arba vidine mikrostruktūra. Struktūrizuotiems komponentams galima priskirti mikrooptiką, tekstūruotus paviršius ir nanostruktūrizuotas dangas. Tokios struktūros gali suteikti papildomų optinių funkcijų bei gali būti naudojamos kuriant mažo dydžio optines sistemas ir mikrolazerius [1–3].

Analogiškai įprastiems optiniams elementams, struktūrizuotai optikai taip pat yra keliami griežti kokybės reikalavimai, nes šių komponentų kokybė daro įtaką optinių sistemų efektyvumui, patikimumui ir ilgaamžiškumui. Geros kokybės komponentai, priklausomai nuo naudojimo sąlygų, dažniausiai turi pasižymėti mažais optiniais nuostoliais, dideliu atsparumu lazerinei spinduliuotei, mechaniniu atsparumu bei stabiliomis optinėmis ir fizinėmis savybėmis. Kokybiškų parametrų užtikrinimui yra svarbu optimizuoti tiek gamybos, tiek pogamybinius procesus, kurie apima medžiagų parinkimą, poliravimą, ėsdinimą ir plonų sluoksnių nusodinimą [4].

Vienas iš reikšmingiausių iššūkių siekiant pagaminti geros kokybės optinius komponentus yra sugerties, sklaidos ir nepageidaujamų atspindžių optinių nuostolių sumažinimas. Dielektrinių medžiagų sugertį pirmiausia nulemia fundamentinis sugerties kraštas ir vibracinės modos. Tačiau priemaišos, struktūriniai defektai ir paviršinė pažaida gali padidinti sugertį, kuri yra itin žalinga didelės galios lazerinėse sistemose, nes gali sumažinti lazerinės spinduliuotės inicijuotos pažaidos slenkstį (LIDT) [5]. Optinių paviršių atspindžiai sumažina praleidžiamos spinduliuotės intensyvumą. Atspindžių nuostolių sumažinimui įprastai yra taikomas skaidrinančių (AR) dangų nusodinimas arba paviršių nanostruktūrizavimas. Viena iš pagrindinių sklaidos nuostolių priežasčių yra paviršiaus nelygumai. Šie nuostoliai gali sumažinti optinių elementų pralaidumą ir bloginti vaizdinimo kokybę [6,7]. Paviršiaus šiurkštumo sumažinimui optiniai paviršiai įprastai yra poliruojami arba ėsdinami.

Kitas svarbus kokybės kriterijus optiniams komponentams yra stabilumas kintančiomis aplinkos sąlygomis. Įvairios optinės medžiagos, tokios kaip

porėtos nanostruktūrizuotos dangos ir drėgmei jautrūs kristalai, gali pasižymėti jautrumu aplinkos sąlygoms. Aplinkos drėgmės arba organinės taršos poveikis gali paveikti tokių elementų optines ir fizines savybes, sumažinti našumą ir apriboti taikymus [8,9]. Siekiant sumažinti jautrumą aplinkos poveikiui, optiniai elementai gali būti padengiami tankiomis apsauginėmis dangomis arba hidrofobiniais sluoksniais.

Fizinio garų nusodinimo (PVD) metodai yra labiausiai išvystytos technologijos aukštos kokybės optinių dangų formavimui. Tačiau nusodinant dangas ant neplokščių paviršių, PVD metodų taikomumas gali būti ribotas. Optikos gamybos technologijų pažanga lemia vis sudėtingesnių komponentų formavimą, įskaitant laisvos formos elementų ir daugiakomponenčių sistemų, susidedančių iš kelių lęšių, gamybą [7,10,11]. Tačiau tolygus tokių elementų padengimas taikant PVD yra komplikuotas dėl kryptingo nusodinamų garų srauto ir šešėliavimo efekto.

Atominių sluoksnių nusodinimas (ALD) yra perspektyvi technologija tankių ir tolygių dangų formavimui ant sudėtingų 3D pagrindų. ALD proceso principas yra pagrįstas nuosekliomis garų fazės pirmtakų reakcijomis su paviršiumi [12]. Dėl tikslios sluoksnio storio kontrolės ir tolygumo ALD yra taikomas dangų formavimui ant didelio kreivumo ir asferinių lęšių, mikrolęšių ir mikroobjektyvų [7,13–15]. Taip pat buvo pademonstruoti ALD pritaikymai sluoksnių auginimui ant sudėtinga geometrija pasižyminčių struktūrizuotų paviršių, fotoninių kristalų ir mikrostruktūrų [16,17].

Šioje disertacijoje yra tiriamas struktūrizuotų optinių elementų kokybės pagerinimas. Pirma, buvo nagrinėjamas tolygių dangų formavimas ant mikrooptinių komponentų naudojant ALD, siekiant sumažinti mikrooptikos paviršiaus šiurkštumą ir atspindžių nuostolius. Antra, buvo tiriamas porėtų nanostruktūrizuotų dangų stabilizavimas kintančiose aplinkos sąlygose. Siekiant padidinti šių dangų stabilumą buvo pritaikyti du metodai: nanostruktūrizuotų dangų nusodinimas iš medžiagos, pasižyminčios mažesniu jautrumu drėgmei, ir apsauginių sluoksnių formavimas naudojant ALD.

Disertacijos tikslas

Šios disertacijos tikslas buvo pagerinti struktūrizuotų elementų kokybę naudojant atominių sluoksnių nusodinimą, įskaitant tolygių sluoksnių formavimą siekiant sumažinti mikrooptikos optinius nuostolius ir porėtų nanostruktūrizuotų dangų stabilizavimą kintančiose aplinkos sąlygose.

Disertacijos uždaviniai

1. Įvertinti tolygių dangų, suformuotų naudojant atominių sluoksnių nusodinimą, efektyvumą siekiant sumažinti mikrooptinių elementų paviršiaus šiurkštumą neiškraipant jų geometrijos.
2. Ištirti skaidrinančių dangų formavimą ant sudėtingos formos mikrooptinių elementų, pagamintų iš hibridinio polimero, naudojant atominių sluoksnių nusodinimą.
3. Suformuoti nanostruktūrizuotas fazines plokšteles iš LaF_3 ir įvertinti jų stabilumą kintančiose aplinkos sąlygose.
4. Padidinti nanostruktūrizuotų anizotropinių SiO_2 dangų stabilumą kintančiose aplinkos sąlygose taikant atominių sluoksnių nusodinimą.

Darbo mokslinis naujumas ir aktualumas

- Pademonstruotas mikrooptinių elementų paviršiaus lyginimas padengiant elementus tolygiais sluoksniais, suformuotais naudojant atominių sluoksnių nusodinimo technologiją. Lyginant su anksčiau atliktais tyrimais, šiame darbe buvo tiriamas žymiai šiurkštesnių pagrindų šiurkštumo sumažinimas (> 100 nm lyginant su < 10 nm literatūroje). Be to, buvo tiriamas ne plokščių pagrindų paviršiaus lyginimas ir buvo parodyta, kad atominių sluoksnių nusodinimas gali būti taikomas sudėtingos formos komponentų paviršiaus šiurkštumo sumažinimui neiškraipant jų pradinės geometrijos.
- Įvertinta dangų, suformuotų naudojant atominių sluoksnių nusodinimo technologiją, įtaka mikrooptinių komponentų, pagamintų iš hibridinio polimero, geometrijai. Pastebėta, kad elementų geometriją gali paveikti ne tik dangų įtempiai, bet ir kiti reiškiniai, pavyzdžiui, pirmtakų prasiskverbimas į porėto hibridinio polimero paviršių. Pademonstruota, kad tolygios, mažais įtempiais pasižyminčios skaidrinančios dangos gali būti pritaikytos mikrooptinių elementų atspindžių nuostolių sumažinimui neiškraipant jų geometrijos.
- Ištirtas nanostruktūrizuotų anizotropinių lantano fluorido dangų formavimas ir pademonstruotas nanostruktūrizuotų LaF_3 pagrindu suformuotų fazinių plokštelių trumpalaikio stabilumo pagerėjimas kintančiose aplinkos sąlygose.

- Ištirtas apsauginių sluoksnių formavimas ant nanostruktūrizuotų SiO_2 dangų naudojant atominių sluoksnių nusodinimo technologiją. Pasiektas stabilus nanostruktūrizuotų SiO_2 fazinių plokštelių veikimas kintančiose aplinkos sąlygose po apsauginių Al_2O_3 sluoksnių suformavimo naudojant plazminį atominių sluoksnių nusodinimo procesą. Be to, buvo pritaikytas lokalus lazerinis atkaitinimas, kuris padidino fazinių plokštelių, padengtų apsauginiais sluoksniais, atsparumą lazerinei spinduliuotei.

Ginamieji teiginiai

1. Al_2O_3 sluoksniai, suformuoti naudojant atominių sluoksnių nusodinimą, gali sumažinti mikrooptinių elementų paviršiaus šiurkštumą neiškraipydami jų geometrijos, su sąlyga, kad sluoksnio storis yra optimizuotas atsižvelgiant į pradinę paviršiaus topografiją.
2. Tolygios, pasižyminčios mažais įtempiais, dviejų sluoksnių TiO_2/Al_2O_3 skaidrinančios dangos, suformuotos naudojant atominių sluoksnių nusodinimą, sumažina daugiaaukščių hibridinio polimero mikrooptinių elementų atspindžių nuostolius ir neiškraipo jų geometrijos.
3. Porėtos nanostruktūrizuotos LaF_3 dangos pasižymi didesniu trumpalaikiu skirtuminio fazės vėlinimo stabilumu kintančios drėgmės sąlygomis nei porėtos nanostruktūrizuotos SiO_2 dangos.
4. Apsauginiai Al_2O_3 sluoksniai, suformuoti naudojant plazminį atominių sluoksnių nusodinimo procesą, sumažina porėtų nanostruktūrizuotų SiO_2 dangų skirtuminio fazės vėlinimo jautrumą kintančios drėgmės sąlygoms ir nesukelia įtrūkimų porėtoje struktūroje.

Autoriaus ir bendraautorių indėlis

Autorė atliko visus plonų sluoksnių nusodinimus naudojant atominių sluoksnių nusodinimo technologiją ir nanostruktūrizuotų SiO_2 dangų nusodinimus. Autorė atliko didžiąją dalį spektrofotometrinių matavimų, dangų dizainų projektavimų ir optinių savybių charakterizavimų. Autorė pati atliko visus matavimus naudojant optinės emisijos spektroskopiją, atominių jėgų mikroskopiją, interferometriją, optinę profilometriją bei atliko židinio nuotolių ir stabilumo kintančiose aplinkos sąlygose matavimus. Autorė prisidėjo vykdant rezultatų analizę.

Dr. L. Grinevičiūtė vadovavo šiam darbui, konsultavo iškylančiais klausimais dėl eksperimentų ir rezultatų analizės.

Dr. L. Ramalis ir dr. R. Buzelis atliko lazerinės spinduliuotės inicijuotos pažaidos slenksčio ir dangų sugerties matavimus.

M. Slipkauskas atliko nanostruktūrizuotų LaF_3 dangų nusodinimus ir didžiąją dalį šių dangų charakterizavimo.

Dr. A. Selskienė atliko nanostruktūrizuotų dangų matavimus naudojant skenuojančią elektronų mikroskopiją.

Dr. S. Tumėnas atliko elipsometrinius matavimus.

Dr. D. Gailevičius paruošė plonų hibridinio polimero SZ2080™ sluoksnių bandinius.

Prof. dr. M. Malinauskas, dr. D. Ladika, dr. G. Zyla, dr. D. Gailevičius, ir K. Galvanauskas prisidėjo prie hibridinio polimero mikrooptinių komponentų gamybos taikant tiesioginio lazerinio rašymo metodą. Jie taip pat prisidėjo prie mikrooptinių komponentų pralaidumo ir SEM matavimų.

Dr. D. Smith ir prof. dr. S. Juodkazio tyrimų grupė, prisidėjo prie neorganinių mikrolęšių gamybos naudojant lazerinę abliaciją ir SEM matavimų.

Literatūros apžvalga

Pirmajame disertacijos skyriuje yra pateikta literatūros apžvalga. Pirmame poskyryje yra trumpai aprašomi struktūrizuoti elementai – mikrooptiniai komponentai ir nanostruktūrizuotos dangos. Toliau yra apibendrinti disertacijoje taikyti plonų sluoksnių formavimo metodai – terminis garinimas, garinimas elektronų pluoštu, nusodinimas slystančiu kampu ir atominių sluoksnių nusodinimas. Paskutiniame poskyryje yra aprašomi struktūrizuotų optinių komponentų kokybės parametrai – paviršiaus šiurkštumas, atspindžių nuostoliai ir stabilumas kintančiose aplinkos sąlygose.

Eksperimentiniai metodai

Antrajame disertacijos skyriuje yra aprašyti šiame darbe taikyti tyrimų metodai. Pirma, yra aprašomas plonų sluoksnių formavimas naudojant atominių sluoksnių nusodinimo technologiją ir nusodinimo slystančiu kampu metodą. Antra, aptarti mikrooptinių komponentų gamybos metodai. Trečia, pateikti visi taikyti bandinių charakterizavimo metodai: kvarco kristalo mikrosvarstyklės, optinės emisijos spektroskopija, optinių parametrų nustatymas, skirtuminio fazės vėlinimo vaizdinimas, lazerinės pažaidos inicijuoto slenksčio matavimas, įtempių įvertinimas, bandinių struktūros ir

paviršiaus morfologijos analizės metodai, paviršiaus šiurkštumo įvertinimas ir mikrooptinių komponentų charakterizavimas.

Rezultatai

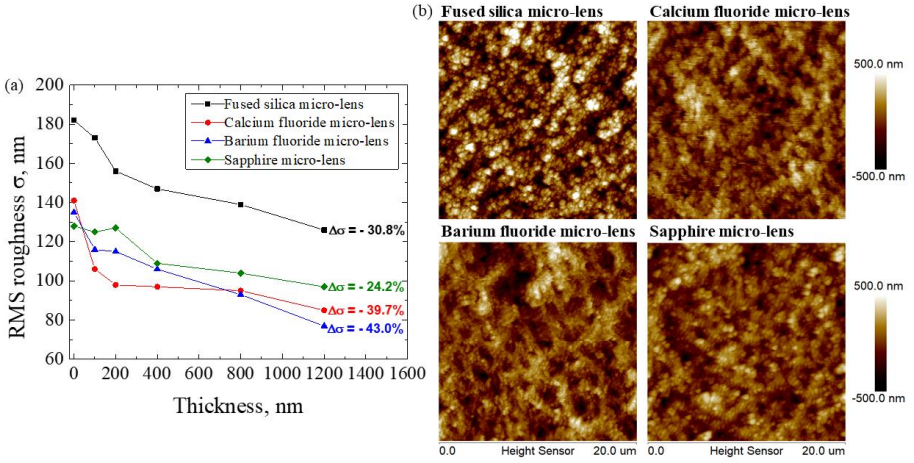
Šio darbo metu gauti rezultatai yra padalinti į du skyrius, atitinkančius dvi pagrindines tyrimų kryptis: mikrooptinių elementų kokybės gerinimą ir porėtų nanostruktūrizuotų dangų atsparumo aplinkos poveikiui didinimą.

Mikrooptikos kokybės gerinimas

Šiame skyriuje pademonstruotas atominių sluoksnių nusodinimo technologijos taikymas tolygių dangų formavimui ant 3D mikrooptinių komponentų. Kadangi buvo vertinami du mikrooptikos kokybės parametrai, skyrius buvo padalintas į dvi dalis. Pirmame poskyryje pateikiamas mikrooptikos paviršiaus šiurkštumo mažinimas, o antrame poskyryje buvo nagrinėjamas mikrooptinių elementų atspindžių nuostolių sumažinimas.

Mikrooptinių komponentų paviršiaus lyginimas

Pirmame poskyryje buvo tiriamas Al_2O_3 sluoksnių nusodinimas ant neorganinių mikrooptinių elementų siekiant sumažinti jų paviršiaus šiurkštumą. Al_2O_3 sluoksniai buvo suformuoti naudojant ALD ant mikrolęšių, pagamintų iš lydyto kvarco, kalcio fluorido, bario fluorido ir safyro. Eksperimentams naudoti mikrooptiniai elementai buvo pagaminti naudojant ultratrumpų impulsų lazerinės abliacijos metodą. Pradinės tyrinėtų bandinių paviršiaus šiurkštumo vertės svyravo tarp 120 nm ir 200 nm. Pirmiausia buvo ištirta Al_2O_3 sluoksnio storio įtaka mikrolęšių paviršiaus šiurkštumui. Bandinių šiurkštumo priklausomybė nuo nusodinto Al_2O_3 dangos storio yra pavaizduota 1 pav. a dalyje. Dangos augimo pradžioje (iki maždaug 400 nm sluoksnio storio), mikrooptinių komponentų šiurkštumas mažėjo sparčiau ir didėjant sluoksnio storiui lėtėjo. Be to, buvo pastebėtas skirtingas mikrolęšių paviršiaus šiurkštumo pokytis nusodinus 1200 nm storio Al_2O_3 sluoksnį, nors pradinis CaF_2, BaF_2 ir safyrinių mikrolęšių šiurkštumas buvo panašus. Po 1200 nm storio Al_2O_3 dangos nusodinimo ant mikrolęšių, pagamintų iš lydyto kvarco, CaF_2, BaF_2 ir safyro, paviršiaus šiurkštumas sumažėjo 30.8%, 39.7%, 43% ir 24.2%, atitinkamai.



1 pav. Mikrolęšių, pagamintų iš lydyto kvarco, CaF_2, BaF_2 ir safyro, paviršiaus morfologijos analizė: (a) paviršiaus šiurkštumo priklausomybė nuo nusodinto Al_2O_3 sluoksnio storio ir (b) pradinės mikrolęšių paviršiaus mikrostruktūros AFM nuotraukos.

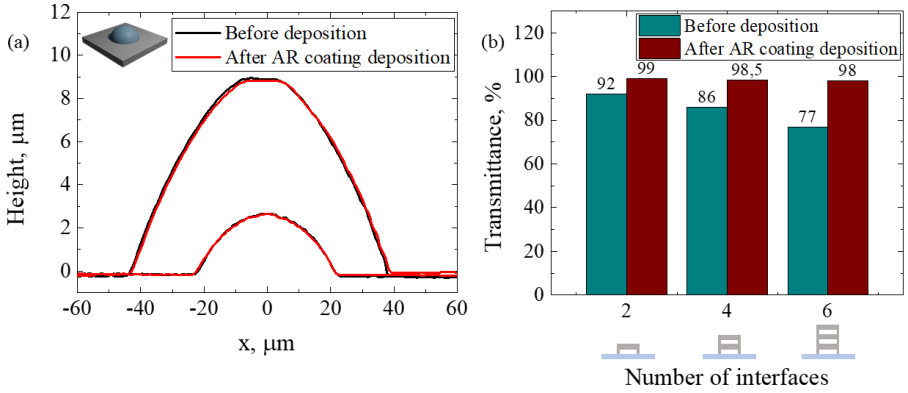
Atlikus papildomą pradinės mikrolęšių paviršiaus morfologijos analizę pastebėta, kad CaF_2 ir BaF_2 mikrolęšių paviršiuje dominuoja smulkesni paviršiaus nelygumai lyginant su bandiniais, pagamintais iš lydyto kvarco ir safyro. Mikrolęšių paviršiaus struktūra prieš dangų nusodinimą yra pateikta 1 pav. b dalyje. Įvertinus vidutinius atstumus tarp paviršiaus nelygumų išilgai bandinio paviršiaus buvo nustatyta, kad didžiausiais atstumais tarp paviršiaus nelygumų pasižymėjo mikrolęšiai pagaminti iš safyro ir lydyto kvarco (470 nm ir 400 nm, atitinkamai). Šių bandinių atveju taip pat buvo pastebėtas mažesnis paviršiaus šiurkštumo pokytis po Al_2O_3 sluoksnio nusodinimo. CaF_2 ir BaF_2 mikrolęšių paviršiuje buvo nustatyti mažesni vidutiniai atstumai tarp paviršiaus nelygumų, kurių apytikslės vertės siekė 270 nm ir 260 nm, atitinkamai. Ant šių mikrolęšių nusodinus 1200 nm storio Al_2O_3 sluoksnį buvo pasiektas didžiausias paviršiaus užlygėjimas. Gauti rezultatai patvirtino, kad paviršiaus šiurkštumo sumažinimo efektyvumui formuojant tolygius sluoksnius didesnę įtaką daro atstumai tarp paviršiaus nelygumų nei nuo pradinis paviršiaus šiurkštumas, kuris parodo nelygumų aukštį.

Siekiant įsitikinti, kad ant mikrooptinių elementų susiformavo tolygi danga, CaF_2 mikrolęšis buvo perskeltas ir atlikta elemento skerspjūvio analizė naudojant SEM. Šie matavimai patvirtino, kad ant mikrolęšio nusėdo tolygus apytiksliai 1200 nm storio Al_2O_3 sluoksnis. Be to, buvo įvertinta ir mikrolęšių forma prieš ir po Al_2O_3 nusodinimo. Po Al_2O_3 nusodinimo nebuvo pastebėta reikšmingų mikrooptinių elementų formos pokyčių.

Skaidrinančių dangų formavimas ant mikrooptinių elementų

Antrajame poskyryje, buvo analizuojamas plonų sluoksnių formavimas ant mikrooptinių elementų, pagamintų iš hibridinio organinio-neorganinio polimero SZ2080™ naudojant tiesioginio lazerinio rašymo metodą. Atsižvelgiant į hibridinio polimero jautrumą temperatūrai, dangų nusodinimui buvo pasirinktas žemos temperatūros (60 °C) plazminis ALD procesas. Pirma, buvo išsiaiškintas vienasluoksnių Al_2O_3 ir TiO_2 dangų poveikis mikrolęšių geometrijai. Al_2O_3 ir TiO_2 sluoksniai pasižymėjo tempiamaisiais įtempiais, tačiau šių sluoksnių poveikis mikrolęšių formai ir židinio nuotoliui buvo priešingas. TiO_2 sluoksnių nusodinimas sukėlė mikrolęšių aukščio sumažėjimą ir židinio nuotolio padidėjimą. Tokie mikrooptinių elementų geometrijos pokyčiai atitinka tempiamųjų dangos įtempių sukeltas deformacijas. Tačiau po Al_2O_3 dangos nusodinimo mikrolęšių aukštis padidėjo, o židinio nuotolis sumažėjo. Šis efektas gali būti susijęs su pirmtako molekulių difuzija į porėtą hibridinio polimero paviršių, kuri gali nulemti dalinį tūrinį paviršinės polimero srities išsiplėtimą. Al_2O_3 auginimui buvo naudojamas trimetilaliuminio (TMA) pirmtakas, kurio molekulės yra sąlyginai mažos, todėl gali prasiskverbti į porėtų polimerinių medžiagų paviršių, taip sukeldamos paviršinio medžiagos sluoksnio pastorėjimą. Tetrakis(dimetilamino)titano junginio, kuris buvo naudojamas TiO_2 sluoksnio formavimui, molekulės yra žymiai didesnės ir dėl šios priežasties Ti pirmtako molekulių prasiskverbimas į polimero tūrį yra mažiau tikėtinas.

Toliau buvo sumodeliuotas AR dangos dizainas, skirtas SZ2080™ pagrindo atspindžio sumažinimui ties 633 nm bangos ilgiu. AR danga susidėjo iš 23 nm storio TiO_2 sluoksnio ir 131 nm storio Al_2O_3 sluoksnio. Po dangos suformavimo, santykinis mikrolęšių pralaidumas ties 633 nm padidėjo apytiksliai 3.7%. Panašus pralaidumo išaugimas (3.6%) buvo išmatuotas ir po AR dangos nusodinimo ant plokščių mikrostruktūrų. Be to, AR danga nesugadino mikrolęšių vaizdinimo kokybės. AR danga pasižymėjo sąlyginai mažais tempiamaisiais įtempiais (apie 127 MPa) ir ši danga neiškraipė mikrooptinių elementų geometrijos. Mikrolęšių profiliai prieš ir po skaidrinančios dangos nusodinimą yra pavaizduoti 2 pav. a dalyje. Po AR dangos nusodinimo 45 µm diametro mikrolęšių židinio nuotolis padidėjo nuo ≈ 182 µm iki ≈ 185 µm, o 95 µm diametro mikrolęšių židinio nuotolis pakito nuo ≈ 190 µm iki ≈ 196 µm. Židinio nuotolio padidėjimą galėjo nulemti tempiamieji dangos įtempiai, tačiau šių pokyčių vertės yra artimos matavimų paklaidoms. Suformuota AR danga taip pat sumažino mikrostruktūrų paviršiaus šiurkštumą nuo 3.4 nm iki 2.6 nm.



2 pav. (a) Skirtingo diametro mikrolęšių profiliai prieš ir po skaidrinančios dangos nusodinimą ir (b) daugiaukščių mikrostruktūrų pralaidumas ties 633 nm bangos ilgiu prieš ir po skaidrinančios dangos nusodinimą.

Pabaigai, buvo įvertinta galimybė suformuoti tolygią, paviršiaus formą atkartojančią AR dangą ant daugiaaukščių mikrooptinių komponentų naudojant ALD. Šiems eksperimentams buvo pagamintos trys skirtingo dizaino mikrostruktūros, susidedančios iš dviejų, keturių arba šešių optinių paviršių. Daugiaaukščių elementų atveju AR dangos yra kritiškai svarbios, nes didėjant paviršių skaičiui, atspindžiai nuo kiekvieno optinio paviršiaus akumuliuojasi ir bendras elemento pralaidumas mažėja. Atliktų mikrostruktūrų pralaidumo matavimų rezultatai yra pademonstruoti 2 pav. b dalyje. Matavimų metu buvo pastebėta, jog paviršių skaičiui padidėjus nuo dviejų iki šešių, pralaidumas 633 nm bangos ilgyje sumažėjo nuo maždaug 92% iki maždaug 77%. Po AR dangos nusodinimo buvo pasiektas visų paviršių praskaidrėjimas ir visų trijų tipų daugiaaukščių mikrostruktūrų pralaidumas siekė ne mažiau nei 98%.

Nanostruktūrizuotų dangų stabilizavimas

Antroje disertacijos dalyje buvo nagrinėjamas porėtų nanostruktūrizuotų dangų stabilumo kintančiose aplinkos sąlygose padidinimas. Šį skyrių sudaro du poskyriai, kuriuose pristatomi skirtingi metodai, taikyti siekiant sumažinti porėtų dangų jautrumą aplinkos poveikiui. Pirma, aptariamas nanostruktūrizuotų sluoksnių nusodinimas naudojant medžiagą, pasižyminčia mažesniu jautrumu drėgmei. Antra, pademonstruotas apsauginių sluoksnių formavimas naudojant atominių sluoksnių nusodinimo technologiją.

Anizotropinės LaF_3 dangos

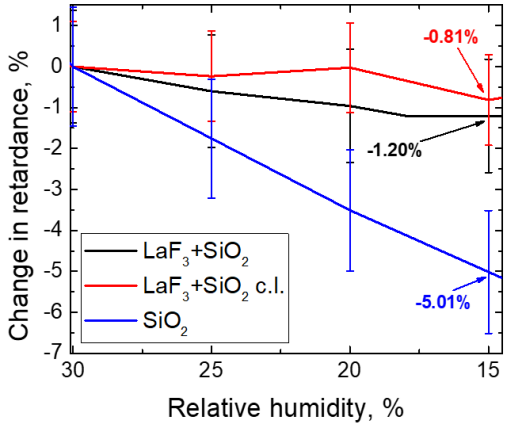
Šiame poskyryje yra aprašomas nanostruktūrizuotų anizotropinių dangų formavimas LaF_3 sluoksnių pagrindu. Pirma, buvo palygintos vienasluoksnės anizotropinės dangos, nusodintos naudojant garinimą elektronų pluoštu (EBE) ir terminį garinimą. Siekiant suformuoti dangą, pasižyminčią didele optine anizotropija ir mažais optiniais nuostoliais, LaF_3 sluoksniai buvo nusodinti 60°, 70° ir 80° kampais naudojant terminį garinimą ir 70° kampu naudojant EBE. Didžiausią dvejopalaužiškumą pavyko pasiekti nusodinant anizotropinius LaF_3 sluoksnius 70° kampu terminio garinimo metodu. Šie sluoksniai toliau buvo taikomi daugiasluoksnių anizotropinių dangų formavimui.

Paprasčiausias nanostruktūrizuotų fazinių plokštelių gamybos metodas yra reikiamo storio anizotropinio sluoksnio nusodinimas. Tačiau didėjant porėto anizotropinio sluoksnio storiui yra stebimas nanokolonų plėtimasis, kuris gali nulemti ženklius šviesos sklaidos nuostolius. Siekiant to išvengti neretai yra naudojamos daugiasluoksnės struktūros, kurias sudaro porėti anizotropiniai sluoksniai ir tankių izotropinių sluoksnių intarpai. Plonų tankių sluoksnių įterpimas sustabdo nanokolonų plėtimąsi ir leidžia pagaminti mažais optiniais nuostoliais pasižyminčias nanostruktūrizuotas fazines plokšteles. Norint išsiaiškinti optimalius parametrus LaF_3 daugiasluoksnių dangų nusodinimui, buvo atlikta serija eksperimentų. Analizuojant dangas, suformuotas tik iš LaF_3 sluoksnių, buvo pastebėta, kad šiose dangose tankūs intarpai nesusiformavo, o vyko nepertraukiamas koloninės mikrostruktūros augimas, kuris nulėmė didelius optinius nuostolius (> 15%) ties 266 nm. Ištisinių nanokolonų susidarymas gali būti susijęs su kristalinės LaF_3 struktūros formavimusi. Kadangi EBE proceso metu nusėda amorfiniai SiO_2 sluoksniai, ši medžiaga buvo pritaikyta tankių intarpų formavimui tarp anizotropinių LaF_3 sluoksnių daugiasluoksnėse dangose. Porėtų LaF_3 ir tankių SiO_2 sluoksnių kombinacija leido suformuoti dangą, pasižyminčią sąlyginai mažais optiniais nuostoliais (< 2%) 266 nm bangos ilgyje.

Parinkus optimalius daugiasluoksnių anizotropinių dangų nusodinimo parametrus, buvo suformuotos ketvirčio bangos ilgio fazinės plokštelės 266 nm bangos ilgiui. Palyginti trys skirtingi nanostruktūrizuotų fazinių plokštelių dizainai: i) vienasluoksnė LaF_3 fazinė plokštelė padengta tankiu apsauginiu SiO_2 sluoksniu (LaF_3+SiO_2 c.l.), ii) daugiasluoksnė fazinė plokštelė susidedanti iš porėtų anizotropinių LaF_3 sluoksnių ir tankių izotropinių SiO_2 intarpų (LaF_3+SiO_2), iii) daugiasluoksnė SiO_2 fazinė plokštelė, susidedanti iš anizotropinių ir izotropinių SiO_2 sluoksnių (SiO_2). Daugiasluoksnė LaF_3+SiO_2 fazinė plokštelė pasižymėjo mažiausiais optiniais

nuostoliais 266 nm bangos ilgyje (≈ 1%). Optiniai nuostoliai SiO_2 fazinėje plokštelėje siekė maždaug 2%, didžiausi optiniai nuostoliai buvo nustatyti vienasluoksnei LaF_3+SiO_2 c.l. fazinei plokštelei (> 3%). Nors daugiasluoksnė LaF_3 fazinė plokštelė užtikrino silpniausius nuostolius, išmatuota LIDT vertė naudojant 1-į-1 matavimo protokolą ties 266 nm buvo mažesnė nei 3 J cm^{-2}. Didžiausias atsparumas lazerinei spinduliuotei buvo pasiektas naudojant vienasluoksnės LaF_3 plokštelės dizainą (≈ 15 J cm^{-2}).

Nanostruktūrizuotų fazinių plokštelių stabilumas buvo įvertintas kintančios drėgmės aplinkoje naudojant skirtuminio fazės vėlinimo vaizdinimą. Skirtingo dizaino fazinių plokštelių skirtuminio fazės vėlinimo pokytis mažinant santykinę aplinkos drėgmę yra parodytas 3 pav.



3 pav. Vienasluoksnių LaF_3+SiO_2 c.l., daugiasluoksnių LaF_3+SiO_2, ir SiO_2 fazinių plokštelių skirtuminio fazės vėlinimo pokyčio priklausomybė nuo santykinės drėgmės.

Porėtų LaF_3 pagrindu pagamintos fazinės plokštelės reikšmingai sumažino aplinkos poveikį porėtų dangų optinėms charakteristikoms. Nustatytas skirtuminio fazės vėlinimo pokytis sumažinus santykinę aplinkos drėgmę vienasluoknių LaF_3 fazinių plokštelių atveju buvo 0.8%, o daugiasluoksnių LaF_3+SiO_2 dangų atveju siekė 1.2%. Toks skirtuminio fazės vėlinimo sumažėjimas keičiant aplinkos drėgmę yra žymiai mažesnis lyginant su 5% pokyčiu nustatytu SiO_2 fazinėms plokštelėms.

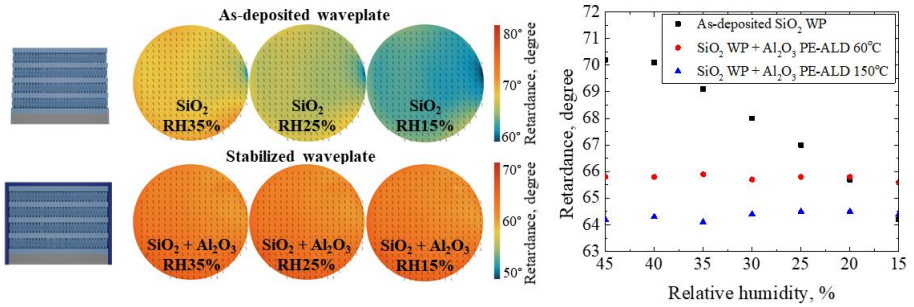
SiO_2 fazinių plokštelių apsaugojimas

Paskutinėje disertacijos dalyje buvo analizuojamas ALD pritaikymas plonų apsauginių sluoksnių formavimui ant porėtų nanostruktūrizuotų SiO_2 dangų. Kadangi pagrindinis šių eksperimentų tikslas buvo stabilizuoti nanostruktūrizuotas UV fazines plokšteles, potencialiai skirtas didelės galios

lazerinėms sistemoms, apsauginiams sluoksniams yra išskiriami papildomi reikalavimai. Šie sluoksniai turi būti ne tik tankūs ir su minimaliu defektų kiekiu, bet nemažiau svarbu yra užtikrinti, jog apsauginiai sluoksniai nepadidintų nanostruktūrizuotų dangų sugerties bei nesumažintų LIDT. Be to, porėtų nanostruktūrizuotų dangų mechaninis neatsparumas nulemia mažais įtempiais pasižyminčių apsauginių sluoksnių poreikį.

Pradžioje buvo nustatyti plonų ≈ 150 nm storio Al_2O_3 sluoksnių optiniai ir fiziniai parametrai. Vienasluoksnės Al_2O_3 dangos buvo nusodinamos žemoje (60 °C) ir aukštesnėje (150 °C) temperatūroje taikant terminį ir plazminį ALD (PE-ALD) procesą. Mažiausiu lūžio rodikliu ir mažiausiais optiniais nuostoliais pasižymėjo Al_2O_3 dangos suformuotos 60 °C temperatūroje naudojant terminį ALD, o aukštesnė 150 °C nusodinimo temperatūra leido suformuoti ženkliai tankesnius, didesnio lūžio rodiklio sluoksnius. Didžiausio lūžio rodiklio Al_2O_3 sluoksniai buvo gauti naudojant aukštesnės temperatūros plazminį procesą, tačiau šiuo atveju buvo pastebėti žymiai didesni optiniai nuostoliai ties 355 nm, kurių vertė buvo apytiksliai 4 eilėmis didesnė nei Al_2O_3 dangų nusodintų naudojant terminį ALD. Išmatavus Al_2O_3 sluoksnių sugertį 355 nm bangos ilgyje, galima spręsti, kad sugertis yra pagrindinis nuostolių šaltinis UV spektrinėje srityje.

Al_2O_3 dangos, suformuotos naudojant terminį ALD procesą, pasižymėjo sąlyginai dideliais įtempiais, kurių vertės viršijo 300 MPa. Tokiomis pačiomis sąlygomis ant porėtų anizotropinių dangų nusodinti Al_2O_3 sluoksniai sukėlė šių dangų įtrūkimus. Plazminio proceso atveju Al_2O_3 sluoksnių įtempiai buvo ženkliai mažesni ir nesiekė 200 MPa. Nusodinant apsauginius Al_2O_3 sluoksnius PE-ALD metodu, buvo užtikrinti pakankamai maži įtempiai, kurie nepažeidė porėtų anizotropinių SiO_2 dangų. Įvertinus anizotropinių dangų skirtuminio fazės vėlinimo kitimą laike buvo nustatyta, kad apsauginių sluoksnių nusodinimas nesustabdė skirtuminio fazės vėlinimo didėjimo, kuris gali būti siejamas su lėtu drėgmės prasiskverbimu į porėtą struktūrą. Tačiau po pradinio nusistovėjimo atlikus trumpalaikio stabilumo testavimus kintančios drėgmės sąlygomis nustatyta, kad apsauginiai Al_2O_3 sluoksniai, suformuoti taikant PE-ALD, stabilizavo nanostruktūrizuotų SiO_2 dangų skirtuminį fazės vėlinimą. Fazės vėlinimo skirtumo kitimas mažinant santykinę aplinkos drėgmę prieš ir po apsauginių sluoksnių nusodinimą pavaizduotas 4 pav.



4 pav. Nanostruktūrizuotų SiO_2 fazinių plokštelių skirtuminio fazės vėlinimo žemėlapiai esant skirtingai santykinei drėgmei (RH) ir skirtuminio fazės vėlinimo priklausomybė nuo santykinės drėgmės prieš apsauginių Al_2O_3 sluoksnių nusodinimą ir po jo.

Kadangi Al_2O_3 sluoksniai, nusodinti naudojant PE-ALD, nesukėlė mechaninių pažeidimų nanostruktūrizuotose dangose, šie sluoksniai buvo pritaikyti nanostruktūrizuotų ketvirčio bangos ilgio fazinių plokštelių apsaugojimui. Taikant 1-į-1 matavimo protokolą, SiO_2 fazinių plokštelių LIDT ties 355 nm siekė 18.6 J cm^{-2} ir 18.6 J cm^{-2}, atitinkamai išilgai greitosios ir lėtosios ašies. Tačiau apsauginių sluoksnių suformavimas 60 °C temperatūroje naudojant PE-ALD procesą, nulėmė LIDT sumažėjimą iki 1.8 J cm^{-2} (greitajai ašiai) ir 5.3 J cm^{-2} (lėtajai ašiai). Dar prastesnis lazerinis atsparumas buvo nustatytas po Al_2O_3 sluoksnių nusodinimo aukštesnėje 150 °C temperatūroje, po kurio LIDT vertė nukrito iki 1.7 J cm^{-2}. Nanostruktūrizuotų SiO_2 LIDT sumažėjimas po apsauginių sluoksnių nusodinimo gali būti susijęs su didele UV sugertimi Al_2O_3 sluoksniuose, suformuotuose naudojant PE-ALD procesą.

Šiame darbe buvo pademonstruotas lokalaus lazerinio atkaitinimo potencialas siekiant padidinti apsaugotų SiO_2 plokštelių atsparumą lazerinei spinduliuotei. Eksperimentų metu lazerinės energijos įtėkis buvo lėtai didinamas, kol buvo užfiksuota lazerine spinduliuote inicijuota pažaida. Vidutinis įtėkio didinimo žingsnis siekė maždaug 0.4–0.5 J cm^{-2} vienam impulsui. Taikant šią matavimų metodiką, po Al_2O_3 sluoksnių nusodinimo 60 °C ir 150 °C temperatūroje nanostruktūrizuotų fazinių plokštelių lazerinė pažaida buvo pastebėta pasiekus apytiksliai 35 J cm^{-2} ir 22 J cm^{-2} energijos įtėkio vertes, atitinkamai.

Išvados

1. Tolygūs Al_2O_3 sluoksniai, suformuoti naudojant atominių sluoksnių nusodinimą, leido užlyginti neorganinių mikrolęšių, pagamintų iš lydyto kvarco, CaF_2, BaF_2 ir safyro, paviršių užpildydami tarpus tarp paviršiaus nelygumų. Šiurkštumo sumažėjimas daugiausia priklauso nuo atstumų tarp paviršiaus nelygumų. Ploni Al_2O_3 sluoksniai sumažino tirtų mikrooptinių komponentų paviršiaus šiurkštumą nepakeisdami jų geometrijos.
2. Mažais įtempiais (127 MPa) pasižyminčios skaidrinančios dangos, suformuotos naudojant atominių sluoksnių nusodinimą, sumažino hibridinio polimero 3D mikrooptinių elementų atspindžių nuostolius neiškraipydamos jų formos ir vaizdinimo kokybės. Po skaidrinančios dangos nusodinimo, daugiaaukščių mikrostruktūrų, kurias sudaro šeši paviršiai, pralaidumas padidėjo nuo ≈ 77% iki ≈ 98%.
3. Kintančios drėgmės sąlygomis daugiasluoksnių ir vienasluoksnių LaF_3 dangų pagrindu suformuotų fazinių plokštelių skirtuminio fazės vėlinimo svyravimai sumažėjo iki 1.2% ir 0.8%, lyginant su 5% pokyčiu SiO_2 fazinių plokštelių atveju. Porėtų anizotropinių LaF_3 ir tankių izotropinių SiO_2 sluoksnių kombinacija leido suformuoti daugiasluoksnes plokšteles, pasižyminčias žymiai mažesniais optiniais nuostoliais (1.1%), lyginant su vienasluoksnėmis LaF_3 fazinėmis plokštelėmis (> 3%).
4. Apsauginiai sluoksniai, suformuoti naudojant plazminį atominių sluoksnių nusodinimą, po pradinio nusistovėjimo stabilizavo nanostruktūrizuotų SiO_2 fazinių plokštelių skirtuminį fazės vėlinimą kintančios drėgmės sąlygomis. Po apsauginių sluoksnių suformavimo, fazinių plokštelių lazerine spinduliuote sukeltos pažaidos slenkstis sumažėjo nuo ≈ 18 J cm^{-2} iki mažiau nei 5 J cm^{-2}. Lokalus lazerinės spinduliuotės atkaitinimas lėtai keliant energijos įtėkį padidino fazinių plokštelių atsparumą pažaidai iki 35 J cm^{-2} ir 22 J cm^{-2} po Al_2O_3 apsauginių sluoksnių nusodinimo 60 °C ir 150 °C temperatūroje, atitinkamai.

BIBLIOGRAPHY

1. A. Ostendorf, A. Neumeister, S. Dudziak, S. Passinger, and J. Stampfl, "Micro- and nano-parts generated by laser-based solid freeform fabrication," in *Advances in Laser Materials Processing* (Elsevier, 2010), pp. 695–734.
2. T. Gissibl, S. Thiele, A. Herkommer, and H. Giessen, "Two-photon direct laser writing of ultracompact multi-lens objectives," Nature Photon **10**, 554–560 (2016).
3. S. Thiele, K. Arzenbacher, T. Gissibl, H. Giessen, and A. M. Herkommer, "3D-printed eagle eye: Compound microlens system for foveated imaging," Sci. Adv. **3**, e1602655 (2017).
4. J. H. Campbell, R. A. Hawley-Fedder, C. J. Stolz, J. A. Menapace, M. R. Borden, P. K. Whitman, J. Yu, M. J. Runkel, M. O. Riley, M. D. Feit, and R. P. Hackel, "NIF optical materials and fabrication technologies: an overview," in Optical Engineering at the Lawrence Livermore National Laboratory II: The National Ignition Facility, Proc. SPIE 5341, p. 84 (2004).
5. M. Bass, ed., "Handbook of optics. 1: Fundamentals, techniques, and design," in 2. ed (McGraw-Hill, 1995).
6. H. E. Bennett, "Scattering Characteristics Of Optical Materials," Optical Engineering **17**(5), 175480 (1978).
7. S. Ristok, P. Flad, and H. Giessen, "Atomic layer deposition of conformal anti-reflective coatings on complex 3D printed micro-optical systems," Opt. Mater. Express **12**, 2063 (2022).
8. D. Wernham and A. Piegari, "Optical coatings in the space environment," in *Optical Thin Films and Coatings* (Elsevier, 2018), pp. 789–811.
9. S. Bertet, T. Quelo, C. Boscher, E. Lavastre, S. MacNally, D. Sadowski, C. Marcel, M. Mireles, B. Gallas, and M. Chorel, "Effect of dimethyl phthalate contamination on all-silica GLAD quarter-wave plate performances," Appl. Opt. **65**, A164 (2026).
10. D. Gonzalez-Hernandez, S. Varapnickas, A. Bertoncini, C. Liberale, and M. Malinauskas, "Micro-Optics 3D Printed via Multi-Photon Laser Lithography," Advanced Optical Materials **11**, 2201701 (2023).
11. T. Gissibl, S. Thiele, A. Herkommer, and H. Giessen, "Sub-micrometre accurate free-form optics by three-dimensional printing on single-mode fibres," Nat Commun **7**, 11763 (2016).
12. A. C. Jones and M. L. Hitchman, eds., *Chemical Vapour Deposition: Precursors, Processes and Applications* (Royal Society of Chemistry, 2008).
13. K. Pfeiffer, L. Ghazaryan, U. Schulz, and A. Szeghalmi, "Wide-Angle Broadband Antireflection Coatings Prepared by Atomic Layer Deposition," ACS Appl. Mater. Interfaces **11**, 21887–21894 (2019).

14. K. Pfeiffer, U. Schulz, A. Tünnermann, and A. Szeghalmi, "Antireflection Coatings for Strongly Curved Glass Lenses by Atomic Layer Deposition," Coatings **7**, 118 (2017).
15. I. Rana, S. Mahadevan, M. Delamer, and C. Longworth, "Star grazing with alumina grass: antireflection coatings in the visible and near-infrared on IPX-clear microlenses assisted by grass-like alumina," in *Advanced Fabrication Technologies for Micro/Nano Optics and Photonics XIX*, G. Von Freymann, E. Blasco, D. Chanda, and C. Moser, eds. (SPIE, 2026), p. 47.
16. Y.-T. Yang, Q.-Y. Cai, D.-Q. Liu, L.-S. Gao, H.-T. Zhang, L. Peng, E.-T. Hu, B.-J. Liu, H.-H. Luo, R.-J. Zhang, and Y.-X. Zheng, "Low polarization-sensitive ultra-broadband anti-reflection coatings with improved reliability," Opt. Express **31**, 25477 (2023).
17. A. Wickberg, A. Abass, H. Hsiao, C. Rockstuhl, and M. Wegener, "Second-Harmonic Generation by 3D Laminate Metacrystals," Advanced Optical Materials **7**, 1801235 (2019).
18. D. Gonzalez-Hernandez, B. Sanchez-Padilla, D. Gailevičius, S. C. Thodika, S. Juodkazis, E. Brasselet, and M. Malinauskas, "Single-Step 3D Printing of Micro-Optics with Adjustable Refractive Index by Ultrafast Laser Nanolithography," Advanced Optical Materials **11**, 2300258 (2023).
19. H. Mu, D. Smith, T. Katkus, N. H. A. Le, D. Stonyte, D. Gailevičius, D. Kapsaskis, A. D. Frate, T. S. Bedi, D. Narbutis, V. Anand, D. Astrauskyte, L. Grineviciute, S. H. Ng, K. Glazebrook, J. Lawrence, and S. Juodkazis, "3D free-form optical lens — miniaturised fibre couplers for astrophotonics," Optics & Laser Technology **190**, 112960 (2025).
20. F. M. Cunha, J. R. Freitas, S. Pimenta, M. F. Silva, and J. H. Correia, "Silicon dioxide atomic layer deposition at low temperature for PDMS microlenses coating," Optical Materials **157**, 116167 (2024).
21. S. Thiele, C. Pruss, A. M. Herkommer, and H. Giessen, "3D printed stacked diffractive microlenses," Opt. Express **27**, 35621 (2019).
22. S. Varapnickas, S. Chandran Thodika, F. Moroté, S. Juodkazis, M. Malinauskas, and E. Brasselet, "Birefringent optical retarders from laser 3D-printed dielectric metasurfaces," Applied Physics Letters **118**, 151104 (2021).
23. A. Ovsianikov, J. Viertl, B. Chichkov, M. Oubaha, B. MacCraith, I. Sakellari, A. Giakoumaki, D. Gray, M. Vamvakaki, M. Farsari, and C. Fotakis, "Ultra-Low Shrinkage Hybrid Photosensitive Material for Two-Photon Polymerization Microfabrication," ACS Nano **2**, 2257–2262 (2008).
24. J.-M. Kwon, Y. Kwon, Y.-G. Cha, D. H. Han, H.-K. Kim, J.-K. Park, M. H. Kim, and K.-H. Jeong, "Biologically inspired microlens array camera for high-resolution wide field-of-view imaging," Nat Commun **17**, 4343 (2026).

25. M. Ares, S. Royo, and J. Caum, "Shack-Hartmann sensor based on a cylindrical microlens array," Opt. Lett. **32**, 769 (2007).
26. M. M. Hawkeye, M. T. Taschuk, and M. J. Brett, *Glancing Angle Deposition of Thin Films: Engineering the Nanoscale*, 1st ed. (Wiley, 2014).
27. L. Grineviciute, C. Babayigit, D. Gailevičius, M. Peckus, M. Turduev, T. Tolenis, M. Vengris, H. Kurt, and K. Staliunas, "Nanostructured Multilayer Coatings for Spatial Filtering," Advanced Optical Materials **9**, 2001730 (2021).
28. J. C. Ginn, I. Brener, D. W. Peters, J. R. Wendt, J. O. Stevens, P. F. Hines, L. I. Basilio, L. K. Warne, J. F. Ihlefeld, P. G. Clem, and M. B. Sinclair, "Realizing Optical Magnetism from Dielectric Metamaterials," Phys. Rev. Lett. **108**, 097402 (2012).
29. M. Mireles, B. N. Hoffman, S. MacNally, C. C. Smith, S. N. Lakshmanan, J. C. Lambropoulos, A. L. Rigatti, and S. G. Demos, "Direct-write laser-assisted patterning of form birefringence in wave plates fabricated by glancing-angle deposition," Optica **10**, 657 (2023).
30. M. Faustini, L. Nicole, C. Boissière, P. Innocenzi, C. Sanchez, and D. Grosso, "Hydrophobic, Antireflective, Self-Cleaning, and Antifogging Sol−Gel Coatings: An Example of Multifunctional Nanostructured Materials for Photovoltaic Cells," Chem. Mater. **22**, 4406–4413 (2010).
31. L. Grinevičiūtė, M. Andrulevičius, A. Melninkaitis, R. Buzelis, A. Selskis, A. Lazauskas, and T. Tolenis, "Highly Resistant Zero-Order Waveplates Based on All-Silica Multilayer Coatings," Physica Status Solidi (a) **214**, 1700764 (2017).
32. T. Tolenis, L. Grinevičiūtė, R. Buzelis, L. Smalakys, E. Pupka, S. Melnikas, A. Selskis, R. Drazdys, and A. Melninkaitis, "Sculptured anti-reflection coatings for high power lasers," Opt. Mater. Express **7**, 1249 (2017).
33. T. Tolenis, L. Grinevičiūtė, L. Smalakys, M. Ščiuka, R. Drazdys, L. Mažulė, R. Buzelis, and A. Melninkaitis, "Next generation highly resistant mirrors featuring all-silica layers," Sci Rep **7**, 10898 (2017).
34. L. Grineviciute, L. Ramalis, R. Buzelis, and T. Tolenis, "Highly resistant all-silica polarizing coatings for normal incidence applications," Opt. Lett. **46**, 916 (2021).
35. S. R. Kennedy, M. J. Brett, H. Miguez, O. Toader, and S. John, "Optical properties of a three-dimensional silicon square spiral photonic crystal," Photonics and Nanostructures - Fundamentals and Applications **1**, 37–42 (2003).
36. S. Kumar and D. K. Aswal, eds., *Recent Advances in Thin Films*, Materials Horizons: From Nature to Nanomaterials (Springer Singapore, 2020).
37. Y. Lin and X. Chen, *Advanced Nano Deposition Methods* (Wiley-VCH Verlag GmbH & Co. KGaA Chemical Industry Press, 2016).

38. L. Grinevičiūtė, "Nanostructured optical coatings for the manipulation of laser radiation," doctoral dissertation, Vilnius University (2021).
39. M.-C. Liu, B.-H. Liao, W.-H. Cho, C.-C. Lee, and C.-C. Jaing, "The research of oblique deposition of lanthanum fluoride thin films at 193nm," in Nanoengineering: Fabrication, Properties, Optics, and Devices IV, Proc. SPIE 6645, 66451Y E. (2007).
40. J. M. LaForge, M. T. Taschuk, and M. J. Brett, "Glancing angle deposition of crystalline zinc oxide nanorods," Thin Solid Films **519**, 3530–3537 (2011).
41. A. Wolcott, W. A. Smith, T. R. Kuykendall, Y. Zhao, and J. Z. Zhang, "Photoelectrochemical Study of Nanostructured ZnO Thin Films for Hydrogen Generation from Water Splitting," Adv Funct Materials **19**, 1849–1856 (2009).
42. A. C. Van Popta, J. C. Sit, and M. J. Brett, "Optical Properties of Porous Helical Thin Films," Appl. Opt. **43**, 3632 (2004).
43. S. Bertet, M. Mireles, S. MacNally, M. Chorel, É. Lavastre, D. Sadowski, C. Marcel, and B. Gallas, "All-alumina quarter-wave plate coatings fabricated by glancing angle deposition using serial bideposition," Applied Surface Science **710**, 163957 (2025).
44. S. MacNally, C. Smith, J. Spaulding, J. Foster, and J. B. Oliver, "Glancing-angle-deposited silica films for ultraviolet wave plates," Appl. Opt. **59**, A155 (2020).
45. C. Charles, N. Martin, and M. Devel, "Optical properties of nanostructured WO_3 thin films by GLancing Angle Deposition: Comparison between experiment and simulation," Surface and Coatings Technology **276**, 136–140 (2015).
46. I. Hodgkinson and Q. H. Wu, "Serial bideposition of anisotropic thin films with enhanced linear birefringence," Appl. Opt. **38**, 3621 (1999).
47. T. Suntola and J. Antson, "Method for producing compound thin films," U.S. patent US4058430 (1977).
48. D.-G. Park, H.-J. Cho, K.-Y. Lim, C. Lim, I.-S. Yeo, J.-S. Roh, and J. W. Park, "Characteristics of n+ polycrystalline-Si/Al_2O_3/Si metal–oxide–semiconductor structures prepared by atomic layer chemical vapor deposition using $Al(CH_3)_3$ and H_2O vapor," Journal of Applied Physics **89**, 6275–6280 (2001).
49. M. Leskelä and M. Ritala, "Atomic Layer Deposition Chemistry: Recent Developments and Future Challenges," Angew Chem Int Ed **42**, 5548–5554 (2003).
50. D. Riihelä, M. Ritala, R. Matero, and M. Leskelä, "Introducing atomic layer epitaxy for the deposition of optical thin films," Thin Solid Films **289**, 250–255 (1996).
51. H. Kumagai, K. Toyoda, K. Kobayashi, M. Obara, and Y. Iimura, "Titanium oxide/aluminum oxide multilayer reflectors for “water-window” wavelengths," Applied Physics Letters **70**, 2338–2340 (1997).

52. M. Králik, "Adsorption, chemisorption, and catalysis," Chemical Papers **68**, (2014).
53. H. Liu, P. Ma, Y. Pu, and Z. Zhao, "Atomic layer deposition of Al_2O_3 and HfO_2 for high power laser application," Journal of Alloys and Compounds **859**, 157751 (2021).
54. M. Leskelä and M. Ritala, "Atomic layer deposition (ALD): from precursors to thin film structures," Thin Solid Films **409**, 138–146 (2002).
55. N. T. Gabriel, "High-power and high-aspect-ratio optical coatings by atomic layer deposition," University of Minnesota (2011).
56. S. M. George, "Atomic Layer Deposition: An Overview," Chem. Rev. **110**, 111–131 (2010).
57. V. Cremers, R. L. Puurunen, and J. Dendooven, "Conformality in atomic layer deposition: Current status overview of analysis and modelling," Applied Physics Reviews **6**, 021302 (2019).
58. R. A. Wind and S. M. George, "Quartz Crystal Microbalance Studies of Al_2O_3 Atomic Layer Deposition Using Trimethylaluminum and Water at 125 °C," J. Phys. Chem. A **114**, 1281–1289 (2010).
59. M. N. Rocklein and S. M. George, "Temperature-Induced Apparent Mass Changes Observed during Quartz Crystal Microbalance Measurements of Atomic Layer Deposition," Anal. Chem. **75**, 4975–4982 (2003).
60. M. Leskelä and M. Ritala, "ALD precursor chemistry : Evolution and future challenges," J. Phys. IV France **09**, Pr8-837-Pr8-852 (1999).
61. M. L. O'Neill, H. R. Bowen, A. Derecskei-Kovacs, K. S. Cuthill, B. Han, and M. Xiao, "Impact of Aminosilane Precursor Structure on Silicon Oxides by Atomic Layer Deposition," Interface magazine **20**, 33–37 (2011).
62. H. H. Lemago, S. C. Arwen, D. Hessz, G. Jágerszki, P. Pál, C. Cserháti, E. M. Baradács, T. Fodor, Z. Erdélyi, and I. M. Szilágyi, "Thermal and plasma-enhanced ALD for the synthesis of inverse opal Al_2O_3 and its composite materials," Vacuum **238**, 114254 (2025).
63. X. Liu, S. Ramanathan, A. Longdergan, A. Srivastava, E. Lee, T. E. Seidel, J. T. Barton, D. Pang, and R. G. Gordon, "ALD of Hafnium Oxide Thin Films from Tetrakis(ethylmethylamino)hafnium and Ozone," J. Electrochem. Soc. **152**, G213 (2005).
64. Y.-S. Lee, D. Choi, B. Shong, S. Oh, and J.-S. Park, "Low temperature atomic layer deposition of SiO_2 thin films using di-isopropylaminosilane and ozone," Ceramics International **43**, 2095–2099 (2017).
65. Y.-C. Cheng, H.-C. Wang, S.-W. Feng, T.-P. Li, S.-K. Fung, K.-Y. Yuan, and M.-J. Chen, "Co-dosing Ozone and Deionized Water as Oxidant Precursors of ZnO Thin Film Growth by Atomic Layer Deposition," Nanoscale Res Lett **15**, 154 (2020).
66. H. B. Profijt, S. E. Potts, M. C. M. Van De Sanden, and W. M. M. Kessels, "Plasma-Assisted Atomic Layer Deposition: Basics, Opportunities, and Challenges," Journal of Vacuum Science & Technology A: Vacuum, Surfaces, and Films **29**, 050801 (2011).

67. S. B. S. Heil, F. Roozeboom, M. C. M. Van De Sanden, and W. M. M. Kessels, "Plasma-assisted atomic layer deposition of Ta_2O_5 from alkylamide precursor and remote O_2 plasma," Journal of Vacuum Science & Technology A: Vacuum, Surfaces, and Films **26**, 472–480 (2008).
68. M. Hirayama and S. Sugawa, "Low-energy high-flux ion bombardment-induced interfacial mixing during Al_2O_3 plasma-enhanced atomic layer deposition," Journal of Vacuum Science & Technology A: Vacuum, Surfaces, and Films **38**, 052407 (2020).
69. C. Vallée, M. Bonvalot, S. Belahcen, T. Yeghoyan, M. Jaffal, R. Vallat, A. Chaker, G. Lefèvre, S. David, A. Bsiesy, N. Possémé, R. Gassilloud, and A. Granier, "Plasma deposition—Impact of ions in plasma enhanced chemical vapor deposition, plasma enhanced atomic layer deposition, and applications to area selective deposition," Journal of Vacuum Science & Technology A: Vacuum, Surfaces, and Films **38**, 033007 (2020).
70. J. Kim, S. Kim, H. Jeon, M.-H. Cho, K.-B. Chung, and C. Bae, "Characteristics of HfO_2 thin films grown by plasma atomic layer deposition," Applied Physics Letters **87**, 053108 (2005).
71. E. O. Filatova and A. S. Konashuk, "Interpretation of the Changing the Band Gap of Al_2O_3 Depending on Its Crystalline Form: Connection with Different Local Symmetries," J. Phys. Chem. C **119**, 20755–20761 (2015).
72. V. Miikkulainen, M. Leskelä, M. Ritala, and R. L. Puurunen, "Crystallinity of inorganic films grown by atomic layer deposition: Overview and general trends," Journal of Applied Physics **113**, 021301 (2013).
73. J. W. Elam, M. Schuisky, J. D. Ferguson, and S. M. George, "Surface chemistry and film growth during TiN atomic layer deposition using TDMAT and NH_3," Thin Solid Films **436**, 145–156 (2003).
74. Q. Xie, Y.-L. Jiang, C. Detavernier, D. Deduytsche, R. L. Van Meirhaeghe, G.-P. Ru, B.-Z. Li, and X.-P. Qu, "Atomic layer deposition of TiO_2 from tetrakis-dimethyl-amido titanium or Ti isopropoxide precursors and H_2O," Journal of Applied Physics **102**, 083521 (2007).
75. P. Poodt, D. C. Cameron, E. Dickey, S. M. George, V. Kuznetsov, G. N. Parsons, F. Roozeboom, G. Sundaram, and A. Vermeer, "Spatial atomic layer deposition: A route towards further industrialization of atomic layer deposition," Journal of Vacuum Science & Technology A: Vacuum, Surfaces, and Films **30**, 010802 (2012).
76. D. M. Fryauf, A. C. Phillips, M. J. Bolte, A. Feldman, G. S. Tompa, and N. P. Kobayashi, "Scaling Atomic Layer Deposition to Astronomical Optic Sizes: Low-Temperature Aluminum Oxide in a Meter-Sized Chamber," ACS Appl. Mater. Interfaces **10**, 41678–41689 (2018).
77. H. Qi, M. Zhu, M. Fang, S. Shao, C. Wei, K. Yi, and J. Shao, "Development of high-power laser coatings," High Pow Laser Sci Eng **1**, 36–43 (2013).

78. O. Stenzel, *Optical Coatings: Material Aspects in Theory and Practice*, Springer Series in Surface Sciences (Springer Berlin Heidelberg, 2014), Vol. 54.
79. D. M. Mattox, "Particle bombardment effects on thin-film deposition: A review," Journal of Vacuum Science & Technology A: Vacuum, Surfaces, and Films **7**, 1105–1114 (1989).
80. J. L. Van Hemmen, S. B. S. Heil, J. H. Klootwijk, F. Roozeboom, C. J. Hodson, M. C. M. Van De Sanden, and W. M. M. Kessels, "Plasma and Thermal ALD of Al_2O_3 in a Commercial 200 mm ALD Reactor," J. Electrochem. Soc. **154**, G165 (2007).
81. J. B. Oliver and D. Talbot, "Optimization of deposition uniformity for large-aperture National Ignition Facility substrates in a planetary rotation system," Appl. Opt. **45**, 3097 (2006).
82. G. N. Strauss, "Mechanical Stress in Optical Coatings," in *Optical Interference Coatings*, N. Kaiser and H. K. Pulker, eds., Springer Series in Optical Sciences (Springer Berlin Heidelberg, 2003), Vol. 88, pp. 207–229.
83. C. Coupeau, "Atomic force microscopy study of the morphological shape of thin film buckling," Thin Solid Films **406**, 190–194 (2002).
84. M. George, C. Coupeau, J. Colin, and J. Grilhé, "Mechanical behaviour of metallic thin films on polymeric substrates and the effect of ion beam assistance on crack propagation," Acta Materialia **53**, 411–417 (2005).
85. O. M. E. Ylivaara, X. Liu, L. Kilpi, J. Lyytinen, D. Schneider, M. Laitinen, J. Julin, S. Ali, S. Sintonen, M. Berdova, E. Haimi, T. Sajavaara, H. Ronkainen, H. Lipsanen, J. Koskinen, S.-P. Hannula, and R. L. Puurunen, "Aluminum oxide from trimethylaluminum and water by atomic layer deposition: The temperature dependence of residual stress, elastic modulus, hardness and adhesion," Thin Solid Films **552**, 124–135 (2014).
86. S. Shestaeva, A. Bingel, P. Munzert, L. Ghazaryan, C. Patzig, A. Tünnermann, and A. Szeghalmi, "Mechanical, structural, and optical properties of PEALD metallic oxides for optical applications," Appl. Opt. **56**, C47 (2017).
87. H. B. Profijt, M. C. M. Van De Sanden, and W. M. M. Kessels, "Substrate-biasing during plasma-assisted atomic layer deposition to tailor metal-oxide thin film growth," Journal of Vacuum Science & Technology A: Vacuum, Surfaces, and Films **31**, 01A106 (2013).
88. S. Kumar, Z. Tong, and X. Jiang, "Advances in the design and manufacturing of novel freeform optics," Int. J. Extrem. Manuf. **4**, 032004 (2022).
89. J. E. DeGroote, H. J. Romanofsky, I. A. Kozhinova, J. M. Schoen, and S. D. Jacobs, "Polishing PMMA and other optical polymers with magnetorheological finishing," in Optical Manufacturing and Testing V, Proc. SPIE 5180, p. 123 (2004).

90. T. J. Myers, J. A. Throckmorton, R. A. Borrelli, M. O'Sullivan, T. Hatwar, and S. M. George, "Smoothing surface roughness using Al_2O_3 atomic layer deposition," Applied Surface Science **569**, 150878 (2021).
91. W. S. Lau, L. Du, D. Q. Yu, X. Wang, H. Wong, and Y. Xu, "The Application of a Selective Etch to Conclusively Show the Surface Smoothing Effect of an Amorphous Thin Film Deposited by Atomic Layer Deposition," ECS J. Solid State Sci. Technol. **6**, N111–N116 (2017).
92. J. W. Elam, Z. A. Sechrist, and S. M. George, "ZnO/Al_2O_3 nanolaminates fabricated by atomic layer deposition: growth and surface roughness measurements," Thin Solid Films **414**, 43–55 (2002).
93. W. S. Lau, J. Zhang, X. Wan, J. K. Luo, Y. Xu, and H. Wong, "Surface smoothing effect of an amorphous thin film deposited by atomic layer deposition on a surface with nano-sized roughness," AIP Advances **4**, 027120 (2014).
94. S. H. Gerritsen, N. J. Chittock, V. Vandalon, M. A. Verheijen, H. C. M. Knoops, W. M. M. Kessels, and A. J. M. Mackus, "Surface Smoothing by Atomic Layer Deposition and Etching for the Fabrication of Nanodevices," ACS Appl. Nano Mater. **5**, 18116–18126 (2022).
95. C. Kauppinen, K. Isakov, and M. Sopanen, "Grass-like Alumina with Low Refractive Index for Scalable, Broadband, Omnidirectional Antireflection Coatings on Glass Using Atomic Layer Deposition," ACS Appl. Mater. Interfaces **9**, 15038–15043 (2017).
96. L. Ghazaryan, Y. Sekman, S. Schröder, C. Mühlig, I. Stevanovic, R. Botha, M. Aghaee, M. Creatore, A. Tünnermann, and A. Szeghalmi, "On the Properties of Nanoporous SiO_2 Films for Single Layer Antireflection Coating," Adv Eng Mater **21**, 1801229 (2019).
97. L. Ghazaryan, E.-B. Kley, A. Tünnermann, and A. Szeghalmi, "Nanoporous SiO_2 thin films made by atomic layer deposition and atomic etching," Nanotechnology **27**, 255603 (2016).
98. J. A. Dobrowolski, D. Poitras, P. Ma, H. Vakil, and M. Acree, "Toward perfect antireflection coatings: numerical investigation," Appl. Opt. **41**, 3075 (2002).
99. Y. Wei, H. Liu, O. Sheng, Z. Liu, S. Chen, and L. Yang, "Laser damage properties of TiO_2/Al_2O_3 thin films grown by atomic layer deposition," Appl. Opt. **50**, 4720 (2011).
100. C. J. Stolz, J. R. Taylor, W. K. Eickelberg, and J. D. Lindh, "Effects of vacuum exposure on stress and spectral shift of high reflective coatings," Appl. Opt. **32**, 5666 (1993).
101. D. Grosso, C. Boissière, and C. Sanchez, "Ultralow-dielectric-constant optical thin films built from magnesium oxyfluoride vesicle-like hollow nanoparticles," Nature Mater **6**, 572–575 (2007).
102. S. S. Kim, N. T. Gabriel, W.-B. Song, and J. J. Talghader, "Encapsulation of low-refractive-index SiO_2 nanorods by Al_2O_3 with atomic layer deposition," Opt. Express **15**, 16285 (2007).

103. M. Mireles, S. MacNally, C. Smith, and A. L. Rigatti, "Enhancing Stability of the Optical Properties of Nanostructured All-Silica Coatings," in Optica OIC — Optical Interference Coatings Conference 2025 Technical Digest Series, paper TD.4. (2025).
104. M. Mireles, S. MacNally, C. C. Smith, and A. L. Rigatti, "Defect passivation in nanostructured silica for stable birefringence in polarization optics," Appl. Opt. **65**, A99 (2026).
105. P. Ma, Y. Pu, W. Zhang, J. Die, M. Zhang, and H. Liu, "Protecting the EBE coatings from vacuum-air-shift by ion assistance or ALD capping layer," Ceramics International **48**, 2670–2676 (2022).
106. L. González-García, J. Parra-Barranco, J. R. Sánchez-Valencia, A. Barranco, A. Borrás, A. R. González-Elipe, M.-C. García-Gutiérrez, J. J. Hernández, D. R. Rueda, and T. A. Ezquerra, "Correlation lengths, porosity and water adsorption in TiO_2 thin films prepared by glancing angle deposition," Nanotechnology **23**, 205701 (2012).
107. A. Soutenain, M. Chorel, E. Lavastre, M. Guy, E. Laborde, J. Cornette, P. Carles, E. Yvernaud, Y. Launay, M. Colas, M. Mireles, A. Rigatti, C. Ducros, and C. Dublanche-Tixier, "Long-term aging of SiO_2/HfO_2 PIAD-deposited Laser Mégajoule polarizer coatings," Opt. Express **33**, 43116 (2025).
108. O. Stenzel, S. Wilbrandt, N. Kaiser, M. Vinnichenko, F. Munnik, A. Kolitsch, A. Chuvilin, U. Kaiser, J. Ebert, S. Jakobs, A. Kaless, S. Wüthrich, O. Treichel, B. Wunderlich, M. Bitzer, and M. Grössl, "The correlation between mechanical stress, thermal shift and refractive index in HfO_2, Nb_2O_5, Ta_2O_5 and SiO_2 layers and its relation to the layer porosity," Thin Solid Films **517**, 6058–6068 (2009).
109. K. Scherer, L. Nouvelot, P. Lacan, and R. Bosmans, "Optical and mechanical characterization of evaporated SiO_2 layers Long-term evolution," Appl. Opt. **35**, 5067 (1996).
110. J. A. Theil, D. V. Tsu, M. W. Watkins, S. S. Kim, and G. Lucovsky, "Local bonding environments of Si–OH groups in SiO_2 deposited by remote plasma-enhanced chemical vapor deposition and incorporated by postdeposition exposure to water vapor," Journal of Vacuum Science & Technology A: Vacuum, Surfaces, and Films **8**, 1374–1381 (1990).
111. A. Brunet-Bruneau, S. Fisson, G. Vuye, and J. Rivory, "Change of TO and LO mode frequency of evaporated SiO_2 films during aging in air," Journal of Applied Physics **87**, 7303–7309 (2000).
112. T. Zeng, M. Zhu, C. Yin, Y. Cui, J. Zhao, Y. Wang, G. Hu, Y. Chai, and J. Shao, "Strategy to improve the long-term stability of low-stress e-beam coatings," Opt. Mater. Express **10**, 2738 (2020).
113. A. C. van Popta, J. J. Steele, S. Tsoi, J. G. C. Veinot, M. J. Brett, and J. C. Sit, "Porous Nanostructured Optical Filters Rendered Insensitive to Humidity by Vapor-Phase Functionalization," Adv Funct Materials **16**, 1331–1336 (2006).

114. T. Zeng, M. Zhu, Y. Chai, C. Yin, N. Xu, K. Yi, Y. Wang, Y. Zhao, G. Hu, and J. Shao, "Effects of water adsorption on properties of electron-beam HfO_2/SiO_2 high-reflection coatings," Thin Solid Films **697**, 137826 (2020).
115. F. J. Ramos, T. Maindron, S. Béchu, A. Rebai, M. Frégnaux, M. Bouttemy, J. Rousset, P. Schulz, and N. Schneider, "Versatile perovskite solar cell encapsulation by low-temperature ALD-Al_2O_3 with long-term stability improvement," Sustainable Energy Fuels **2**, 2468–2479 (2018).
116. C.-Y. Chang, C.-T. Chou, Y.-J. Lee, M.-J. Chen, and F.-Y. Tsai, "Thin-film encapsulation of polymer-based bulk-heterojunction photovoltaic cells by atomic layer deposition," Organic Electronics **10**, 1300–1306 (2009).
117. G. Sharma, S. Khurana, S. Sapra, and P. K. Santra, "Vacancy Passivation and ALD Alumina Encapsulation Strategies for Stable Multilayered All-Inorganic Halide Perovskite Pc-WLEDs," Small e12820 (2026).
118. K. Pfeiffer, S. Shestaeva, A. Bingel, P. Munzert, L. Ghazaryan, C. Van Helvoirt, W. M. M. Kessels, U. T. Sanli, C. Grévent, G. Schütz, M. Putkonen, I. Buchanan, L. Jensen, D. Ristau, A. Tünnermann, and A. Szeghalmi, "Comparative study of ALD SiO_2 thin films for optical applications," Opt. Mater. Express **6**, 660 (2016).
119. T. Maindron, T. Jullien, and A. André, "Defect analysis in low temperature atomic layer deposited Al_2O_3 and physical vapor deposited SiO barrier films and combination of both to achieve high quality moisture barriers," Journal of Vacuum Science & Technology A: Vacuum, Surfaces, and Films **34**, 031513 (2016).
120. Y.-S. Lee, J.-H. Han, J.-S. Park, and J. Park, "Low temperature SiO_x thin film deposited by plasma enhanced atomic layer deposition for thin film encapsulation applications," Journal of Vacuum Science & Technology A: Vacuum, Surfaces, and Films **35**, 041508 (2017).
121. L. Grineviciute, H. Badorreck, L. Jensen, D. Ristau, M. Jupé, A. Selskis, and T. Tolenis, "Impact of deposition conditions on nanostructured anisotropic silica thin films in multilayer interference coatings," Applied Surface Science **562**, 150167 (2021).
122. X. Li, M. Gross, K. Green, B. Oreb, and J. Shen, "Ultraviolet laser-induced damage on fused silica substrate and its sol-gel coating," Opt. Lett. **37**, 2364 (2012).
123. E. Skliutas, D. Samsonas, A. Čiburys, L. Kontenis, D. Gailevičius, J. Berzinš, D. Narbutis, V. Jukna, M. Vengris, S. Juodkazis, and M. Malinauskas, "X-photon laser direct write 3D nanolithography," Virtual and Physical Prototyping **18**, e2228324 (2023).
124. J. W. Elam, M. D. Groner, and S. M. George, "Viscous flow reactor with quartz crystal microbalance for thin film growth by atomic layer deposition," Review of Scientific Instruments **73**, 2981–2987 (2002).

125. A. Rahtu, "Atomic Layer Deposition of High Permittivity Oxides: Film Growth and In Situ Studies," doctoral dissertation, University of Helsinki (2002).
126. U. Fantz, "Basics of plasma spectroscopy," Plasma Sources Sci. Technol. **15**, S137–S147 (2006).
127. S. Bublitz and C. Mühlig, "Absolute Absorption Measurements in Optical Coatings by Laser Induced Deflection," Coatings **9**, 473 (2019).
128. International Organization for Standardization, *ISO 21254-1:2011, Lasers and Laser-Related Equipment — Test Methods for Laser-Induced Damage Threshold — Part 1: Definitions and General Principles.* (2011).
129. G. C. A. M. Janssen, M. M. Abdalla, F. Van Keulen, B. R. Pujada, and B. Van Venrooy, "Celebrating the 100th anniversary of the Stoney equation for film stress: Developments from polycrystalline steel strips to single crystal silicon wafers," Thin Solid Films **517**, 1858–1867 (2009).
130. J. Canning, C. Clark, M. Dayao, D. De LaMela, M. Logozzo, and J. Zhao, "Anti-Reflection Coatings on 3D-Printed Components," Coatings **11**, 1519 (2021).
131. J. Moghal, S. Reid, L. Hagerty, M. Gardener, and G. Wakefield, "Development of single layer nanoparticle anti-reflection coating for polymer substrates," Thin Solid Films **534**, 541–545 (2013).
132. L. Grineviciute, S. Melnikas, J. Nikitina, M. Drazdys, A. Selskis, and D. Astrauskytė, "Optical Coating Deposition on Submicron-Patterned Surfaces," Coatings **15**, 372 (2025).
133. M. Dudziak, I. Topolniak, D. Silbernagl, K. Altmann, and H. Sturm, "Long-Time Behavior of Surface Properties of Microstructures Fabricated by Multiphoton Lithography," Nanomaterials **11**, 3285 (2021).
134. J. Bauer, A. G. Izard, Y. Zhang, T. Baldacchini, and L. Valdevit, "Thermal post-curing as an efficient strategy to eliminate process parameter sensitivity in the mechanical properties of two-photon polymerized materials," Opt. Express **28**, 20362 (2020).
135. S. Ratzsch, E.-B. Kley, A. Tünnermann, and A. Szeghalmi, "Influence of the oxygen plasma parameters on the atomic layer deposition of titanium dioxide," Nanotechnology **26**, 024003 (2015).
136. H. Wang, Z. Wang, X. Xu, Y. Liu, C. Chen, P. Chen, W. Hu, and Y. Duan, "Multiple short pulse process for low-temperature atomic layer deposition and its transient steric hindrance," Applied Physics Letters **114**, 201902 (2019).
137. C. A. Wilson, R. K. Grubbs, and S. M. George, "Nucleation and Growth during Al_2O_3 Atomic Layer Deposition on Polymers," Chem. Mater. **17**, 5625–5634 (2005).
138. J. C. Spagnola, B. Gong, S. A. Arvidson, J. S. Jur, S. A. Khan, and G. N. Parsons, "Surface and sub-surface reactions during low temperature aluminium oxide atomic layer deposition on fiber-forming polymers," J. Mater. Chem. **20**, 4213 (2010).

139. J. S. Jur, J. C. Spagnola, K. Lee, B. Gong, Q. Peng, and G. N. Parsons, "Temperature-Dependent Subsurface Growth during Atomic Layer Deposition on Polypropylene and Cellulose Fibers," Langmuir **26**, 8239–8244 (2010).
140. G. N. Parsons, S. E. Atanasov, E. C. Dandley, C. K. Devine, B. Gong, J. S. Jur, K. Lee, C. J. Oldham, Q. Peng, J. C. Spagnola, and P. S. Williams, "Mechanisms and reactions during atomic layer deposition on polymers," Coordination Chemistry Reviews **257**, 3323–3331 (2013).
141. R. L. Puurunen and W. Vandervorst, "Island growth as a growth mode in atomic layer deposition: A phenomenological model," Journal of Applied Physics **96**, 7686–7695 (2004).
142. P. Paul, V. Beladiya, D. Kästner, U. Schulz, M. Burkhardt, and A. V. Szeghalmi, "Conformal antireflection coating on polycarbonate domes," in *Advances in Optical Thin Films VII*, M. Lequime and D. Ristau, eds. (SPIE, 2021), p. 11.
143. A.-M. El-Sayed, M. B. Watkins, A. L. Shluger, and V. V. Afanas'ev, "Identification of intrinsic electron trapping sites in bulk amorphous silica from ab initio calculations," Microelectronic Engineering **109**, 68–71 (2013).
144. S. Bertet, "Study of GLAD coatings for the optical smoothing of high-power lasers,", doctoral dissertation, Sorbonne Université (2025).
145. W. Pong and C. S. Inouye, "Photoemission studies of LaF_3," J. Opt. Soc. Am. **68**, 521 (1978).
146. L. Skuja, H. Hosono, M. Hirano, and K. Kajihara, "Advances in silica-based glasses for UV and vacuum UV laser optics," in Proc. SPIE 5122, p. 1–14 (2003).
147. C. Li, X. Kang, D. Luan, Q. Zhu, and W. Zheng, "Laser-irradiation-driven formation of oxygen-related defects and performance degradation in fused silica with nanosecond pulsed laser at 355 nm," Optics & Laser Technology **111**, 727–733 (2019).
148. X. Gao, Q. Mu, and P. Zhou, "Propagation of point defects in SiO_2/Al_2O_3 anti-reflection coatings under multi-pulse laser irradiation," Applied Surface Science **695**, 162873 (2025).
149. D. Ristau, S. Günster, S. Bosch, A. Duparré, E. Masetti, J. Ferré-Borrull, G. Kiriakidis, F. Peiró, E. Quesnel, and A. Tikhonravov, "Ultraviolet optical and microstructural properties of MgF_2 and LaF_3 coatings deposited by ion-beam sputtering and boat and electron-beam evaporation," Appl. Opt. **41**, 3196 (2002).
150. C.-C. Lee, M.-C. Liu, M. Kaneko, K. Nakahira, and Y. Takano, "Influence of thermal annealing and ultraviolet light irradiation on LaF_3 thin films at 193 nm," Appl. Opt. **44**, 6921 (2005).
151. M.-C. Liu, C.-C. Lee, B.-H. Liao, M. Kaneko, K. Nakahira, and Y. Takano, "Fluoride antireflection coatings deposited at 193 nm," Appl. Opt. **47**, C214 (2008).

152. W. Lu, B. Pan, R. Miao, B. Yang, C. Yu, D. Zhang, D. Chen, L. Han, and Z. Wang, "Dependence of Structural and Optical Performance of Lanthanum Fluoride Antireflective Films on O Impurities," Coatings **12**, 1184 (2022).
153. L. V. Rodríguez-de Marcos, J. I. Larruquert, J. A. Méndez, and J. A. Aznárez, "Self-consistent optical constants of MgF_2, LaF_3, and CeF_3 films," Opt. Mater. Express **7**, 989 (2017).
154. Thorlabs, Inc., "Mounted Zero-Order Quarter-Wave Plates," product specifications. Available at: https://www.thorlabs.com/mounted-zero-order-half-wave-plates?tabName=Damage%20Thresholds (accessed 15 October 2026).
155. M. L. Hair, "Hydroxyl groups on silica surface," Journal of Non-Crystalline Solids **19**, 299–309 (1975).
156. J. Liu and H. Cao, "Sub-ambient water wettability of hydrophilic and hydrophobic SiO_2 surfaces," The Journal of Chemical Physics **161**, 184701 (2024).
157. G. Azimi, R. Dhiman, H.-M. Kwon, A. T. Paxson, and K. K. Varanasi, "Hydrophobicity of rare-earth oxide ceramics," Nature Mater **12**, 315–320 (2013).
158. I.-K. Oh, K. Kim, Z. Lee, K. Y. Ko, C.-W. Lee, S. J. Lee, J. M. Myung, C. Lansalot-Matras, W. Noh, C. Dussarrat, H. Kim, and H.-B.-R. Lee, "Hydrophobicity of Rare Earth Oxides Grown by Atomic Layer Deposition," Chem. Mater. **27**, 148–156 (2015).
159. S. Sankar, B. N. Nair, T. Suzuki, G. M. Anilkumar, M. Padmanabhan, U. N. S. Hareesh, and K. G. Warrier, "Hydrophobic and Metallophobic Surfaces: Highly Stable Non-wetting Inorganic Surfaces Based on Lanthanum Phosphate Nanorods," Sci Rep **6**, 22732 (2016).
160. W. Levason, F. M. Monzittu, and G. Reid, "Coordination chemistry and applications of medium/high oxidation state metal and non-metal fluoride and oxide-fluoride complexes with neutral donor ligands," Coordination Chemistry Reviews **391**, 90–130 (2019).
161. R. H. Hopkins, R. A. Hoffman, and W. E. Kramer, "Moisture resistant optical films: their production and characterization," Appl. Opt. **14**, 2631 (1975).
162. Z. Lin, C. Song, T. Liu, J. Shao, and M. Zhu, "Comparative Study of Plasma-Enhanced-Atomic-Layer-Deposited $Al_2O_3/HfO_2/SiO_2$ and $HfO_2/Al_2O_3/SiO_2$ Trilayers for Ultraviolet Laser Applications," ACS Appl. Mater. Interfaces **16**, 31756–31767 (2024).
163. Y. Chai, M. Zhu, K. Yi, W. Zhang, H. Wang, Z. Fang, Z. Bai, Y. Cui, and J. Shao, "Experimental demonstration of laser damage caused by interface coupling effects of substrate surface and coating layers," Opt. Lett. **40**, 3731 (2015).
164. W. Du, M. Zhu, J. Shi, T. Liu, J. Sun, K. Yi, and J. Shao, "Effect of subsurface impurity defects on laser damage resistance of beam splitter coatings," High Pow Laser Sci Eng **11**, e61 (2023).

165. S. Papernov and A. W. Schmid, "Laser-induced surface damage of optical materials: absorption sources, initiation, growth, and mitigation," in Laser-Induced Damage in Optical Materials: 2008, Proc. SPIE 7132, 71321J (2008).
166. D. C. Miller, R. R. Foster, S.-H. Jen, J. A. Bertrand, S. J. Cunningham, A. S. Morris, Y.-C. Lee, S. M. George, and M. L. Dunn, "Thermo-mechanical properties of alumina films created using the atomic layer deposition technique," Sensors and Actuators A: Physical **164**, 58–67 (2010).
167. C. A. Davis, "A simple model for the formation of compressive stress in thin films by ion bombardment," Thin Solid Films **226**, 30–34 (1993).
168. P. F. Carcia, R. S. McLean, and M. H. Reilly, "Permeation measurements and modeling of highly defective Al_2O_3 thin films grown by atomic layer deposition on polymers," Applied Physics Letters **97**, 221901 (2010).
169. J. A. Bertrand and S. M. George, "Evaluating Al_2O_3 gas diffusion barriers grown directly on Ca films using atomic layer deposition techniques," Journal of Vacuum Science & Technology A: Vacuum, Surfaces, and Films **31**, 01A122 (2013).
170. M. D. Groner, F. H. Fabreguette, J. W. Elam, and S. M. George, "Low-Temperature Al_2O_3 Atomic Layer Deposition," Chem. Mater. **16**, 639–645 (2004).
171. V. Verlaan, L. R. J. G. Van Den Elzen, G. Dingemans, M. C. M. Van De Sanden, and W. M. M. Kessels, "Composition and bonding structure of plasma-assisted ALD Al_2O_3 films," Phys. Status Solidi (c) **7**, 976–979 (2010).
172. M. Bischoff, T. Nowitzki, O. Voß, S. Wilbrandt, and O. Stenzel, "Postdeposition treatment of IBS coatings for UV applications with optimized thin-film stress properties," Appl. Opt. **53**, A212 (2014).
173. M. Falmbigl, K. Godin, J. George, C. Mühlig, and B. Rubin, "Effect of annealing on properties and performance of HfO_2/SiO_2 optical coatings for UV-applications," Opt. Express **30**, 12326 (2022).
174. B. Wang, H. Qi, H. Wang, Y. Cui, J. Zhao, J. Guo, Y. Cui, Y. Liu, K. Yi, and J. Shao, "Morphology, structure and optical properties in TiO_2 nanostructured films annealed at various temperatures," Opt. Mater. Express **5**, 1410 (2015).
175. B. Shougaijam, R. Swain, C. Ngangbam, and T. R. Lenka, "Analysis of morphological, structural and electrical properties of annealed TiO_2 nanowires deposited by GLAD technique," J. Semicond. **38**, 053001 (2017).
176. Z. Lin, M. Zhu, C. Song, T. Liu, C. Yin, T. Zeng, and J. Shao, "Effect of annealing on the properties of plasma-enhanced atomic layer deposition grown HfO_2 coatings for ultraviolet laser applications," Journal of Alloys and Compounds **946**, 169443 (2023).
177. A. Mahmood, N. Ahmed, Q. Raza, T. Muhammad Khan, M. Mehmood, M. M. Hassan, and N. Mahmood, "Effect of thermal annealing on the

structural and optical properties of ZnO thin films deposited by the reactive e-beam evaporation technique," Phys. Scr. **82**, 065801 (2010).
178. A. Lale, E. Scheid, F. Cristiano, L. Datas, B. Reig, J. Launay, and P. Temple-Boyer, "Study of aluminium oxide thin films deposited by plasma-enhanced atomic layer deposition from tri-methyl-aluminium and dioxygen precursors: Investigation of interfacial and structural properties," Thin Solid Films **666**, 20–27 (2018).
179. L. Ramalis, R. Buzelis, G. Dolmantaitė, and T. Tolenis, "Near fundamental nanosecond laser damage resistance of nanostructured all-silica mirrors at 355 nm by local laser irradiation," Results in Optics **14**, 100616 (2024).
180. L. Ramalis, "Formation of sculptured thin films on crystalline substrates and their investigation in laser systems," doctoral dissertation, Vilnius University (2025).

PADĖKA

Pirma, didžiausią padėką norėčiau išreikšti magistro ir doktorantūros studijų vadovei dr. Linai Grinevičiūtei, kurios paskatinta nusprendžiau tęsti pradėtus tyrimus ir studijuoti doktorantūrą bei pradėti naujas tyrimų kryptis. Ačiū už visapusišką pagalbą, patarimus, palaikymą ir įdomias diskusijas.

Esu ypatingai dėkinga dr. Ramučiui Drazdžiui už tai, jog bakalauro studijų metu priėmė mane į Optinių dangų laboratoriją, supažindino su optinių dangų sritimi ir atominių sluoksnių nusodinimo technologija.

Taip pat dėkoju prof. dr. Sauliaus Juodkazio tyrimų komandai iš Swinburne universiteto ir prof. dr. Mangirdo Malinausko grupei iš Vilniaus universiteto už bendradarbiavimą ir kartu atliktus tyrimus, kurie reikšmingai prisidėjo prie šio darbo.

Dėkoju visiems buvusiems ir esamiems kolegoms iš Optinių dangų laboratorijos, ypač dr. Mantui Drazdžiui, dr. Ryčiui Buzeliui, dr. Lukui Ramaliui, Mantui Slipkauskui ir Linai Volosevičienei, už pagalbą atliekant tyrimus, patarimus ir palaikančią aplinką.

Ačiū tėvams, artimiesiems ir draugams už nuolatinį palaikymą, paramą, supratingumą ir padrąsinimus siekti savo tikslų.

CURRICULUM VITAE

PERSONAL INFORMATION

Name, surname: Darija Astrauskytė
ORCID: https://orcid.org/0009-0004-4028-5263
Web of Science ResearcherID: NHP-9930-2025

EDUCATION

- 2022 – 2026 PhD studies in Materials Engineering, Center for Physical Sciences and Technology (FTMC), Theme: Formation of thin dielectric layers on structured elements using atomic layer deposition technology.
- 2020 – 2022 Master in Laser Technology, Vilnius University, Theme: The formation of optical coatings on structured elements using atomic layer deposition technology.
- 2016 – 2020 Bachelor in Applied Physics, Vilnius University, Theme: Investigation of the optical and physical properties of titanium oxide thin films synthesized by atomic layer deposition technology and application for the design of optical coatings.

WORK EXPERIENCE

- 2022 – present Junior researcher, Center for Physical Sciences and Technology (FTMC), Vilnius, Lithuania
- 2019 – 2022 Engineer, Center for Physical Sciences and Technology (FTMC), Vilnius, Lithuania

SCIENTIFIC AWARDS AND SCHOLARSHIPS

- Best student presentation in conference SPIE Optical Systems Design 2026 (2026 April 12–16, Strasbourg, France)
- Travel scholarship award from Research Council of Lithuania (LMTLT) for SPIE Optical Systems Design 2026 conference in Strasbourg, France, April 12–16
- Research Council of Lithuania (LMTLT) funding for study results (2025)
- Travel scholarship award from Research Council of Lithuania (LMTLT) for SPIE Optical Systems Design 2024 conference in Strasbourg, France, April 7–11
- Best poster presentation in conference Functional Inorganic Materials 2022 (2022 October 6–8, Vilnius, Lithuania)

Vilniaus universiteto leidykla
Saulėtekio al. 9, III rūmai, LT-10222 Vilnius
El. p. info@leidykla.vu.lt, www.leidykla.vu.lt
bookshop.vu.lt, journals.vu.lt
Tiražas 25 egz.